Homebuilt 4, 12 and 20 GHz Microwave Radiometers

by
Norman Grody (ngantique@hotmail.com)

4 GHz, 12 GHz and 20 GHz radiometers viewing rain through a glass patio door

Homebuilt 4, 12 and 20 GHz Microwave Radiometers

Norman C. Grody (ngantique@hotmail.com)

Preface

Beginning in the 1960's NASA solicited scientists and engineers to develop satellite infrared and microwave radiometers for observing and measuring the atmospheric and surface properties of our solar system. I began my government career working at NASA in 1971 at a time when the US first began carrying experimental microwave radiometers aboard satellites to view Earth from space. I then joined NOAA in 1972 working on more advanced radiometers by the Air Force, Navy, NASA and NOAA. Throughout the years, these instruments measured the extremely low level thermal radiation (~10^{-12} watts) emanating from the Earth's surface and atmosphere at frequencies between 6 and 183 GHz. At NOAA I was mainly involved in developing algorithms to derive surface and atmospheric parameters from the radiometric measurements. These parameters are used by various organizations to help forecast, analyze and monitor the weather and climate.

After retiring from NOAA in 2005 I considered building a microwave radiometer using components available through the Internet. My interest was spurred by a 2003 article I read from the internet (http://www.qsl.net/oh2aue/dicke) by Michael Fletcher who described a homebuilt 11 GHz Dicke radiometer and gave a number of references. One of the references, the Sept. 1978 article in Sky and Telescope (Vol. 56, No 3) by Swenson and Yang entitled "An Amateur Radio Telescope-V" was particularly helpful in that it gave detailed circuit diagrams. Another very good reference is the 162 page book entitled "Microwave Radiometer Systems: Design & Analysis" by Neils Skou. The book was published in 1989 by Artech House, Inc. and provides detailed construction and analysis of a 5, 17 and 34 GHz radiometer, each operating as a total power, Dicke and noise injection instrument. My project became a reality when I realized how cheap the components could be. In fact the most expensive part was the test equipment needed to measure the radiometer performance. Such test equipment included a Tektronix oscilloscope and a Hewlett Packard spectrum analyzer, sweep generator, power meter and a slotted line to measure the high emissivity calibration target. The test equipment was of high quality from the 1970's purchased from Ebay.

While some test equipment was relatively expensive (*i.e.*, 0.01 to 22 GHz spectrum analyzer cost $400), I was able to construct a 4, 12 and 20 GHz Dicke radiometer from parts costing less than $200 each. Most costly were the front end microwave components consisting of a waveguide to SMA (SubMiniature version-A) transition, followed by a Pin Diode Switch, an Isolator, and Low Noise Block converter (LNB), none of which I could construct. However, I was able to construct the lower frequency components that begins with a multiplexer and square law detector, followed by an AC amplifier, and ends with a synchronous demodulator. These were built using standard circuits containing operational amplifiers. I also constructed the antenna and radiometer cabinet using sheet metal.

Although all of the radiometers have similar design, the 4 GHz unit required a narrow band filter to suppress intermittent Radio Frequency Interference (*RFI*) from WiFi, radar

and aircraft altimeters as primary examples. In fact, the 4 GHz radiometer without the filter routinely detected approaching aircraft. Also, unlike the 4 GHz radiometer, the highest frequency 20 GHz radiometer occasionally detects interference in the form of DC offsets that could not be filtered out and appears to be due to satellite transmission. However, of greater importance is the fact that this radiometer has a peak response at 20.5 GHz which is near the 22.23 GHz water vapor line. As such, it has a higher sensitivity to water vapor as well as clouds and rain than the lower frequency radiometers. Therefore, calibration of this radiometer requires water vapor adjustments when using clear sky measurements. Such sky elevation scan measurements are considered to calibrate the radiometer and measure the atmospheric transmittance. This so called tipping curve procedure was developed by Dr. Robert Dicke and shown below being used by Dicke and his associates in 1946. Lastly, algorithms were developed based on simulations to derive water vapor and cloud liquid water from the combined 20 and 12 GHz radiometer measurements. These algorithms will be applied to the actual radiometer measurements in a later addition to evaluate their performance.

Historically, I began this project by first building a total power radiometer that only required an LNB, square law detector and DC amplifier. However, I found that very small gain changes in the LNB, detector and amplifier made it impractical to build a drift free total power radiometer without very frequent calibration. I therefore decided to forego the simpler total power radiometer in favor of the more stable Dicke radiometer which uses synchronous detection to reduce the effect of gain variations. In fact, because of this radiometer design, much of the concerns involving signal to noise ratio, stability of the system, sensitivity, etc., proved to be unfounded by the unattended long time performance of the instruments. Also, while the instrument portion of the document is complete there are still some additional measurements of the surface, atmosphere and calibration that will be expanded upon in future updates.

Tipping curve absorption measurements made in 1946 by Dr. Robert Dicke along with his associates. Starting on the Left is E. Beringer, R. Kyhl, A. Vane and R. Dicke. This picture is in the MIT Rad Lab Book “Five Years” (see pg. 113). It shows Dicke holding up an absorber in front of one of his radiometers while a chart recorder on the ground plots the measurements.

Contents

1. Introduction

This document summarizes my experience in constructing stable and reliable Dicke microwave radiometers at 4, 12 and 20 GHz. It is written for those with a background in microwave sensors and covers issues pertaining to the development and application of radiometers in remote sensing. Incidentally, while it's easy to find a complete Doppler radar module from the internet for under $10, this is not true of radiometers. In fact, it took me about 10 years of working on and off, until coming up with the final design described in Chapter 3. I'll now briefly mention a few of the issues I came across while working on this project.

The first issue involved the testing and evaluation of the radiometer performance. As described in Chapter 4, this ultimately required the construction of a high emissivity calibration target using high quality ferrite materials called Eccosorb manufactured by Emerson & Cuming. Calibration of the radiometer using the target revealed a number of issues. In particular, it became obvious that an isolator was needed to suppress the LNB local oscillator signal from being transmitted out and then reflected back into the radiometer due to a slight impedance mismatch of the target.

The second problem area had to do with the detector. As explained in Chapter 6, rather than purchase a square law detector, I constructed one using a Schottky diode. However, after considering different diodes and reviewing the literature, I realized the need to use a matched pair of diodes that is temperature compensated. Chapter 6 demonstrates the improvement in radiometer performance using such a temperature compensated detector.
.
The third problem had to do with the synchronous demodulator which was constructed from information acquired from the internet. As described in Appendix A4, this unit uses operational amplifiers configured as a difference amplifier, an integrator and a DC amplifier. Most important was the judicious choice of a J177 P-Channel MOSFET that is energized by a clock generator to switch the polarity of the difference amplifier output during half the clock cycle. This same clock also energizes a pin diode switch to switch the radiometer input from the antenna to a reference load. I tried different switching transistors until finally arriving at the J177, which could handle the large negative input signals when viewing space as well as the smaller positive signals when viewing earth.

The fourth issue pertains to *RFI* observed with the 4 GHz radiometer. Besides obvious sources (*e.g.*, aircraft altimeters, radar and WiFi), which I tracked down using my spectrum analyzer, there were many other frequencies that turned up intermittently. I tried using different filters placed after the LNB *IF* output to suppress the *RFI* until arriving at the final filter whose frequency response is shown in Appendix A7. However, as discussed in Chapter 8, *RFI* is not always narrow band and intermittent. This is shown for the 20 GHz radiometer whose interference could not be removed using filters.

The document concludes by showing measurements to demonstrate some radiometer applications in earth remote sensing. To make it interesting, the measurements were all done in my basement with the radiometer antennas viewing through my glass patio door. As such, the analysis of the measurements includes the transmission, reflection and absorption by the glass door. This added complexity does not detract from interesting findings of how the different frequencies respond to surface and atmospheric features.

2. Radiometers

To begin this discussion Figure 1 shows the 4 GHz radiometer where the right-most picture has the lid opened to show the labeled components. For a larger picture of the components see Figure 18. The bottom-right of Figure 1 shows the radiometer output connector (Rad Out) as well as other outputs used for diagnostics. Also shown is the 15 dB gain horn antenna in the front, which receives the microwave radiation. Design equations for the antenna are given in Appendix A1. The bottom-left of Figure 1 shows the power input connectors, the DC fine offset control and two additional diagnostic outputs. The digital voltmeter in the top-left picture is used to display the radiometer output and LNB temperature. A temperature regulated exhaust fan on the right side of the cabinet cools the LNB using the circuit in Appendix A2. For comparison, Figure 2 shows the 12 GHz radiometer. It has a 19 dB gain horn antenna and the same input and output connections as the 4 GHz radiometer. The bottom two figures show the lid opened to view the components. An enlarged picture of the 12 GHz components is shown in Appendix A3. As with the 4 GHz unit, the 12 GHz components are labeled so they can be compared with the block diagrams discussed in the next Chapter. As mentioned in the Title, this report also describes a 20 GHz radiometer that was constructed later after completing the lower frequency units. Its construction and measurements are described in a separate Chapter at the end of this document.

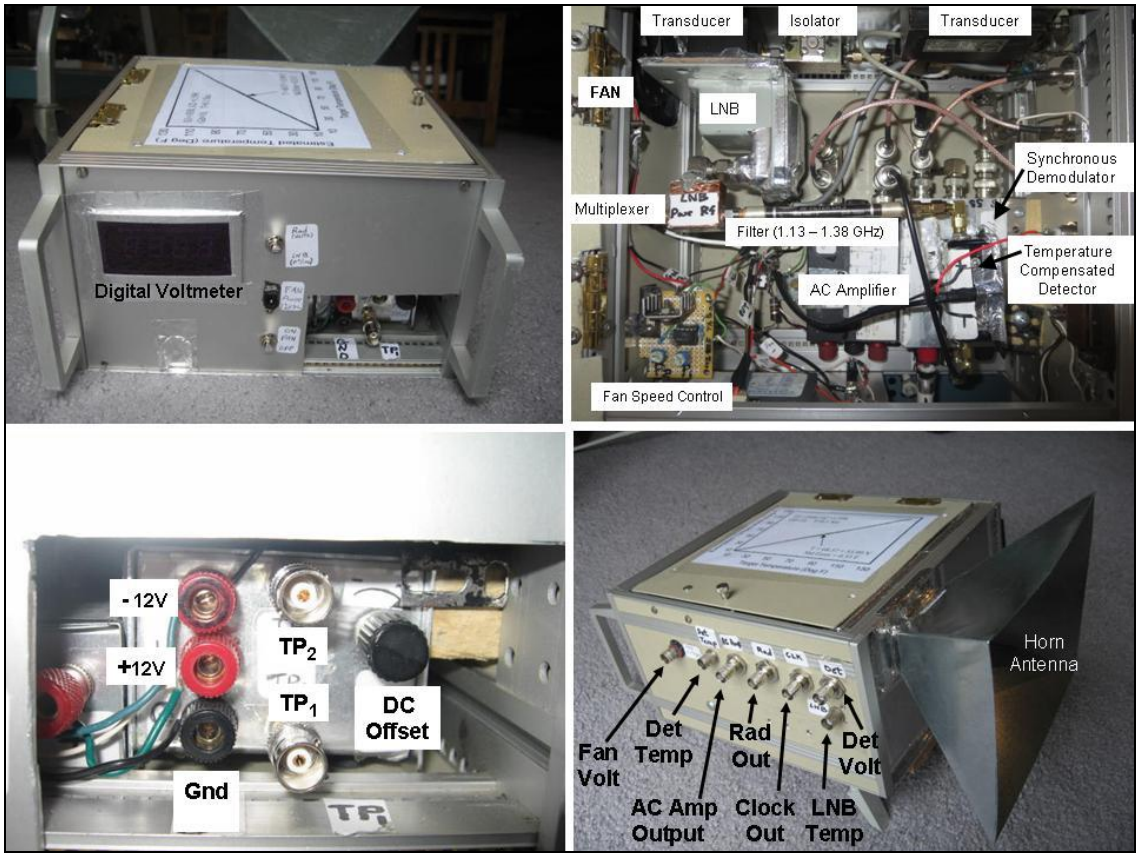

Figure 1- Different views of 4 GHz radiometer. The back view on top-left has a voltmeter to display the radiometer output. The open lid on top-right shows the components (see Figure 18 for a larger image). The bottom-left shows the power input, DC offset and two diagnostic outputs from the synchronous demodulator, TP_1, TP_2. The bottom-right shows the radiometer output (Rad Out) and other outputs. This view also shows the 15 dB gain pyramidal horn antenna.

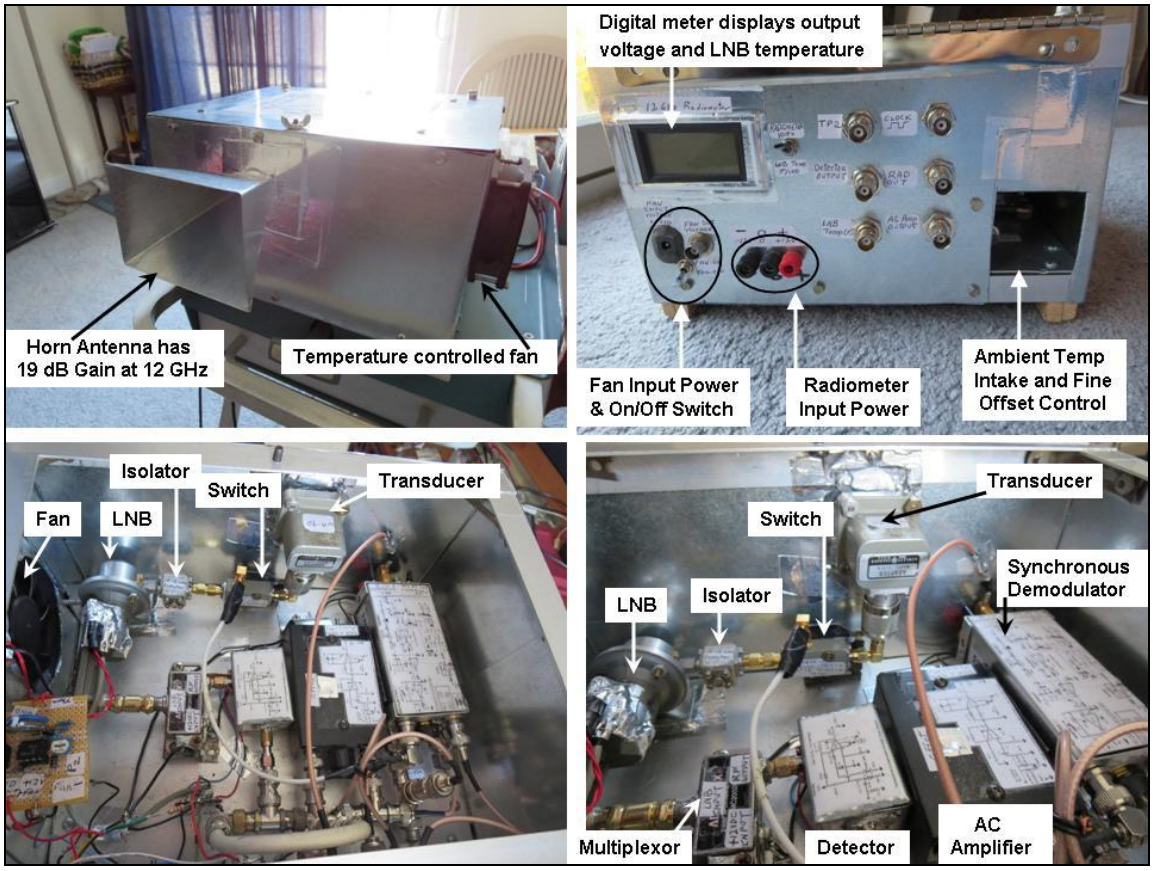

Figure 2 - Different views of the 12 GHz radiometer. The front view in top-left shows the 19 dB gain pyramidal horn antenna. The back view in top-right contains different outputs, including the power input and access to the fine offset control. The top lid is opened in the two bottom figures to show the various components (Figure A3 in the Appendix shows a larger picture).

3. Radiometer Block Diagrams

The radiometers are constructed using separate modules to facilitate the assembly and testing, as well as enhancing the isolation. Figures 1 and 2 show the placement of the different modules in the cabinets while Figures 3 and 4 show the block diagrams of the radiometers. The flow diagram for both radiometers begins on the left with the horn antenna. The antenna receives microwave thermal radiation and outputs it to a single pole single throw (SPST) pin diode switch that switches between the input noise temperature, T_A, and a resistive load inside the switch at temperature T_R. As such, the switched output is a modulated microwave signal whose envelope is a square wave with modulation amplitude T_R - T_A. The pin diode switch is driven by a square wave generator (clock) that also drives the last stage, synchronous demodulator, whose output is a DC level proportional to the difference between the two signals, *i.e.,* T_A - T_R. Although shown separately, the clock is part of the synchronous demodulator circuit which is briefly discussed next and more fully described in Appendix A4.

The block diagrams also illustrate the different waveforms at each output stage of the radiometer. Similarly, Figure 5 shows the measured waveforms seen after the detector

stage when the 4 GHz radiometer views space over a period of about two clock cycles or 10 milliseconds. The left-most Figure displays the modulated signals from the detector and AC amplifier output while the right-most Figure shows the synchronous demodulator output, TP_2, prior to its integrator and amplifier stage The synchronous demodulator uses a difference amplifier to switch the polarity of the modulated signal during half the clock cycle. As discussed in Appendix A4, this demodulated waveform shown in the Figure is then passed through an integrator to smooth the signal. The next stages in the synchronous demodulator are then used to provide low level amplification and set the DC offset. As a result of these operations the output from the synchronous demodulator, shown in the block diagrams, reduces short time drift, T_{Drift}, and the effect of gain fluctuations by the preceding radiometer amplifiers. On the other hand, instrumental noise, T_N, is uncorrelated so taking the difference in the demodulator does not cancel this noise. However, as shown by equations (7a, b) in Chapter 5, temporal averaging by the integrator stage of the synchronous demodulator significantly reduces this noise.

Before reaching the synchronous demodulator, the modulated (*i.e.*, switched) microwave signal shown in the block diagrams is first amplified by the LNB which has high gain (60 dB) with a very low noise figure of 0.2 dB or 14 *K* noise temperature for the C and Ku bands. These microwave amplifiers were developed commercially beginning in the 1970's for direct broadcast satellite TV reception, and is the key radiometer component used here. Unlike more recent direct detect amplifiers using Monolithic Microwave Integrated Circuit (MMIC) technology, LNB's use the more traditional heterodyne principle to down convert the input signal to a lower intermediate frequency (*IF*) between 1 and 2 GHz. These operations are shown in the block diagram of a generic LNB in Figure 6. To obtain the very low noise figure, the LNB uses very low noise Field Effect Transistors (FET's) configured as amplifiers, a local oscillator (*LO*) and mixer. The stable *LO* frequency is generated using a crystal Dielectric Resonator Oscillator (DRO) driven by an FET. As such, LNB's greatly simplify the radiometer construction by combining the amplifiers, *LO* and mixer into a single unit. Unfortunately, however, LNB's are only available at specific frequencies in C-Band, Ku-Band and Ka Band.

For reference, the bottom of Figure 6 shows the LNB's used in my 4 and 12 GHz radiometers, which have waveguide input and coax output for the *IF* signal. As discussed in Chapter 4, these radiometers result in a noise equivalent temperature (NEΔT) of about 0.3 *K* for a 0.1 second integration time. The Figure also indicates the availability of Ka band LNB's that generally cover the 18.3 to 20.2 GHz region while some go slightly beyond this frequency range. While I began this project by developing a 4 and 12 GHz radiometer, I more recently constructed a Dicke radiometer using the Norsat 9000C Ka band LNB shown in Figure 6 which is measured in Chapter 8 to have a peak response at 20.5 GHz. As such, while the report was originally written to discuss the 4 and 12 GHz radiometers, I have now extended it to describe this latest radiometer, whose frequency is near the 22.23 GHz water vapor absorption line. This LNB has an *LO* at 19.25 GHz with a 1.3 dB noise figure or a noise temperatures of 100 *K*. As such the radiometer requires an integration time larger than 0.1 seconds to obtain the same 0.3 *K* NEΔT of the lower frequency radiometers. A description of the 20 GHz radiometer, its calibration and measurements is given in Chapter 8, along with its application to measure water vapor and cloud liquid water.

Referring back to the radiometer block diagrams, the square wave envelope of the *IF* signal is detected using matched pair Schottky diodes that are temperature compensated

using the difference amplifier circuit described in Appendix A5. This very small envelope is then amplified using an AC amplifier that also removes the detectors 10 mv DC level shown in Figure 5. The AC amplifier circuit is described in Appendix A6. In addition to these components the radiometers use a wide band isolator between the switch output and LNB input. The 4 GHz isolator frequency response is shown in Appendix A7. Note that it blocks reflections due to an impedance mismatch between the switch and LNB at the input frequencies of 3.76 to 4.01 GHz. More importantly, the isolator also blocks the 5.15 GHz *L0* radiation generated within the C-Band LNB from being leaked out through the antenna. The Ku Band LNB has its *L0* at 10.75 GHz and therefore requires a different isolator. Without the isolator, this radiation leakage from the *L0* produces calibration errors when it is reflected back into the radiometer due to an impedance mismatch between the antenna and calibration target. Similarly, the isolator also prevents the *L0* from being reflected back into the radiometer by an impedance mismatch between the switch and LNB which would produce an additional error.

While radio frequency interference is no problem at Ku-Band, there are many sources at C-Band (*e.g.*, WiFi, radar, aircraft altimeters). As such the 4 GHz block diagram contains an optimally chosen narrow band coaxial bandpass filter at the LNB output to suppress most radio frequency interference (*RFI*). Figure A8 of the Appendix shows the filter response to be centered at 1.26 GHz with a 250 MHz bandwidth and very high out of band rejection. As a result of the filter, the equivalent input frequency amplified by the LNB is reduced from 3.30 - 4.30 GHz to 3.76 - 4.05 GHz. Since the input power to the antenna is given by the Nyquist equation $4kTB$, the four times reduction in bandwidth, B, requires a four times increase in gain. The 12 GHz radiometer does not require such a filter so that it can use its full LNB bandwidth of 500 MHz. As such, the 4 GHz radiometer requires double the gain of a comparable 12 GHz radiometer. Not resolved at this time is the interference seen for the 20 GHz radiometer as discussed in Chapter 8.

As noted in the block diagrams and described in Appendix A4, the synchronous demodulator contains an integrator with adjustable time constants to reduce short time instrumental noise, T_N, from the LNB as well the other components. The demodulator also contains a low gain DC amplifier and a DC offset control that is set during calibration. Schematics of the synchronous demodulator, temperature compensated detector and AC amplifier are given in the Appendices. Not shown in the block diagram is the Transition whose waveguide input connects to the antenna while its SMA output connects to the pin diode switch. A second Transition is placed between the LNB waveguide input and SMA isolator output. These components are shown in Figures 1 and 2 along with a multiplexer that is connected to the LNB *IF* output. The multiplexer or bias tee is shown in Figure 7 for the 4 GHz radiometer. It uses filters to pass DC power to the LNB while extracting its *IF* signal. To improve the insertion loss and bandpass, commercially built multiplexers use Surface Mount Technology (SMT) components placed on a printed circuit board (PCB).

The block diagrams also show that the LNB uses a 12 volt regulated power source while the AC amplifier, temperature compensated detector and synchronous demodulator require +/-12 volts. All voltages are obtained from a single regulated power supply which provides about 200 milliwatts to power each radiometer, with most of the power used by the LNB. While I found that temperature regulation was not a serious problem, a small 12 volt exhaust fan shown in Figure 2 is attached to the cabinet to cool down the LNB and other components, where the fan speed is varied depending on the LNB temperature. A

simple fan speed control circuit that uses ambient temperature for cooling is shown in Appendix A2.

Many of the components have adjustable parameters although they are fixed after calibration. These parameters include the gain of the AC amplifier, G_1, detector, G_d, and DC amplifier, G_2. As shown in the block diagrams Dicke radiometers measure the difference between the input radiation and the warm reference temperature. As such, the smallest signal occurs when viewing earth while the largest signal, which is negative, occurs when viewing cold space as was shown in Figure 5. Therefore, to prevent saturation of the AC amplifier output, its gain must be set so that the radiometer output is less than about -10 volts when viewing space. Also, as discussed in Section 6.1, the detector bias and input signal level must be such that the detector output voltage varies linearly with input power for both small and large input signals. Finally, for convenience, the DC offset provided by the synchronous demodulator is set so that the radiometer output is near zero when viewing a high emissivity target at ambient temperature.

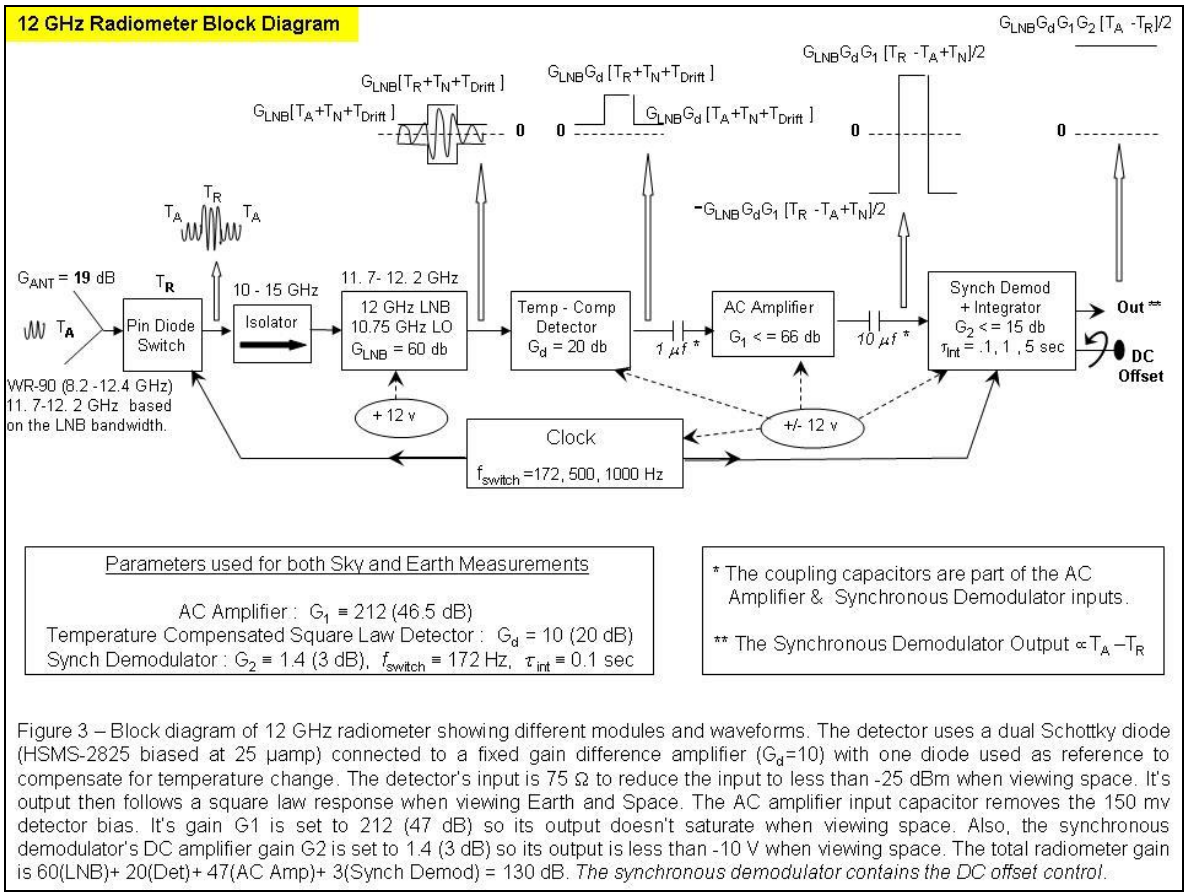

Figure 3 – Block diagram of 12 GHz radiometer showing different modules and waveforms. The detector uses a dual Schottky diode (HSMS-2825 biased at 25 μamp) connected to a fixed gain difference amplifier (G_d=10) with one diode used as reference to compensate for temperature change. The detector's input is 75 Ω to reduce the input to less than -25 dBm when viewing space. It's output then follows a square law response when viewing Earth and Space. The AC amplifier input capacitor removes the 150 mv detector bias. It's gain G1 is set to 212 (47 dB) so its output doesn't saturate when viewing space. Also, the synchronous demodulator's DC amplifier gain G2 is set to 1.4 (3 dB) so its output is less than -10 V when viewing space. The total radiometer gain is 60(LNB)+ 20(Det)+ 47(AC Amp)+ 3(Synch Demod) = 130 dB. *The synchronous demodulator contains the DC offset control.*

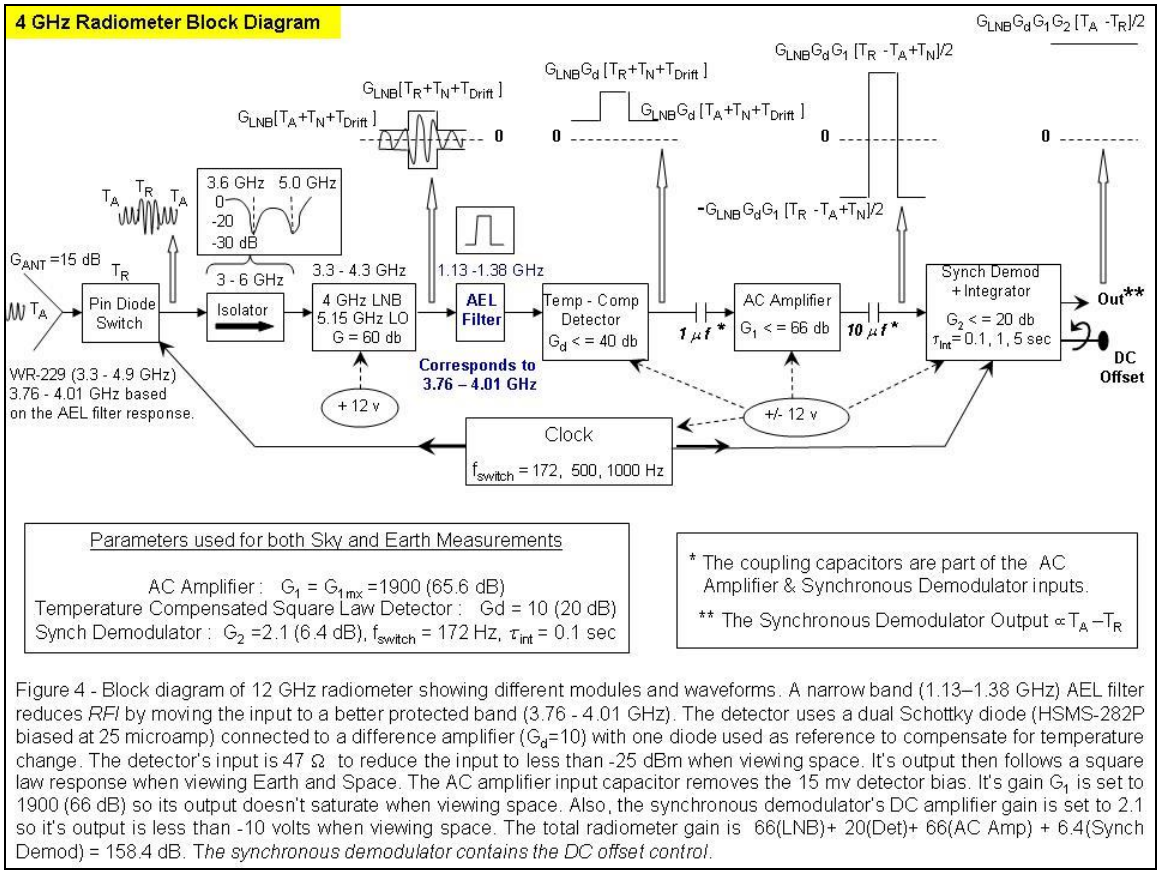

Figure 4 - Block diagram of 12 GHz radiometer showing different modules and waveforms. A narrow band (1.13–1.38 GHz) AEL filter reduces *RFI* by moving the input to a better protected band (3.76 - 4.01 GHz). The detector uses a dual Schottky diode (HSMS-282P biased at 25 microamp) connected to a difference amplifier (G_d=10) with one diode used as reference to compensate for temperature change. The detector's input is 47 Ω to reduce the input to less than -25 dBm when viewing space. It's output then follows a square law response when viewing Earth and Space. The AC amplifier input capacitor removes the 15 mv detector bias. It's gain G_1 is set to 1900 (66 dB) so its output doesn't saturate when viewing space. Also, the synchronous demodulator's DC amplifier gain is set to 2.1 so it's output is less than -10 volts when viewing space. The total radiometer gain is 66(LNB)+ 20(Det)+ 66(AC Amp) + 6.4(Synch Demod) = 158.4 dB. *The synchronous demodulator contains the DC offset control.*

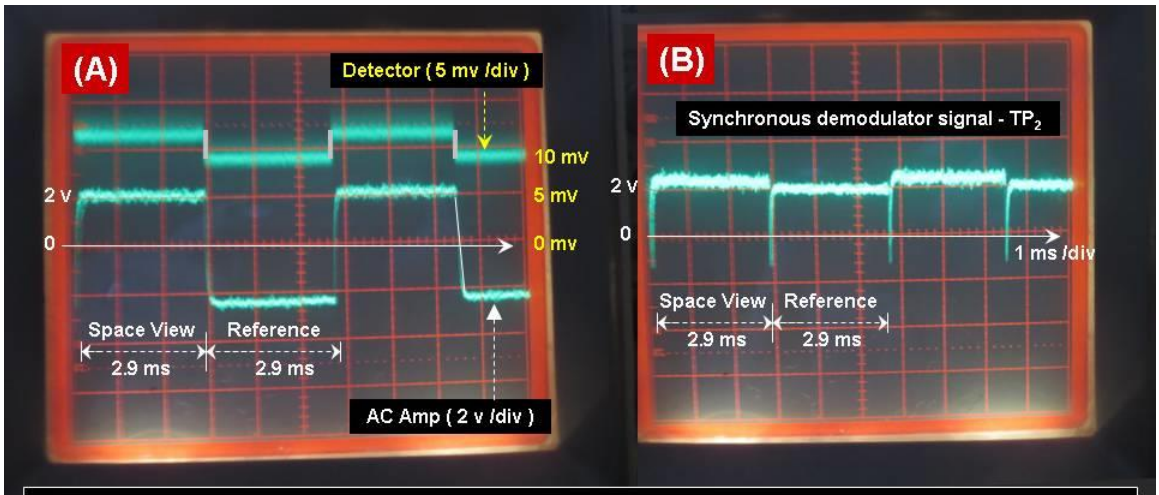

FIGURE 5 - 4 GHz radiometer viewing space through glass door shown in cover picture. Radiometer parameters are G_1 =1900, G_2 =2.1, G_d =10. Shown is the output voltage from

(A) Detector and AC Amplifier (note the different vertical scales).
(B) Synchronous Demodulator before its integrator and DC amplifier stage.

Radiometer Output

The integrator and amplifier stages of the synchronous demodulator smoothes, amplifies and inverts the signal TP_2 so the radiometer output becomes – 4.9 volts.

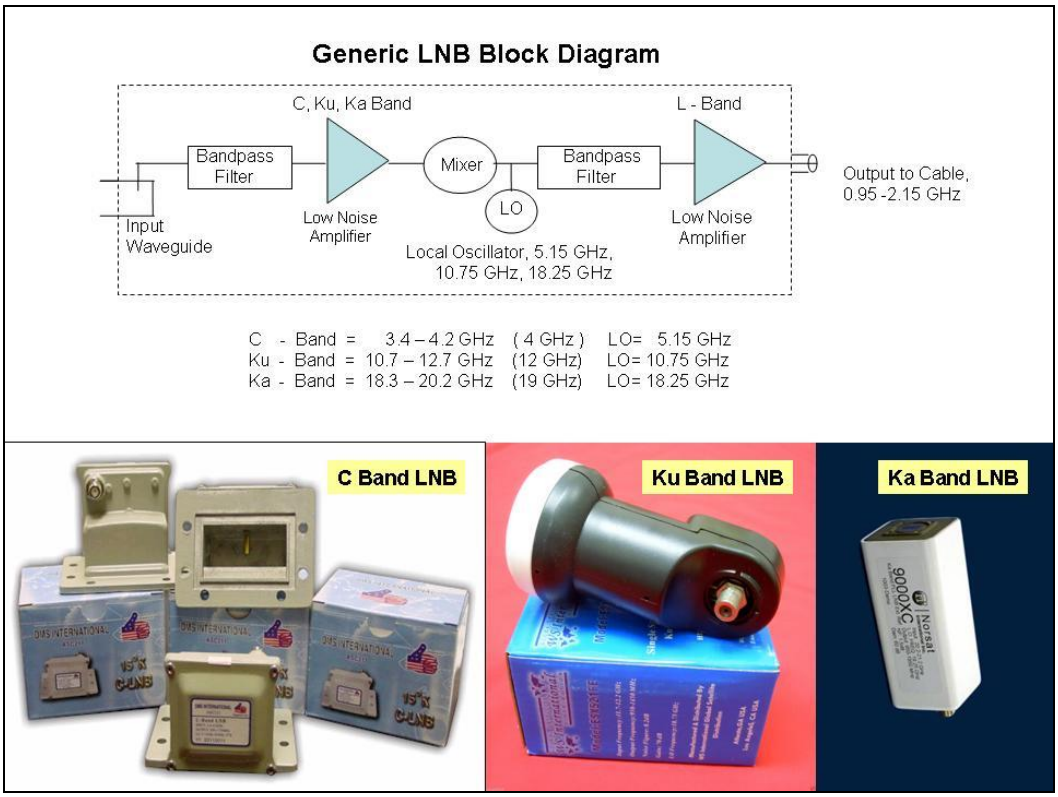

Figure 6 – The key radiometer component is the Low Noise Block down converter (LNB) whose generic block diagram is shown in the top figure. It uses the heterodyne principle to receive high frequency microwave radiation and down convert it to a lower Intermediate Frequency (*IF*) between 1 and 2 GHz using a Local Oscillator (*LO*) and mixer. It has high gain (>60 dB) with a very low noise figure and was originally used at the feed point of satellite TV dish antennas. The bottom figures show the LNB's used in my 4 GHz (C-Band), 12 GHz (Ku-Band) and 20 GHz (Ka-Band) radiometers and have waveguide input and coax output.

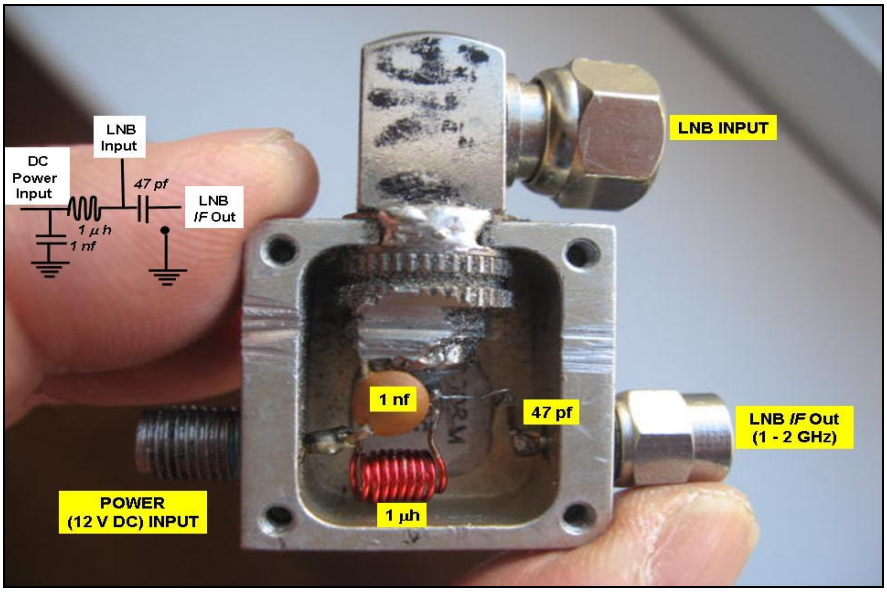

Figure 7 – Multiplexer used in 4 GHz radiometer (see Fig. 1 Top-Right). Insert on the left shows the circuit, while the cover is removed to show the components. The unit is connected to the LNB (Top) to provide a DC power path while also providing a path to access the down converted *IF* signal between 1 and 2 GHz (Bot-Right). The inductor and 1 nf capacitor block the *IF* signal from leaking to the power supply while the 47 pf capacitor blocks the DC power from exiting the LNB.

4. Radiometer Calibration

I initially spent much time testing different radiometer configurations as well as different components before coming up with the final design shown in Figures 3 and 4. To check the linearity and calibrate the radiometers, a high emissivity target is needed so that the radiometer voltage depends only on the targets physical temperature. A high emissivity, low reflectivity target also prevents microwave and thermal radiation generated by the instrument from being reflected back by the target into the radiometer. The coherent microwave radiation was mentioned previously, and consists of the *LO* leakage signal generated within the LNB that is blocked by the 30 dB isolator placed in front of the LNB (see Figures 3 and 4). Note that the 4 GHz radiometer isolator is wideband in order to suppress the 5.15 GHz local oscillator signal in addition to providing an impedance match at the input LNB frequencies between 3.76 and 4.01 GHz (see Figure A7). The thermal radiation referred to is the heat produced by the LNB that gets conducted out through the antenna and reflected back by the target.

After considering different materials I found that the best target is constructed using three sheets of ferrite material, called Eccosorb MCS by Emerson and Cuming, which are glued together and backed by an aluminum plate. According to the manufacturer this particular absorbing material works between 1 and 18 GHz. Figure 8 shows the target in the upper right picture. The upper left picture shows the layout used to measure the voltage standing wave ratio (VSWR) of the target over the 4 GHz radiometer frequency band. The setup consists of a coaxial slotted line terminated on one side by a coax to waveguide transition that the target rests on. The other side of the slotted line goes to an isolator, which is connected to a signal generator. Also shown is the VSWR meter connected to a crystal detector, which slides along the slotted line to measure the ratio of maximum to minimum voltage. A plot of the measured VSWR as a function of frequency is shown in the bottom left image. The reflectivity, Γ, and target emissivity, ε_S, are determined from VSWR measurements using the equations

$$|\Gamma| = \frac{VSWR - 1}{VSWR + 1} \quad where \quad \varepsilon_S = 1 - |\Gamma|^2 \cdot \qquad (1)$$

Figure 8 shows the VSWR measurements for frequencies corresponding to the 4 GHz radiometer. As indicated in Figure 3, the 4 GHz radiometer has a 250 MHz bandwidth between 3.76 to 4.01 GHz due to its bandpass filter. Within these frequencies the VSWR varies between 1.10 and 1.05 so that the calculated emissivity is better than 0.99. The emissivity for the 12 GHz radiometer is found to be slightly lower due to its higher frequency and wider 500 MHz bandwidth, which is between 11.7 and 12.2 GHz due to the LNB (see Figure 4). The VSWR measurements within these frequencies are found to vary between 1.8 and 1.2 so that the emissivity is between 0.92 and 0.99, respectively. Finally, as shown in Figures 8 and 9, the target contains an LM34 thermocouple temperature sensor attached through the aluminum plate to the Eccosorb. This sensor measures the target temperature during the calibration procedure.

As part of the calibration procedure, the target was initially cooled to 10 ^{0}F by placing it in a freezer. The target is then placed over the antenna as shown in Figure 9, and the radiometer output voltage and target temperature are recorded as the target slowly warms for more than an hour to reach room temperature. For data storage and analysis, the radiometer output as well as three other signals is connected to a 12 bit analog to digital converter (DI-158) by DATAQ Instruments, whose output is connected to a laptop computer through its USB port. Software supplied by the manufacturer enables one to monitor the time variation of up to four signals at once.

As an example, Figure 10 shows the calibration measurements for the 12 GHz radiometer. The temperature and voltage changes quickly initially and then more slowly as the target approaches room temperature (see top Figures). To accurately measure these changes, the integration time of the radiometer is set to its minimum of 0.1 seconds. Although not necessary, the plotted measurements are sampled averaged using the DATAQ software to reduce the noise by a factor of three. The left-most plot shows the radiometer output voltage increasing over 1.5 hours as the target warms from 10 ^{0}F to the 68 ^{0}F room temperature. Variation of target temperature with time is plotted in the right-most figure.

Regression analysis of these data is used to obtain an equation between voltage and target temperature, as well as the inverse equation, along with their standard errors (SE). The equations and SE are listed in the figures along with the yellow curves, which is the voltage and temperature estimates based on the equations. The bottom Figure shows the estimated target temperature using the regression equation plotted against the actual target temperature. This expression,

$$\text{Target } (^0\text{F}) = 68.1 + 58.9\ \text{V} \qquad (2a)$$

is called the calibration equation and converts the radiometer measured voltage to temperature, which is generally referred to as brightness temperature, T_b. Also, the calibration constant in the equation is called the offset while the voltage proportionality constant is called the radiometric gain. The bottom figure also shows a one to one line in yellow and, as with the other figures, lists the amplifier gains associated with the radiometer under test. Incidentally, while temperature is given in degrees Fahrenheit, it is custom to express it in degrees Kelvin so that the brightness temperature becomes

$$T_b(K) = 293.2 + 32.7\ \text{V}. \qquad (2b)$$

A very similar calibration equation is obtained for the 4 GHz radiometer by appropriately setting its amplifier gain. In this way the 4 and 12 GHz radiometer measurements can be compared directly with one another without having to account for different calibration parameters (*i.e.*, offset and radiometric gain). Alternatively, once the final radiometer design is arrived at and it is fully calibrated, one can use the calibrated brightness temperatures instead of voltages when comparing the two radiometer measurements. However, since the radiometer gain parameters G_1, G_2 and G_d have been changed slightly during the course of this investigation, I have chosen to reference the voltage measurements together with the calibration equations.

Equation (2b) has a SE or noise equivalent temperature (NEΔT) of only 0.09 *K* (0.17 ^{0}F) for the 0.1 second integration time. This low radiometer noise is attributed to the

excellent linearity over the 32 *K* (58 ^{0}F) temperature range in addition to the low noise figure (0.2 dB) of the LNB. As mentioned above the NEΔT is reduced by a factor of three by sample averaging the measurements. While the 32 *K* temperature range may be adequate when viewing earth, colder temperatures are preferred to calibrate the radiometer for sky viewing measurements where T_b can approach the 2.7 *K* cosmic background. Alternatively, assuming the radiometer operates linearly, one could use equation (2b) to extrapolate measurements to colder or warmer temperatures. For example, according to equation (2b) the voltage increases from -8.9 volts to 0 volts as T_b increases from 2.7 *K* to 293 *K*. Although these voltages are within the +/-10 volt saturation limit, calibration using colder temperatures is preferred to assure linearity for the large dynamic range observed when viewing both earth and space. One method of obtaining this is the cold sky calibration procedure described next.

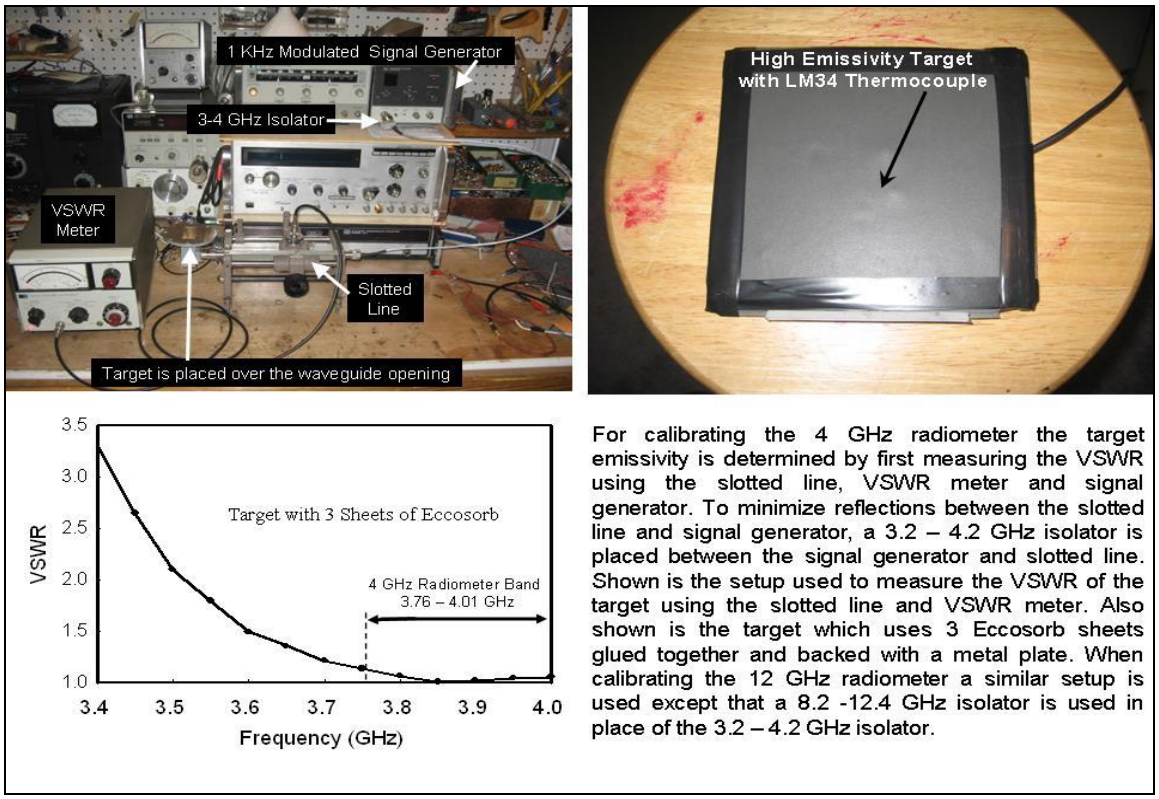

Figure 8 - The target shown in the top-right image is contains three Eccosorb sheets backed by an aluminum plate. Its temperature is measured using the LM34 thermocouple imbedded in the Eccosorb. The targets VSWR is measured using the slotted line setup shown in the upper left picture. The bottom-left graph shows the measured VSWR plotted as a function of frequency.

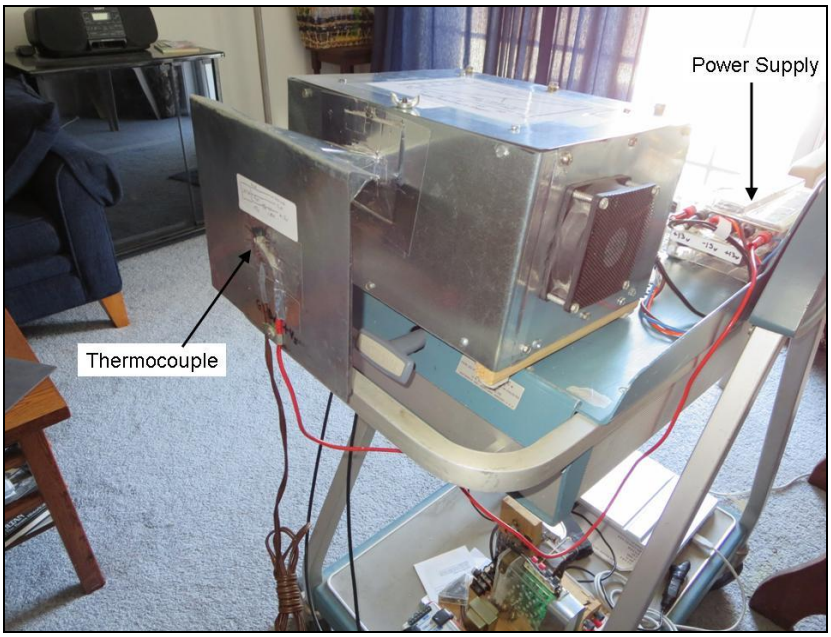

Figure 9 -Calibration of 12 GHz radiometer by placing a high emissivity target over the antenna. The target temperature is monitored using the attached thermocouple.

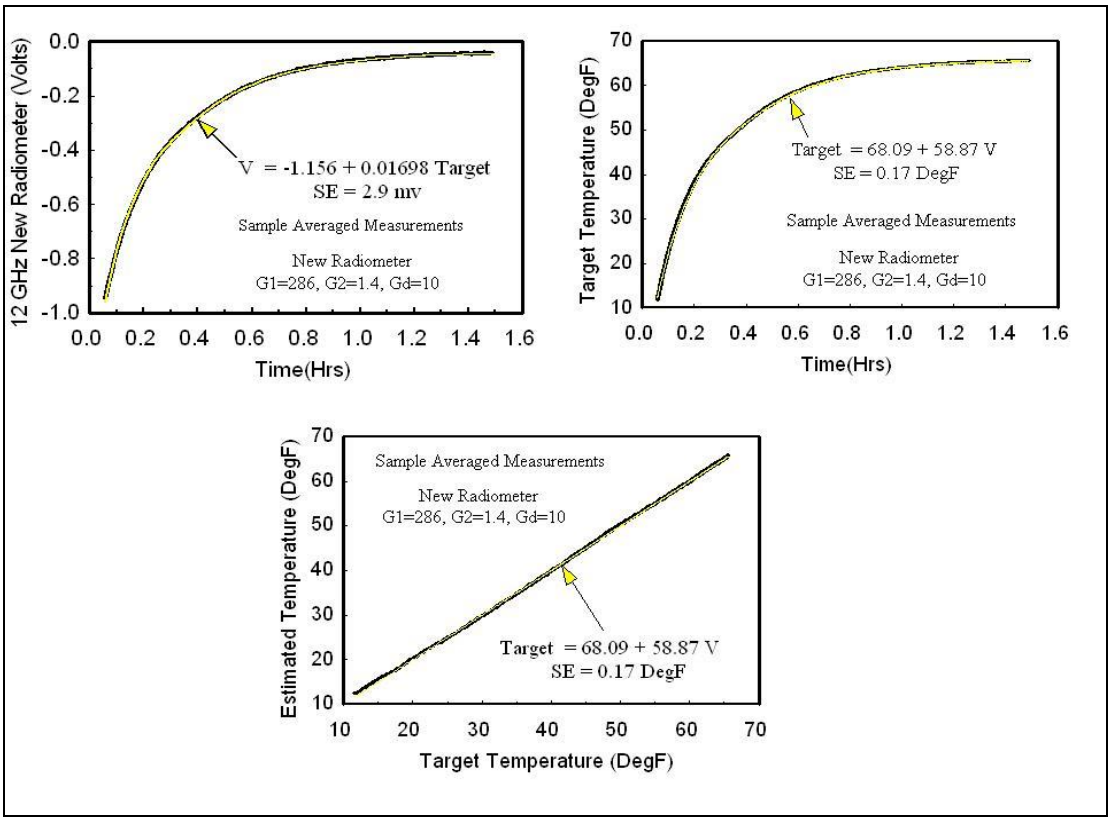

Figure 10 - Calibration of 12 GHz radiometer using a high emissivity target. The left figure shows the radiometer voltage as the target warms from 10 ^{0}F to room temperature at 68 ^{0}F, while the right figure shows the target temperature as a function time. The left figure also shows the best fit equation of voltage as a function of temperature in yellow, while the right figure shows the temperature as a function of voltage in yellow. The bottom figure shows the target temperature using the best fit equation plotted against actual temperature, with a one to one line in yellow.

4.1 Sky Brightness Temperature

As indicated by equation (2b), the linear brightness temperature equation has the form

$$T_b = \mathrm{I} + \mathrm{S}\,\mathrm{V}, \qquad (3)$$

where I is the intercept or offset, S is the slope or radiometric gain and V is the radiometer output voltage.

In the previous Section a high emissivity target having variable temperature was used to measure the calibration parameters and check the linearity over a small temperature range. However, in general, the radiometric offset and gain in (3) is determined using a two point calibration procedure whereby the radiometer views a high emissivity target having warm and very cold temperatures, T_W and Tc. As such, the calibration parameters become

$$S = \frac{T_W - T_C}{\mathrm{V}_W - \mathrm{V}_C}, \quad \text{and} \quad \mathrm{I} = \frac{T_C \mathrm{V}_W - T_W\ \mathrm{V}_C}{\mathrm{V}_W - \mathrm{V}_C} \qquad (4)$$

where V_W and V_C are the radiometer voltages measured when viewing the warm and cold targets. To obtain the largest dynamic range, the warm target is usually around ambient temperature, while the cold target temperature is obtained using liquid nitrogen whose boiling point temperature is 77 *K*.

As a second calibration approach, the more traditional cold sky method is used where the warm target measurement defines the high voltage calibration point while cloud free sky measurements, $T_C = T_{SKY}$, are used to obtain the lowest voltage, $V_C = V_{SKY}$, calibration point. For these measurements the radiometers were placed on my upper patio deck with the antenna viewing the sky as shown in Figure 11 for the 4 GHz radiometer. At such low frequencies or at very high altitudes atmospheric absorption is small so that T_{SKY} approximates the cosmic background radiation, T_{CB}, of 2.7 *K*. However, as discussed below, in general $T_{SKY} > T_{CB}$ so that one must accurately determine T_{SKY} from measurements or model calculations.

Figure 12 shows the different parameters affecting the sky brightness temperature based on radiation transfer. The sky brightness temperature, T_{SKY}, seen by an upward viewing radiometer is given by a radiation transfer equation which contains two terms, the attenuated cosmic radiation $\tau^{\mathrm{Sec}\theta}\, T_{\mathrm{CB}}$ and the downwelling atmospheric emission $[1-\tau^{\mathrm{Sec}\theta}]\, T_{\mathrm{M}}$,

$$\boxed{T_{\mathrm{SKY}}(\theta) = \tau^{\mathrm{Sec}\theta}\, T_{\mathrm{CB}} + [1-\tau^{\mathrm{Sec}\theta}]\, T_{\mathrm{M}} \quad .} \qquad (5)$$

Both terms in (5) contain the transmittance, τ, which is the fraction of radiant power transmitted vertically through the atmosphere to the receiving antenna. The $Sec\theta$ exponent of τ is a result of the increased path length when viewing at off zenith angles, θ, through a vertically stratified atmosphere. Equation (5) also contains the cosmic background radiation temperature T_{CB} of 2.7 *K*, and mean atmospheric temperature T_M.

The mean atmospheric temperature in (5) can be written as

$$T_{\mathrm{M}} = \frac{\int_0^{\infty} T(\mathrm{z}) \dfrac{\mathrm{d}\tau(\mathrm{z})^{\mathrm{Sec}\theta}}{\mathrm{dz}}\,\mathrm{dz}}{\int_0^{\infty} \dfrac{\mathrm{d}\tau(\mathrm{z})^{\mathrm{Sec}\theta}}{\mathrm{dz}}\,\mathrm{dz}} \qquad (6a)$$

with $$\tau(\mathrm{z}) = e^{-\alpha(\mathrm{z})} = e^{-\int_{\mathrm{z}}^{\infty}\gamma(z')dz'} \quad . \qquad (6b)$$

Physically, T_M is the temperature $T(z)$ vertically averaged over the weighting function, $d\tau(z)^{\mathrm{Sec}\theta}/dz$, where $\tau(z)$ is the transmittance function at height z above the ground. As mentioned above, the transmittance τ in (5) is the transmittance function from the ground to the top of the atmosphere, *i.e.*, $\tau(\mathrm{z} = 0)$. The transmittance function in turn depends on the absorption coefficient per unit length, $\gamma(\mathrm{z})$, or opacity function $\alpha(\mathrm{z})$ in (6b) where $\alpha(\mathrm{z} = 0) = \alpha$ is the opacity. Furthermore, the weighting function can be shown to decrease exponentially with height, z, peaking at the surface where z = 0. As such, the mean temperature for the 4, 12 and 20 GHz radiometers can be approximated as $T_M \approx \Gamma\ T_S$ where T_S is surface temperature. The proportionality factor Γ in the equation is obtained by calculating T_M using a sample of temperature and absorption profiles and correlating it with T_S. A standard error of about 3 *K* is obtained with proportionality factors of 0.93, 0.94 and 0.96 at the radiometer center frequencies of 3.9, 11.7 and 20.5 GHz, respectively.

At very low frequencies, or at very high altitudes $\tau \approx 1$ so that equation (5) results in $T_{SKY} = T_{CB} = 2.7$ *K*. In general, however $\tau < 1$ so that $T_{SKY} > T_{CB}$ and one must determine T_{SKY} from measurements or model calculations. Under cloud free conditions microwave radiation is absorbed by molecular oxygen and water vapor. The measured transmittance due to water vapor and oxygen was first obtained by radiometers using the so-called tipping curve procedure[1] described in Dicke's 1946 seminal paper (*Phys. Rev.* 70, 340–348). This novel procedure uses clear sky radiometer measurements at two or more elevation angles to derive the transmittance and calibrate microwave radiometers. This same approach is used today where details on its application is given in Appendix A11. The tipping curve procedure is also applied in Chapter 8 to measure the transmittance and calibrate the 20 GHz radiometer.

The effects of atmospheric absorption of cosmic radiation and the emission by water vapor and oxygen is shown in Figure 13. This Figure plots the simulated cloud free sky brightness temperature for a zenith viewing radiometer as a function of frequency between 3 and 22 GHz with total precipitable water (*TPW*) as a parameter. The simulations use (5) with the transmittance and mean temperature calculated using the

[1] The procedure is based on (5) which can be written as $\ln\left[\dfrac{T_M - T_{SKY}(\theta)}{T_M - T_{CB}}\right] = Sec\,\theta \ln\tau$. Differentiating with respect to $Sec\,\theta$ we obtain $\dfrac{d\ln[T_M - T_{SKY}(\theta)]}{d\,Sec\,\theta} = \ln\tau = -\alpha$ where α = opacity.

latest absorption models of oxygen and water vapor as developed by Dr. Philip Rosenkranz who is now retired from MIT. Three different vertical soundings of temperature and water vapor were used in calculating the sky brightness temperature.

The nearly flat frequency response shown in Figure 13 in the absence of water vapor (*TPW* = 0 mm) is due to the 2.7 *K* cosmic radiation in addition to the non-resonant oxygen absorption whose strong resonant lines occur between 50 and 70 GHz. Atmospheric emission due to oxygen is comparable to the cosmic radiation of 2.7 *K* so that the brightness temperature increases to 5.0 *K* for the 4 GHz radiometer and 6.6 *K* for the 20 GHz radiometer whose center frequency is at 20.5 GHz. A much larger increase occurs due to water vapor emission which increases T_{SKY} as a function of *TPW* with the peak response occurring at the center of the water vapor line at 22.235 GHz. Water vapor emission is shown to be negligible at 4 GHz, but increases the brightness temperature an additional 5 *K* at 12 GHz, and 55 *K* at 20.5 GHz for tropical atmospheres where the water vapor amount can reach 60 mm or more. As such, it is important to include this atmospheric radiation for accurate calibration using sky measurements. The next Section describes the cold sky calibration procedure used for the 4 GHz radiometer.

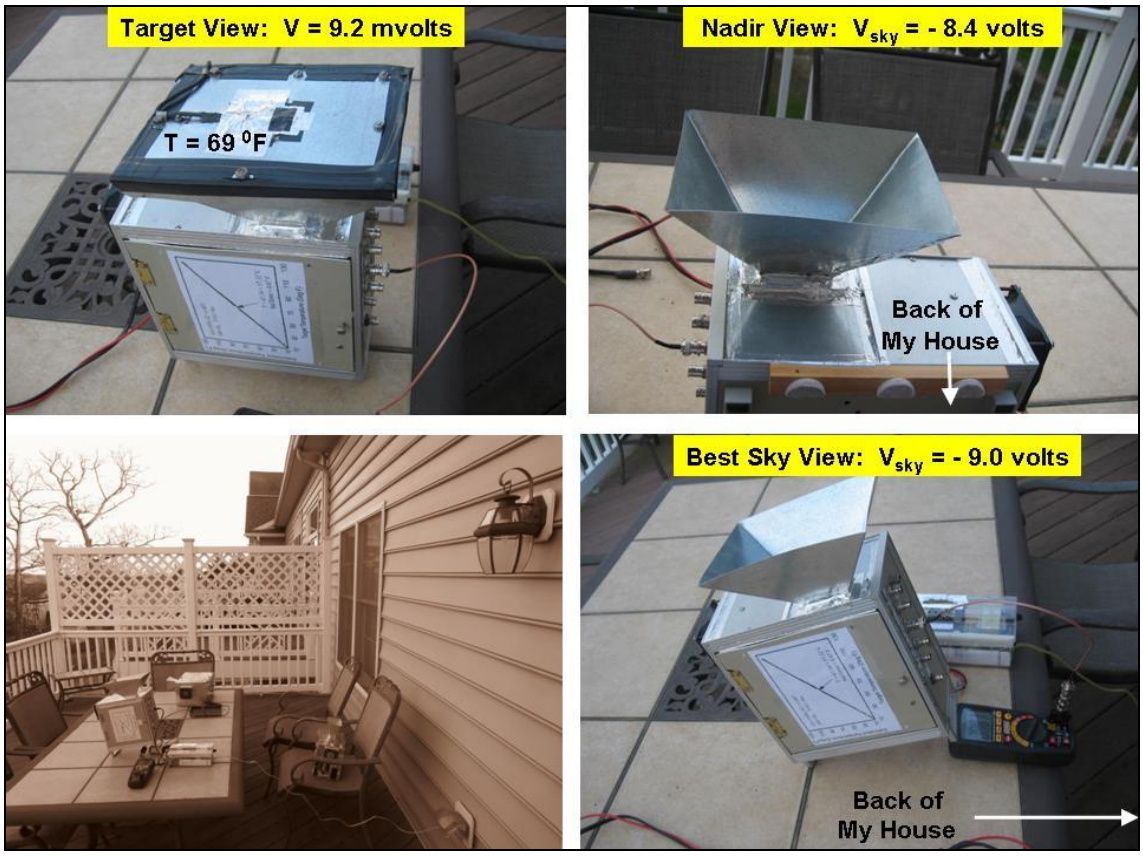

Figure 11 - The bottom-left shows the 4 GHz radiometer taking sky measurements from my patio deck. An enlarged picture is shown in the bottom-right. Calibration begins by placing the target over the antenna and setting the radiometer output to nearly zero volts by adjusting its fine offset (Top-Left). The top-right shows a sky measurement of -8.4v at nadir viewing while the bottom-right shows it reduced to -9.0v by rotating the antenna by 90 degrees and directing the antenna away from the back of my house. The target temperature is 69 ^{0}F so that assuming the sky radiation is at 2.7 *K* (-455 ^{0}F), the radiometric gain becomes (455+69)/9 = 58.2 ^{0}F/V. Radiometer parameters for these measurements are G_1=1930, G_2=1.7, G_d=10 and τ_{INT}=0.1 seconds.

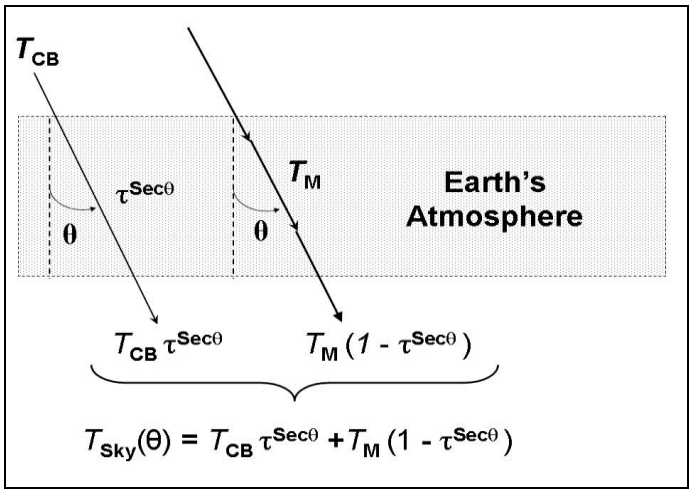

Figure 12 - Sky brightness temperature T_{SKY} received by a ground-based radiometer. T_{SKY} consists of the cosmic background T_{CB} and atmospheric radiation emitted at mean temperature T_M with effective emissivity $1-\tau^{Sec\theta}$. The cosmic radiation is also attenuated by the transmittance τ whose exponent $Sec\theta$ accounts for the increased slant path at zenith angle, θ.

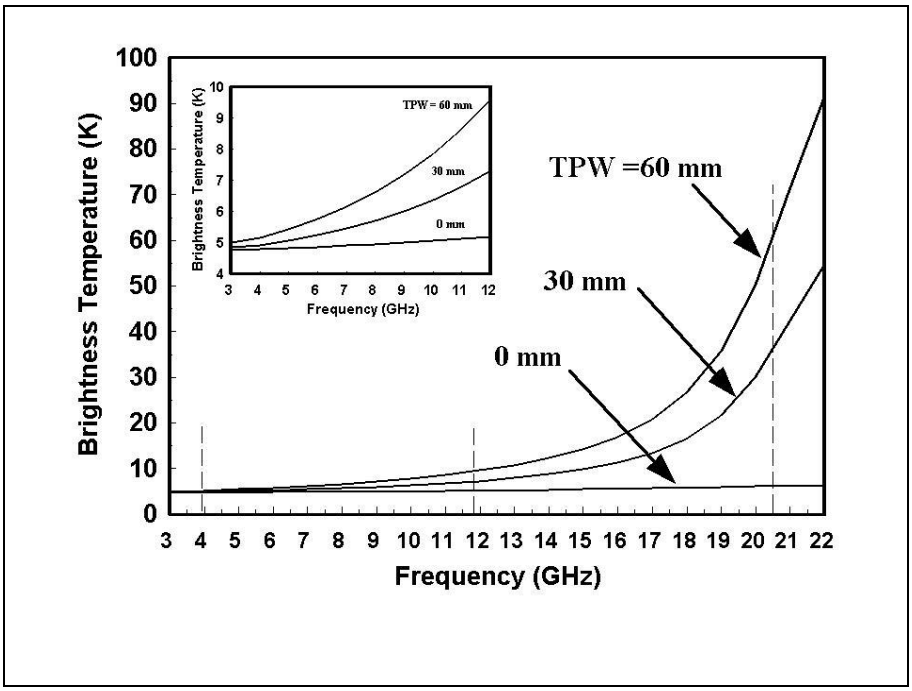

Figure 13 - Simulated brightness temperature for cloud free atmospheres as a function of frequency for different amounts of water vapor (*TPW*). Vertical lines identify the center frequencies of the 4, 12 and 20 GHz radiometers which is at 3.9, 11.7 and 20.5 GHz, respectively. The insert is an expanded plot for frequencies less than 12 GHz.

4.2 Sky Calibration Measurements

Under cloud-free and dry atmospheric conditions it is relatively quick and easy to measure the offset and gain calibration parameters in equation (3). To assure accurate sky measurements, the antenna is moved around nadir to see if any antenna contributions

arise from surrounding objects. Figure 11 (Bot-Left) shows the sky radiation calibration measurements taken from my patio deck using the 4 GHz radiometer. The procedure begins as shown in the top-left figure, where the high emissivity target is placed over the antenna while the radiometers fine offset control is adjusted to produce a near zero output voltage for the ambient target temperature of 69 ^{0}F. The top-right figure shows the target removed so that the radiometer views space with the antenna directed at nadir. For this particular orientation, the antenna pattern seen by the back of my house contains the larger beamwidth of 28.7 degrees. This results in maximum earth radiation reflected off the back of my house into the antenna field of view (FOV). The corresponding radiometer measurement is shown to be -8.4v.

The bottom of Figure 11 shows the antenna rotated 90 degrees so that the smaller beamwidth of 25.5 degrees is directed toward my house. Furthermore, the antenna is slanted away from the back of my house, so that the combined changes reduce the earth radiation scattered into the antenna FOV. As such, the radiometer measurement is decreased from -8.4v to -9.0v. Therefore, if the sky radiates at the cosmic background temperature of 2.7 *K* (-455 ^{0}F), the radiometric gain is (455+69)/9 = 58.2 ^{0}F/volt. This gain decreases to 57.7 ^{0}F/volt or by about 1 % when including the 2 *K* (3.6 ^{0}F) increase in sky temperature due to oxygen emission. The radiometer parameters associated with these measurements is G_1=1930, G_2=1.7, G_d=10 and τ_{Int} = 0.1 seconds. Nearly the same radiometric gain was obtained using the variable target temperature method described before. Also, compared to sky measurements at 4 GHz, the narrow 16 degree beamwidth of the 12 GHz radiometer results in much smaller effects due to the surrounding earth radiation scattered into the antennas FOV. Calibration of the 12 GHz radiometer with nearly the same radiometric gain was obtained using the cold sky procedure and setting the instrument parameters as G_1= 286, G_2=1.4 and G_d=10.

The next Chapter briefly outlines the effect of gain variation on a Dicke and total power radiometer. This is followed by an experiment in Chapter 6 showing the sensitivity of a Schottky diode detector to temperature variation, and its effect on the Dicke radiometer performance. The temperature effect is shown to be greatly pronounced when the radiometer views cold space. Therefore, a temperature compensated detector such as that shown in Figure A5 was used to reduce this effect. Unless specifically mentioned, all of the measurements described here use the finalized design shown in Figures 3 and 4 which use a temperature compensated detector.

5. Gain Variation Effect

The simplest radiometer, called a total power radiometer, measures microwave radiation without the synchronous detection components (*i.e.*, switch, demodulator and clock) in Figures 3 and 4. As a result, temperature instability of the radiometer output is found at very high gain (*e.g.*, 150 dB). This instability occurs due to gain variations as well as variations in the LNB noise figure with temperature which sets a practical limit on the maximum usable gain in the system. As mentioned previously, Dicke type radiometers used here reduce the noise and output drift due to such gain variations by switching the antenna input from the scene to a stable reference load and differencing the output signals using a synchronous demodulator. Alternatively, the difference operation can be performed digitally. The requirement is that the gain is stable within the switching times,

i.e., $f_{switch}\ \tau_{Int} > 1$ where f_{switch} is the switching frequency and τ_{Int} is the integration time. I found no problem using the radiometers lowest switching frequency and smallest integration time, *i.e.*, f_{switch} = 173 Hz and $\tau_{In\,t}$ = 0.1 seconds.

The downside of a Dicke radiometer compared to a total power radiometer is as follows;

(A) Thermal fluctuations in the radiometer output is increased by 2 relative to a total power radiometer since a Dicke radiometer views the antenna, T_A in half the integration time of a total power radiometer, *i.e.*,

$$\Delta T_b \rceil_{Total\ \ Power} = (T_A + T_N)\sqrt{\frac{1}{B\tau_{\text{int}}} + \left(\frac{\Delta G}{G}\right)^2}, \qquad (7a)$$

$$\Delta T_b \rceil_{Dicke} = \sqrt{\frac{(T_A + T_N)^2 + (T_R + T_N)^2}{B(\tau_{\text{int}}/2)} + \left(\frac{\Delta G}{G}\right)^2 (T_A - T_R)^2} \qquad (7b)$$

so that for no gain variation, $\Delta G = 0$ and for $T_A = T_R$, $\Delta T_b \rceil_{Dicke} = 2\ \Delta T_b \rceil_{Total\ Power}$.

Equations (7a) and (7b) are the minimum detectable change or noise equivalent temperature, NEΔT, of each radiometer. The corresponding voltage fluctuation is $\Delta V = kGB\ \Delta T_b$ where k is Boltzman's constant, B is the *IF* bandwidth and the radiometer gain G is $G_{LNB}\ G_{Amp}\ G_{Syn}\ \gamma_{det}$ where γ_{det} is the detector sensitivity. Also, as evident from (7b), the contribution due to gain variation can be removed using a null balancing radiometer which uses feedback to minimize the output, T_A - T_R, by adding noise of sufficient amplitude to T_A. However, this approach requires additional electronics and was not used here since the reduction in drift and gain variations using an unbalanced Dicke radiometer was found to be sufficient.

(B) Sensitivity to input change is reduced by 2 relative to a total power radiometer, *i.e.*, the block diagram shows $V)_{Dicke} = kGB\ (T_A - T_R)/2$ while $V)_{Total\ Power} = kGB\ T_A$ so that $(\Delta V/\Delta T_A)_{Dicke} = 1/2\ (\Delta V/\Delta T_A)_{Total\ Power}$.

However, this factor of 2 reduction in sensitivity is greatly offset by the reduced drift and reduced gain effect of a Dicke radiometer compared to a total power radiometer.

6. Detector Response

In addition to the LNB, the detector is critical in determining the radiometer performance. Not only does the detector define the linearity of the radiometer, it can also affect the overall gain, bandwidth and temperature dependence of the radiometer. These issues are discussed in this Chapter.

A dual packaged Schottky diode series detector element, model HSMS 2862, was chosen because of its high sensitivity at microwave frequencies. The diode sensitivity, γ_{det}, is listed as 50 mv/μw at 1 GHz, decreasing to 25 mv/μw at its highest frequency of 6 GHz.

This decreased sensitivity with frequency results from the diode's intrinsic capacitance which is specified to be about 1 pf. Furthermore, as described later in Chapter 8 (see Figure 29), stray capacitance and inductance further reduces the sensitivity and frequency response when the Schottky diode is connected in a more complete circuit that includes a difference amplifier for temperature compensation and a multiplexer to supply DC power to the LNB and extract its *IF* signal. Before discussing the temperature effect, a brief overview is given next of the detector's square law response.

The bottom-left of Figure 14 shows the detector connected in a voltage doubler circuit along with pictures of the opened and enclosed unit used in an early 4 GHz radiometer. For illustration, the bottom-right of the Figure displays a representative detector response, showing a Log-Log plot of the input power against the output voltage. Note that to ensure a square law response so that the radiometer voltage is linearly proportional to power or brightness temperature, the diode input power should be kept below -15 dBm with an output voltage below 100 mv. This will be discussed more fully in the next Section 6.1.

While the detector's frequency response and input power level affect the overall gain and linearity of the radiometer, its sensitivity is found to be highly temperature dependent do to the intrinsic characteristic of Schottky diodes. This can result in poor performance if not accounted for. The effect on the radiometer performance can be seen by the output voltages shown in the block diagrams of Figure 3 and 4, *i.e.*,

$$V)_{Dicke} = \tfrac{1}{2} k G' B \gamma_{\det} [T_A - T_R] \,, \qquad (8a)$$

$$\frac{\Delta V)_{Dicke}}{\Delta T_{\det}} = \tfrac{1}{2} k G' B [T_A - T_R] \frac{\Delta \gamma_{\det}}{\Delta T_{\det}} \quad , \qquad (8b)$$

$$where \quad G' = G_{LNB}\, G_{Amp}\, G_{Syn} \cdot \qquad (8c)$$

From (8b), we see that the temperature variation of a Dicke radiometer occurs due to changes in detector sensitivity. Furthermore, the temperature variation occurs primarily when viewing cold space since then $T_A << T_{Ref}$. Conversely, the temperature variation is much less when viewing the warmer ground temperatures since then T_A is comparable to T_R. To demonstrate these features, measurements were performed using an earlier 4 GHz radiometer which uses the uncompensated detector shown in Figures 14 and 15. As shown in Figure 16, the radiometer is mounted on top of the 12 GHz radiometer and placed on a movable cart that is elevated so that the antenna views space through my basement glass patio door. During the experiment the detector temperature is heated by about 25 ^{0}F for a short time using a small incandescent light. For the first 90 minutes the high emissivity target is placed over the antenna as in Figure 9, and then removed for about 60 minutes so that the antenna views space.

The two top plots in Figure 17 show the radiometer voltage (Left) and detector temperature (Right) as a function of time. Note the abrupt decrease in radiometer voltage when the detector is heated while the antenna views space at the time of 125 minutes. No change is seen at the earlier time of 75 minutes when the antenna views the high emissivity target. The bottom left figure shows the measurements viewing space on expanded scales, while the bottom right figure shows the corresponding voltage plotted against detector temperature. Using regression analysis, a linear equation is obtained between the voltage and detector temperature that has a slope of -0.1 Volts/^{0}F. Also,

using the detector temperature as input, the voltage derived from this equation is shown to accurately reproduce the true measurements in the bottom left figure. What is also noteworthy is how well the radiometer voltage follows the detector temperature even though the temperature sensor is mounted outside of the detector case as shown in Figure 15. In fact, much of the difference between the two measurements seen in the bottom-right figure is due to the time lag between the outside temperature change and detector response. A more dramatic example of this time lag between the measured temperature and detector temperature response will be displayed in the next Section when testing a temperature compensated detector.

The results shown in Figure 17 are in qualitative agreement with equation (8b), which shows the slope of voltage versus detector temperature, *i.e.*,

$$\frac{\Delta V)_{Dicke}}{\Delta T_{\rm det}} = \tfrac{1}{2} k G' B [T_A - T_R] \frac{\Delta \gamma_{\rm det}}{\Delta T_{\rm det}} \quad .$$

Note that, as in the measurements, the slope is negative when viewing space since then $T_A < T_R$, and becomes negligibly small when viewing the high emissivity target since then $T_A \cong T_R$. It should be mentioned that I initially observed the detector problem by viewing space while warming the detector with my fingers as shown in Figure 15. I originally thought that the temperature stability issue was due to the LNB amplifier, whose gain can be temperature dependent. However, after heating the LNB in the same manner as the detector and finding no effect, I concluded that the issue was not the LNB but solely due to the detector.

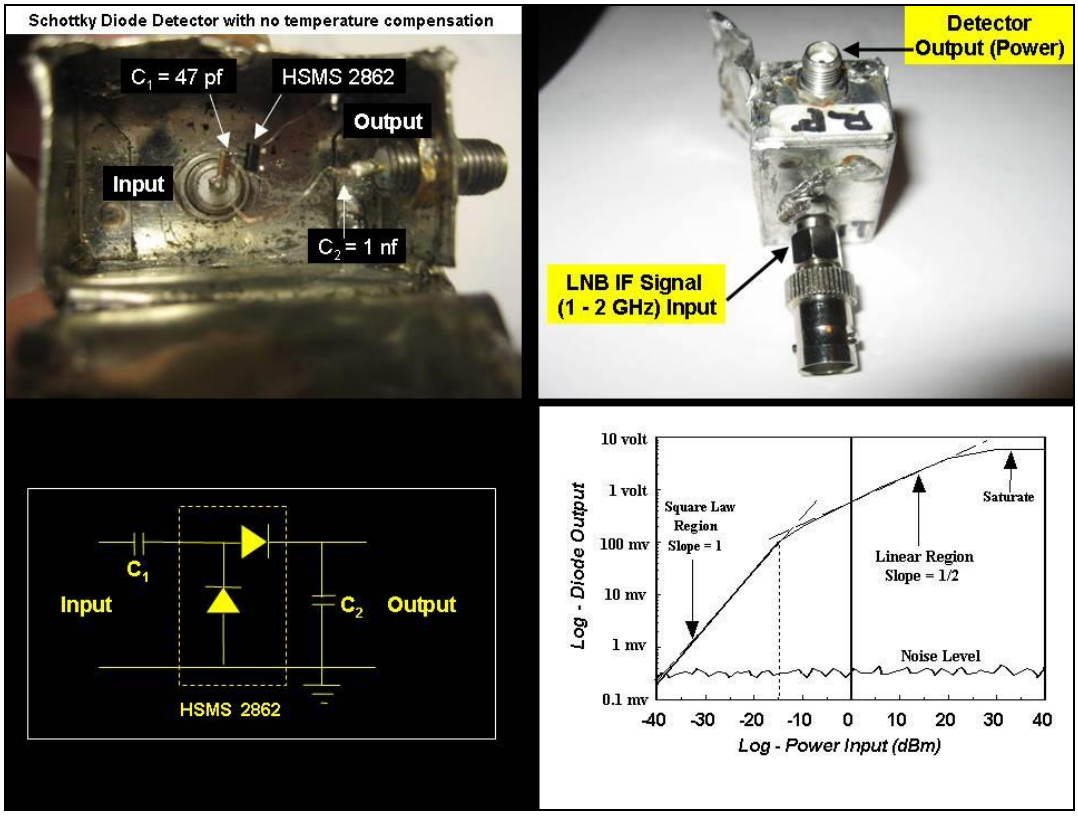

Figure 14- The HSMS 2862 Schottky diode chip contains two elements connected together to double the sensitivity. The circuit is shown in the bottom-left, while the open unit (top left) shows the labeled components of the detector (top right) that are wire connected. The bottom-right shows the generic detector response on a Log-Log plot. It shows the regions for which a diode displays a square law and linear response. Note that to assure a square law response the input power must be below -15 dBm so that the diode's output voltage is less than 100 mv.

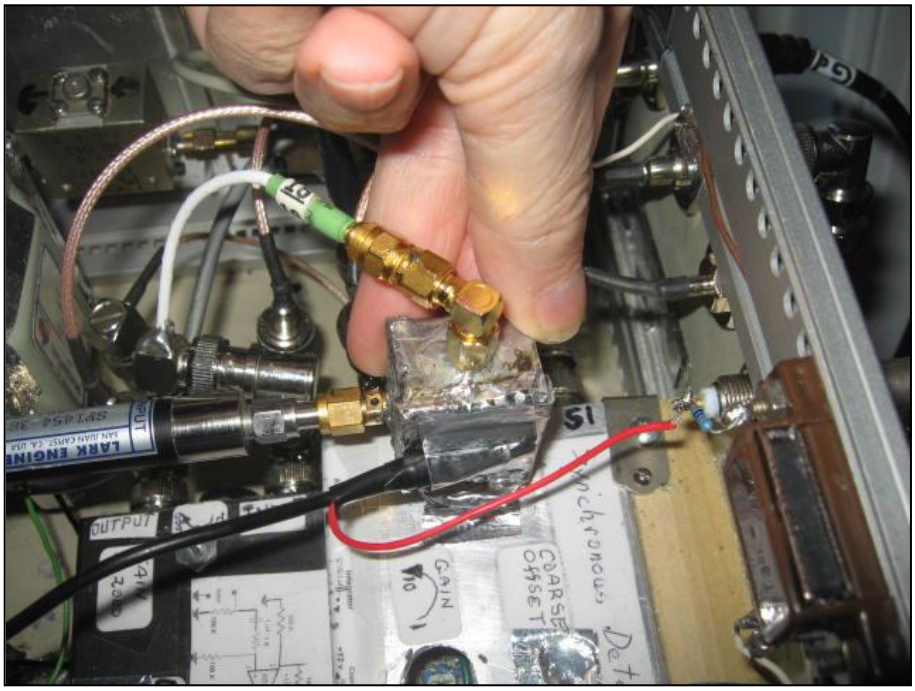

Figure 15- Earlier 4 GHz radiometer uses the uncompensated detector in Figure 14, whose temperature is monitored using a thermocouple attached to its outer case.

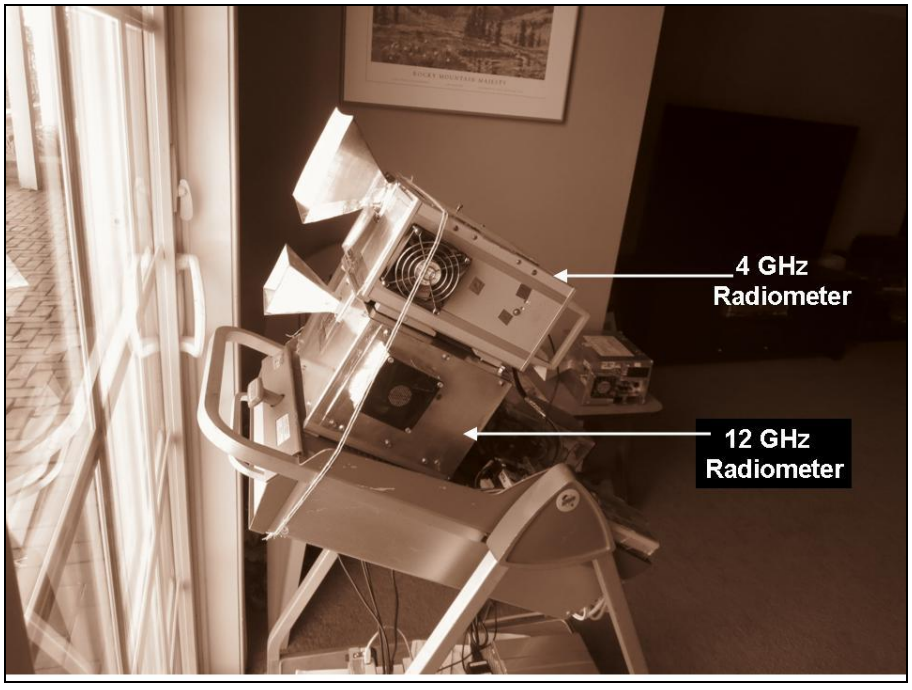

Figure 16- The 4 and 12 GHz radiometers view space through a glass patio door.

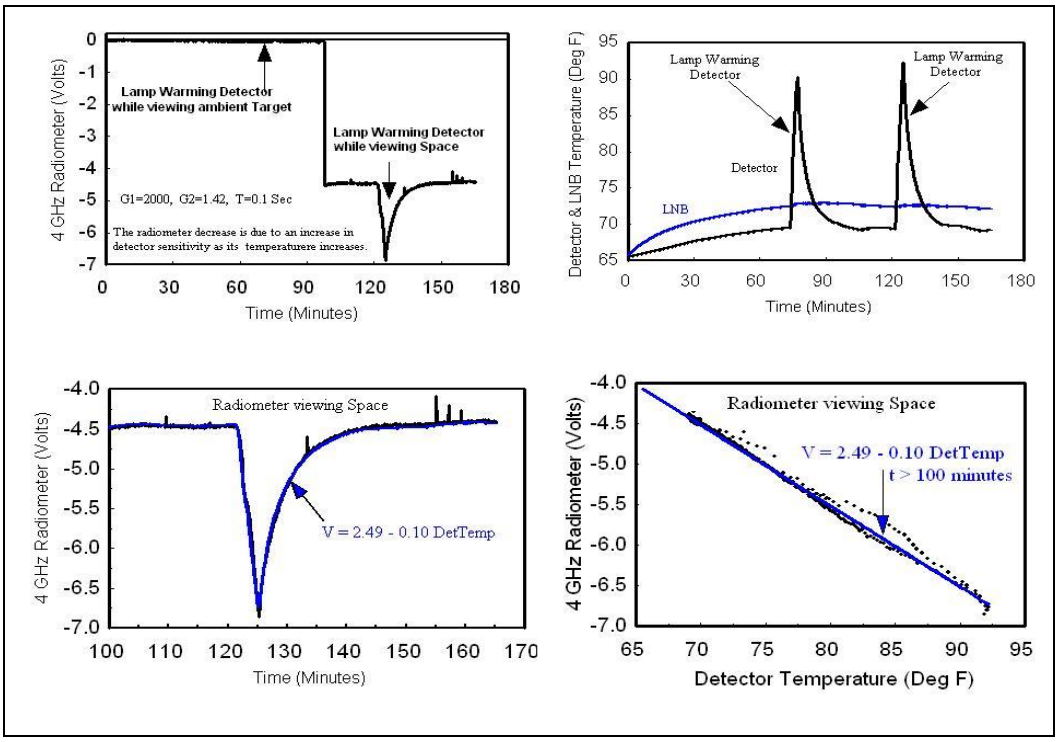

Figure 17- Earlier 4 GHz radiometer with uncompensated Schottky diode detector displays the detector temperature effect. The top-left figure shows the radiometer voltage when the antenna views the high emissivity target followed by the space view. The top-right figure shows the detector and LNB temperatures. The bottom-left figure shows the space viewing measurements while the bottom right figure plots these voltages against detector temperature.

6.1 Detector Temperature Compensation

Upon realizing that the detector is highly temperature sensitive, I decided to use a temperature compensated Schottky diode detector rather than the alternative, which is to use a tunnel diode detector that is less temperature dependent but also has much smaller sensitivity. The circuit uses a matched pair of Schottky diodes connected to a difference amplifier. As discussed in Appendix A5, one diode section is used as reference while the other is connected to the input, which is the LNB *IF* output signal. The difference output then approximately cancels the temperature effect since both diodes operate at nearly the same temperature.

Figure 18 shows the finalized 4 GHz radiometer with the compensated detector while Figure 19 (Bot left) shows the overall response of the detector. The response was determined by connecting a signal generator to the input and measuring the output in millivolts (mv) as the input power was increased from 0.1 microwatts (–40 dBm) to 1 milliwatt (0 dBm). The frequency was set at 1.4 GHz, which is near the center of LNB *IF* bandwidth. Figure 19 (Bot right) shows that for input power levels between -30 dBm (1 μw) to -12 dBm (63 μw), a linear relationship exists between input power and output voltage with a maximum error of +/- 0.2 dBm., *i.e.*,

$$P(\mu w) = -0.6 + 0.2\, V(mv), \qquad (9a)$$

$$V(mv) = 3.0 + 5.0\, P(\mu w), \qquad (9b)$$

Equation (9b) was obtained by inverting (9a), and shows a detector sensitivity of 5 mv/μw for input power within the above mentioned 18 dBm range. This detector sensitivity includes the difference amplifier gain of 10. Also, for completeness, the two plots on the top of Figure 19 compare the above equations with the measurements over a 250 mv output range. From these sets of measurements it is evident that to insure a linear detector response, the input signal strength must be such that the output detector voltage is less than about 200 mv or the input power is less than 40 μw. The output voltage must also be greater than about 8 mv, corresponding to input power greater than 1 μw. Also, not to be overlooked is the detectors frequency response, which can define the overall frequency characteristic of the radiometer. This point was mentioned previously and shown in Figure 29 of Chapter 8 for the 20 GHz radiometer detector.

The 4 GHz radiometer response is again measured after substituting the temperature compensating detector as shown in Figure 18. For this experiment, the 4 GHz radiometer is subjected to the same type of measurements as before. Since the temperature compensated detector has a different gain than the uncompensated detector, the improved radiometer was calibrated to have the same radiometric gain as the earlier unit. As shown in Figure 20 (Top right), the detector temperature is now increased by 55 ^{0}F using the small incandescent lamp. Also, unlike before, the radiometer voltage now increases (Figure 20 Top Left) rather than decreases as its temperature increases. More importantly, Figure 20 (Bot) shows that the radiometer temperature sensitivity is +0.01 V/^{0}F whereas before it was –0.10 V/^{0}F using the uncompensated detector. This factor of 10 improvement in stability using a temperature compensated detector was implemented for the 12 GHz radiometer (see Figure 3) as well as the 4 GHz Dicke radiometer of Figure 4. Also note in Figure 20 a small wave-like displacement between the radiometer response and the detector temperature change. This delayed radiometer response in the top-left and bottom plots occurs because the temperature sensor is mounted to the detector case, which is at a different location, and therefore at a slightly different temperature than the detector element. A similar effect was mentioned when discussing Figure 17, where again a time lag was evident between the two measurements

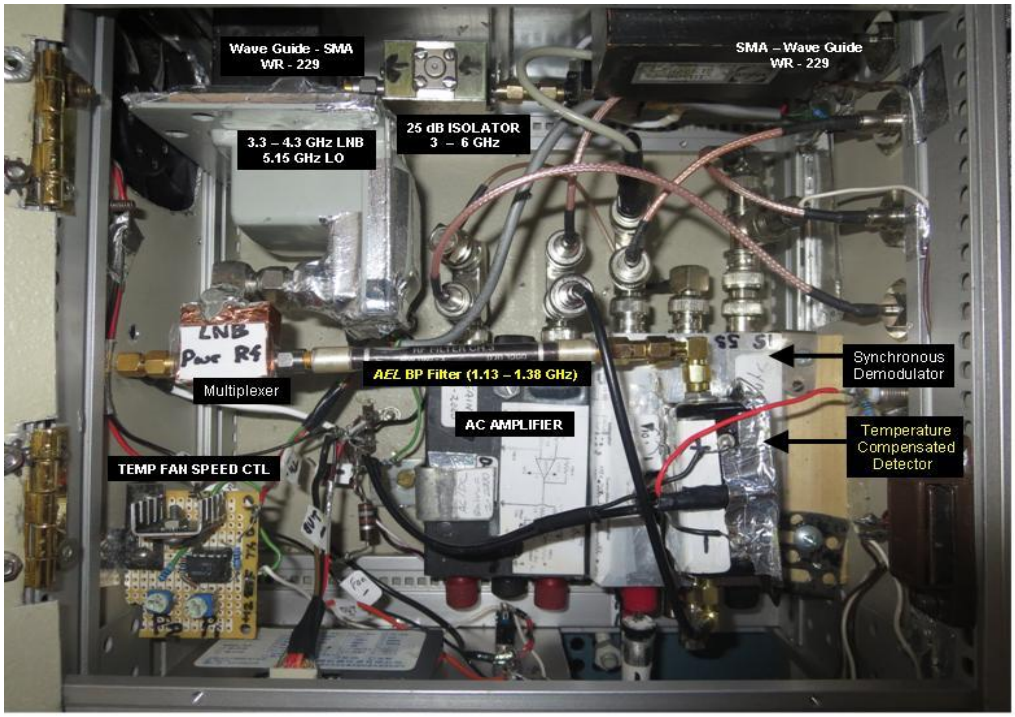

Figure 18- Finalized 4 GHz radiometer has a temperature compensated detector. The labeled components are shown here as well as in the block diagram of Figure 4.

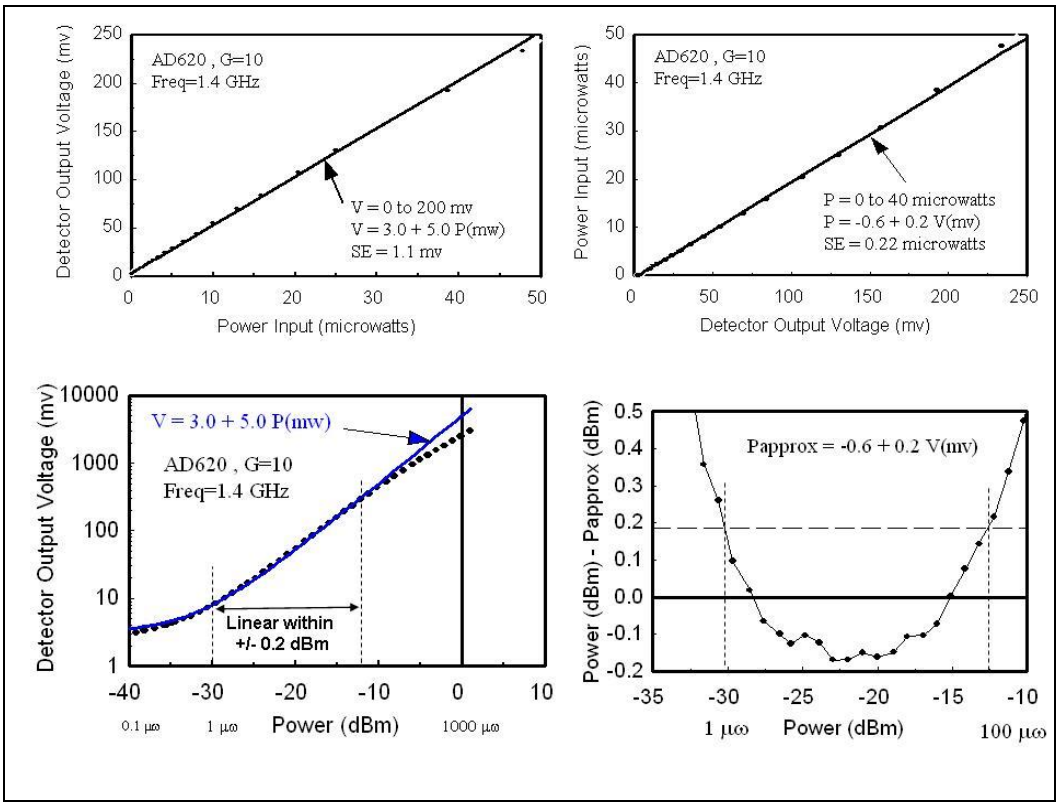

Figure 19- Measurements of 4 GHz radiometer detector at 1.4 GHz with the AD620 amplifier gain set to 10. The top-left shows the detector output voltage as a function of input power, while the adjacent figure shows the inverse relationship. The bottom-left shows the detector output voltage varies linearly with input power over a -30 to -12 dBm range, with a +/- 0.2 dBm accuracy (bottom-right). However, as shown in the bottom figures the detector becomes greater than the power law at very low levels and is closer to linear at high levels. A similar response is shown in the illustrative example shown in Figure 14 (bottom-right).

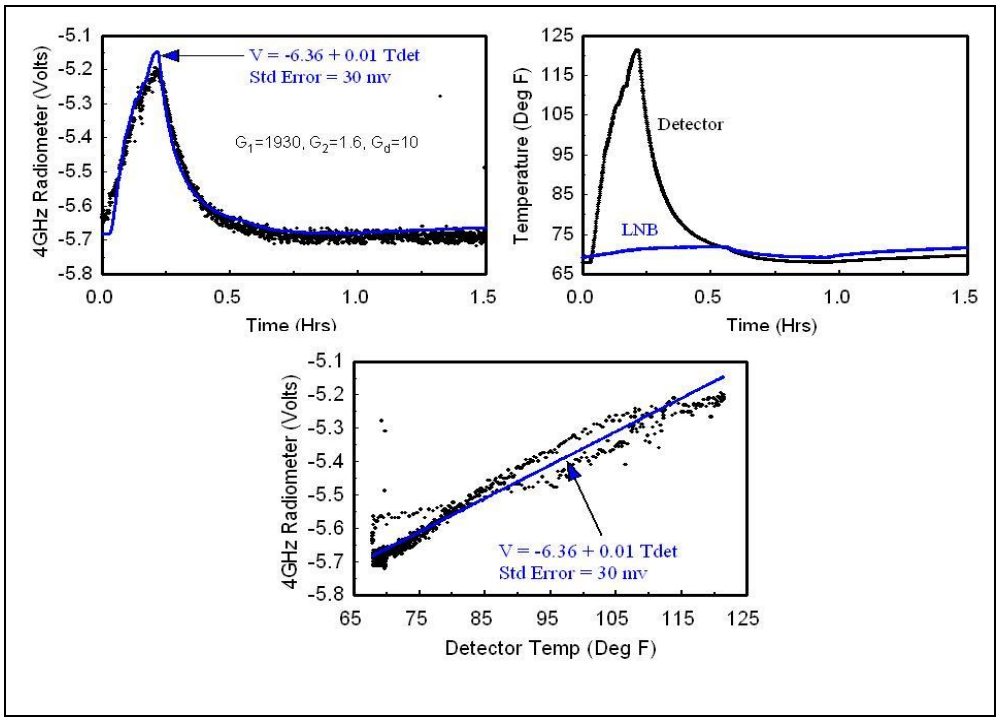

Figure 20 - 4 GHz radiometer with a temperature compensated detector displays a reduced temperature effect compared to the uncompensated detector shown in Figure 17. As in Figure 17, the radiometer views space while the detector temperature is increased by 55 ^{0}F using an incandescent lamp. The top-left shows the radiometer voltage increasing with detector temperature (top-right) with a sensitivity of + 0.01 V/^{0}F (bottom). This sensitivity is 10 times less than the uncompensated detector whose temperature sensitivity is -0.10 V/^{0}F.

7. Radiometer Applications

Much time was spent in developing and testing the radiometer performance, followed by an occasional experiment to demonstrate their use in earth remote sensing. Examples of some sky and ground viewing measurements using the 4 and 12 GHz radiometers are described in this Chapter. The measurements will also be compared with models to help explain the observations and examine the different radiation contributions. To minimize the smoothing of observations all measurements were obtained at the smallest integration time of 0.1 seconds.

As shown in Figure 16, the two radiometers are mounted above each another and placed on a movable cart that can be elevated to either view the ground or sky at an adjustable angle. All measurements were done in my basement, viewing the outside radiation through a sliding glass patio door. Unfortunately, glass is not transparent to microwaves but reflects the outside radiation. However, while the glass door is a poor substitute for a radome, it is a convenient way to shield the radiometers from the environment, particularly when taking rain measurements. A better alternative, although not as convenient, would be to enclose the radiometers in a more transparent Styrofoam enclosure so that the instruments could be placed outdoors as when performing calibration measurements. This Chapter describes the surface and atmospheric observations along with analysis showing the effect glass has on the measurements. The

analysis of the glass effect also explains in some detail how to model the radiation transfer through lossless dielectric media.

7.1 Surface Viewing Measurements

Since the radiometers view the ground through a glass door, the brightness temperature measurement at frequency ν is given by the three components shown in Figure 21, *i.e.*,

$$T_b(\nu) = \Im_g [\varepsilon_S T_S + (1-\varepsilon_S) T_d] \; + \; \varepsilon_g T_g \; + \; R_g T \qquad (10a)$$

$$\text{where} \quad \varepsilon_g = \alpha_g = 1 - R_g - \Im_g \; . \qquad (10b)$$

The largest quantity in (10a) is the surface emission term $\varepsilon_S T_S$. where ε_S is the surface emissivity and T_S is its temperature. Both ground-based, aircraft flown and satellite launched radiometers have been used to measure the emissivity of different surfaces. For reference, Figure 22 shows the average emissivity for different surfaces as a function of frequency. Note that the highest emissivity of 0.95 occurs over vegetated land while the lowest emissivity of about 0.40 occurs for water and flooded land surfaces. The other terms in (10a) account for the absorption, reflection and transmission of radiation by the glass where α_g is the absorption coefficient, R_g is the reflection coefficient and $\Im_g$ is the transmission coefficient. These terms are related by energy conservation using (10b) where by Kirchoff's law $\varepsilon_g = \alpha_g$ is the glass emissivity. Also contained in (10a) is the glass temperature, T_g, and basement temperature, T, which multiplies the glass emissivity and reflectance quantities, respectively. Equation (10a) and Figure 21 shows how the surface emission is attenuated by the glass transmission coefficient.

The transmission coefficient, $\Im_g$, is the fraction of radiant energy transmitted through the glass while the reflection coefficient, R_g, is the fraction of radiant energy reflected by its surface. Also included in (10a) is the thermal emission at temperature T_g due to absorption, which is defined by the glass emissivity ε_g given by (10b). The last term contains the in-house radiation at temperature T that is reflected into the antenna FOV. Equation (10a) implicitly assumes that no sky radiation is directly observed when viewing the ground, such as by way of the antenna side lobes. However it does include the downwelling atmospheric or sky radiation, T_d, reflected by the ground. For smooth (*i.e.*, specular) surfaces, the reflectivity is 1-ε_S so that the reflected radiation is (1-ε_S)T_d, which is added to $\varepsilon_S T_S$ in equation (10a). As mentioned in the next Section and illustrated in Section 8.2, the largest values of T_d occurs during rain events, but even then, the reflected signal is small over high emissivity land surfaces. Therefore, this term will be omitted later since the atmosphere was rain-free when viewing the ground.

As mentioned in Appendix A1, the antenna receives vertical polarization to reduce surface reflections. The dielectric constant of glass is reported to be about 6. As such, its reflection coefficient decreases from 0.18 at nadir to 0.16 at vertical polarization for the approximate 20 degree viewing angle used when viewing the ground. These calculations are for an infinitely deep interface so they do not include the frequency variation resulting

from multiple reflections within the glass sheet. More exact calculations will be presented later. Since the dielectric loss of glass is very small at microwave frequencies the glass can be considered lossless. As such, the glass is mostly reflective with its emissivity or absorptivity nearly zero so that $R_g + \Im_g \approx 1$. Equation (10a) then becomes

$$T_b(\nu) = (1 - R_g)[\varepsilon_S T_S + (1 - \varepsilon_S) T_d] + R_g T \qquad (11)$$

where the frequency dependence is due to the reflection coefficient. Furthermore, as mentioned above, the downwelling reflected radiation is negligible so that (11) reduces to

$$T_b(\nu) = (1 - R_g)\,\varepsilon_S T_S + R_g T. \qquad (12)$$

To begin the analysis, Figure 23 (Bottom left) shows surface measurements taken over a 5 hour period beginning at 7 pm on August 8, 2013. The voltage is seen to decrease steadily over this time period, presumably due to decreasing outside temperature. Unfortunately, I did not take any outside ground temperature measurements to verify the temperature decrease. However, upon plotting the 4 GHz against 12 GHz measurements in Figure 23 (Bottom Right) a slope of 3.1 is obtained using linear regression with a standard error of 5 mv using sample averaged measurements. As shown next, the larger decrease observed at 4 GHz compared to 12 GHz is consistent with a smaller reflection coefficient at 4 GHz compared to 12 GHz.

Using (12), the equation relating the radiometer measurements is

$$\mathrm{T_b}(4) = \mathrm{S\ T_b}(12) + [\mathrm{R_g}(4) - \mathrm{R_g}(12)\mathrm{S}]\,\mathrm{T} \qquad (13a)$$

$$\text{where} \quad \mathrm{S} = \left[\frac{1 - \mathrm{R_g}(4)}{1 - \mathrm{R_g}(12)}\right] \frac{\varepsilon_S(4)}{\varepsilon_S(12)} \cong \frac{1 - \mathrm{R_g}(4)}{1 - \mathrm{R_g}(12)} \qquad (13b)$$

The ratio between the 4 and 12 GHz brightness temperatures in (13a) is given by the slope, *S*, in (13b). As indicated by (13b), this slope is mainly a function of the glass reflection coefficients since the emissivity over vegetated land approaches unity at both 4 and 12 GHz. Even for flooded land the emissivity is calculated to increase from 0.38 at 4 GHz to 0.40 at 12 GHz so that the emissivity ratio in (13b) is 0.95. Furthermore, (2b) shows that T_b is linearly related to voltage so that the slope of 3.1 obtained in Figure 23 can be compared with the slope given by (13b), which will be determined next using reflection measurements.

In a separate insertion loss experiment described in Appendix 9, the reflection coefficient at normal incidence was obtained by measuring the radiometer voltages after opening and closing the glass door. Neglecting glass absorption, the reflection coefficient at 4 and 12 GHz is shown to be 0.20 and 0.64, respectively. As such, the T_b ratio from (13b) is 2.2, which is less than the measured slope of 3.1 in Figure 23. More will be said later about this difference but first we will examine the reflection measurements.

The 4 GHz reflection coefficient of 0.20 is comparable to the 0.16 estimate denoted before which is based on a dielectric constant of 6, so that the 12 GHz reflection

coefficient of 0.64 appears unreasonable. However, as mentioned above, the glass reflectance was calculated for an infinitely deep medium and therefore did not have frequency variations due to multiple reflections within the glass. This effect would be larger at the higher frequency where the largest discrepancy occurs. To examine this, Dr. Philip Rosenkranz provided much analysis in addition to calculating the reflection coefficient for a 2.5 mm single piece of glass using the dielectric constant of 6. The reflection coefficient is found to be a strong function of the frequency and glass thickness product. The reflection coefficient is also somewhat larger for a larger dielectric constant.

A summary of the insertion loss measurements and calculations is given in Table 1. The calculated reflection coefficient at normal incidence is 0.20 at 4 GHz, increasing to 0.51 at 12 GHz. For the 20^0 viewing angle used when observing the ground the calculated reflection coefficient is reduced to 0.17 at 4 GHz and 0.47 at 12 GHz. However, since the glass door actually contains of two glass panes separated by an air gap or spacer, the reflectance varies depending on the separation distance as well as the glass thickness. In fact, calculations show it is possible to get a wide range of reflectances by fixing the dielectric constant to 6 and just varying these two parameters. As an example, Table 2 shows the reflection coefficient calculated for a glass separation of 5 mm with a glass thickness of 4 mm. Since the results are now more sensitive to frequency, the power reflection coefficients were averaged over the radiometer bandwidths because thermal noise is uncorrelated at different frequencies. Note that for the particular parameters chosen the 12 GHz calculations are now nearly the same as the measurements while the 4 GHz results are now different. Also, there is little difference for the two viewing angles.

Table 1: Reflectivity measurements and calculations for a 2 mm glass sheet.

Frequency	Measurements*	Calculation**	Calculation***
4 GHz	$R_g(0^0) = 0.20$	$R_g(0^0) = 0.20$	$R_g(20^0) = 0.17$
12 GHz	$R_g(0^0) = 0.64$	$R_g(0^0) = 0.51$	$R_g(20^0) = 0.47$

* Insertion loss measurements at 0^0 incident angle (See Figure A9 of Appendix).
** Calculated at 0^0 incident angle used in the insertion loss measurements.
*** Calculated at 20^0 incident angle used in ground and sky viewing measurements

Table 2: Reflectivity measurements and calculations for two 4 mm glass sheets separated by a 5 mm air gap.

Frequency	Measurements*	Calculation**	Calculation***
4 GHz	$R_g(0^0) = 0.20$	$R_g(0^0) = 0.11$	$R_g(20^0) = 0.13$
12 GHz	$R_g(0^0) = 0.64$	$R_g(0^0) = 0.67$	$R_g(20^0) = 0.65$

* Insertion loss measurements at 0^0 incident angle (See Figure A9 of Appendix).
** Calculated at 0^0 incident angle used in the insertion loss measurements.
*** Calculated at 20^0 incident angle used in ground and sky viewing measurements

In addition to this example where the radiometer measurements respond to changes in surface temperature, a more definitive experiment was performed on January 15, 2017 starting at 4 pm where I flooded the patio by spraying water over it and the adjoining grass area to lower its emissivity from about 0.95 to 0.37, as shown in Figure 22, without changing the temperature. As shown in Figure 24, both radiometers measure a gradual decrease as the wet area is increased, followed by a more gradually increase after the spraying was stopped and the water level slowly decreased due to runoff. As in the experiment of Figure 23, the smaller glass reflectance at 4 GHz results in a larger voltage drop due to emissivity change than that at 12 GHz.

These measurements illustrate a well known application of radiometers to detect surface wetness. However, what is difficult to explain is the smaller slope in Figure 24 (slope=1.7) compared to Figure 23 (slope=3.1). These different slopes may be due to the different viewing areas seen by the two radiometers whose antennas are displaced and have different beamwidths, *i.e.*, 27 degrees at 4 GHz and 16 degrees at 12 GHz. Since the wetness measurements depend more on area extent than the surface temperature measurements, this spatial factor can affect the results in Figure 24 more than that of Figure 23.

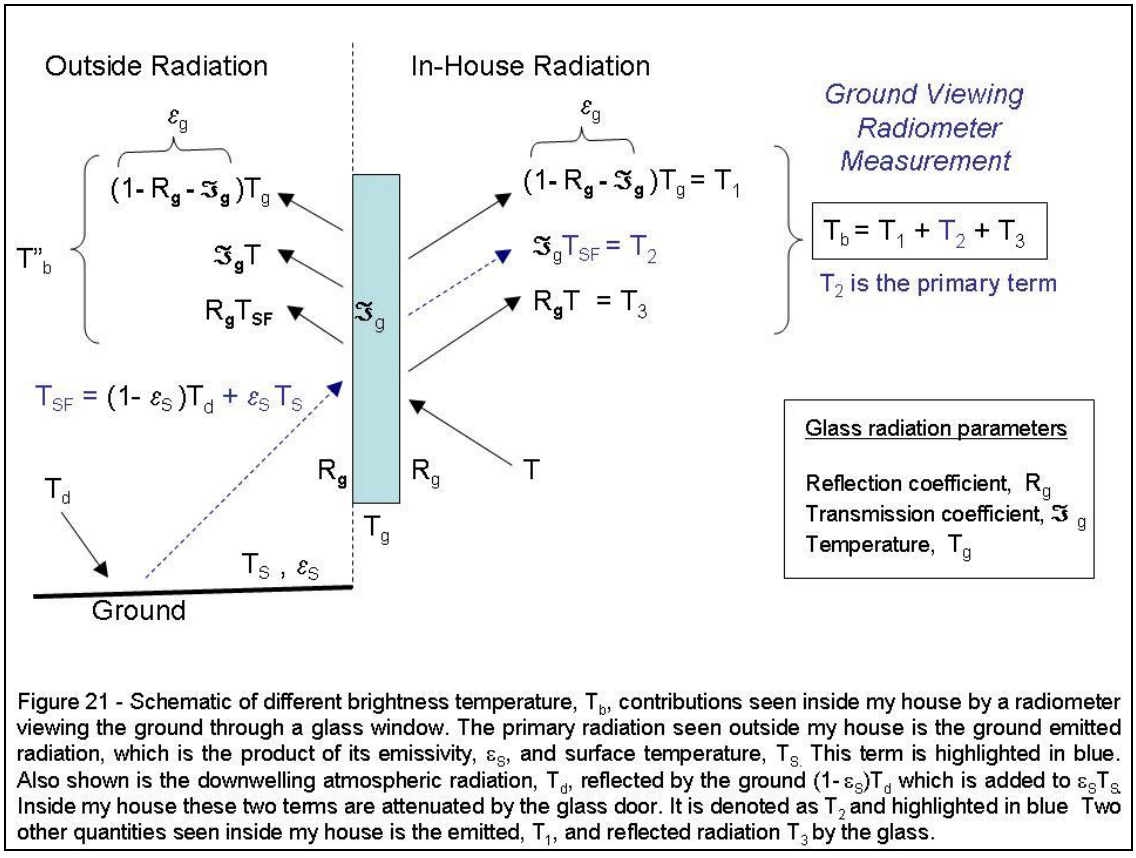

Figure 21 - Schematic of different brightness temperature, T_b, contributions seen inside my house by a radiometer viewing the ground through a glass window. The primary radiation seen outside my house is the ground emitted radiation, which is the product of its emissivity, ε_S, and surface temperature, T_S. This term is highlighted in blue. Also shown is the downwelling atmospheric radiation, T_d, reflected by the ground $(1- \varepsilon_S)T_d$ which is added to $\varepsilon_S T_S$. Inside my house these two terms are attenuated by the glass door. It is denoted as T_2 and highlighted in blue Two other quantities seen inside my house is the emitted, T_1, and reflected radiation T_3 by the glass.

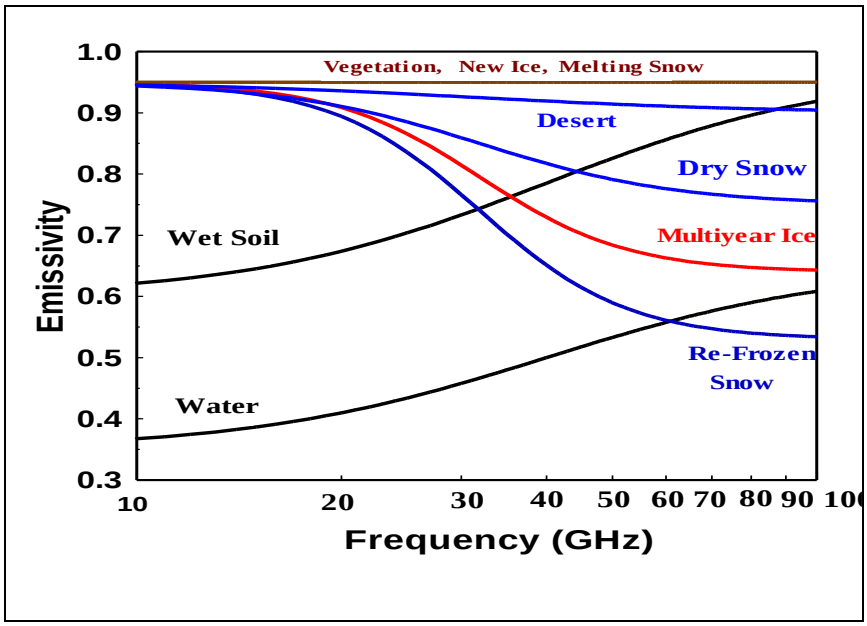

Figure 22- Emissivity obtained using the empirical function $\varepsilon_S = \left[\varepsilon_0 + \varepsilon_\infty (\nu/\nu_0)^n\right] / \left[1 + (\nu/\nu_0)^n\right]$ whose parameters $\varepsilon_0, \varepsilon_\infty, n, \nu_0$ are obtained from representative measurements at nadir viewing. Note that the highest emissivity is for vegetated land, new sea ice and melting snow while the lowest is for water and wet soil. Multiyear sea ice and re-frozen snow also has very low emissivity at high frequency, ν, with a negative slope. Surface identification is obtained from satellite radiometer measurements using the magnitude and slope of emissivity with frequency.

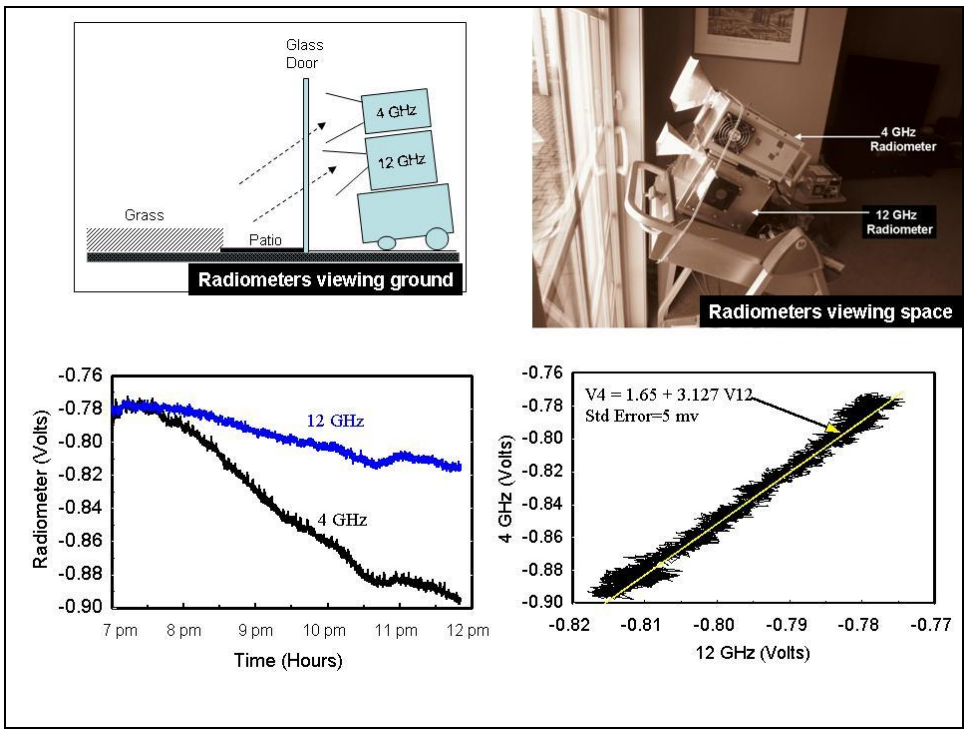

Figure 23 - The 4 and 12 GHz radiometers are placed on a movable cart to view the ground (Top Left) and sky (Top-right) from inside my basement. Radiometer voltages are plotted as function of time (bottom-left) when viewing the ground and a best linear equation is obtained (bottom-right) and shown in yellow.

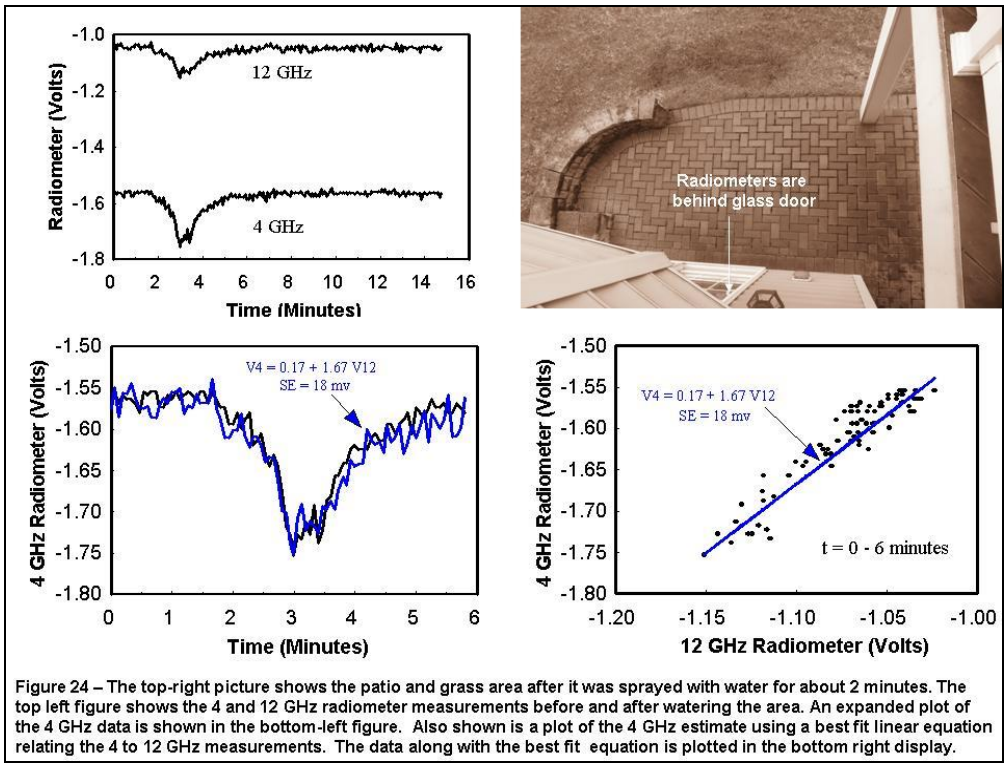

Figure 24 – The top-right picture shows the patio and grass area after it was sprayed with water for about 2 minutes. The top left figure shows the 4 and 12 GHz radiometer measurements before and after watering the area. An expanded plot of the 4 GHz data is shown in the bottom-left figure. Also shown is a plot of the 4 GHz estimate using a best fit linear equation relating the 4 to 12 GHz measurements. The data along with the best fit equation is plotted in the bottom right display.

7.2 Sky Viewing Rain Measurements

In this experiment the 4 and 12 GHz radiometers were elevated to view space as shown in the top-right picture in Figure 23. The different brightness temperature components are now depicted in Figure 25 where the combined terms result in an equation similar to the ground viewing equation (10a), *i.e.*,

$$T_b(\nu) = \Im_g\, T_d + \varepsilon_g\, T_g + R_g T \qquad (14a)$$

$$\text{where} \quad \varepsilon_g = 1 - R_g - \Im_g \qquad (14b)$$

$$\text{and} \quad T_d = (1 - \tau_{CLD}) T_{CLD} \ . \qquad (14c)$$

The first term on the right side is the downwelling atmospheric radiation, T_d, attenuated by the glass door. At the frequencies under consideration this emitted radiation is given by (14c) where τ_{CLD} is the liquid water transmittance due to clouds and rain absorption where T_{CLD} is its temperature. Neglected is the much smaller cosmic background and atmospheric emission terms (5) which can be added to (14c). All quantities in (14a, b, c) are frequency dependent except for the temperatures. The glass door contributions are also shown in Figure 25, where the glass absorption results in thermal emission $\varepsilon_g T_g$ with emissivity (14b). Also, included is the glass transmission coefficient, $\Im_g$, which attenuates the downwelling atmospheric emission. The last term on the right of (14a) is the reflection of in-house radiation at temperature T, where R_g is the glass reflection coefficient. The equation assumes no ground radiation is scattered into the antenna FOV when viewing the sky.

Using equations (14a), (14b) and (14c), and neglecting the glass absorption, $\varepsilon_g = 0$ and $R_g + \Im_g = 1$, so that

$$T_b(\nu) = (1 - R_g)\,(1 - \tau_{CLD})T_{CLD} + R_g T. \qquad (15)$$

Eliminating T_{CLD} we obtain the following relationship between the 12 GHz and 4 GHz brightness temperatures, *viz*.,

$$T_b(12) = S' T_b(4) + [R_g(12) - R_g(4)S']T \qquad (16a)$$

$$\text{where} \quad S' = \left[\frac{1 - R_g(12)}{1 - R_g(4)}\right] \frac{1 - \tau_{CLD}(12)}{1 - \tau_{CLD}(4)} \qquad (16b)$$

The slope *S'* given by (16b) is the product of two terms, one containing the glass reflection coefficients and the other containing the liquid water transmittances at the two frequencies. Note also that the above equations are similar to (13a) and (13b) which relates the 4 to 12 GHz ground viewing measurements.

From the insertion loss measured reflection coefficients in Appendix 9, and discussed in Section 7.1, the reflection coefficient term in (16b) is 0.45 so that the slope becomes

$$S' = 0.45\ \frac{1 - \tau_{CLD}(12)}{1 - \tau_{CLD}(4)}\,. \qquad (17)$$

At the frequencies of measurement the cloud and rain water droplets are smaller than the wavelength. The liquid water transmittance is then given by the Rayleigh approximation combined with Debye's dielectric model,

$$\tau_{CLD}(\nu) = e^{-Q/Q(\nu)}, \qquad (18a)$$

$$\text{with} \quad Q(\nu)^{-1} = \frac{0.0241\,\nu_0\,\nu^2}{\nu^2 + \nu_0^2}, \qquad (18b)$$

$$\text{where} \quad \nu_0 = 160\,e^{7.2[1 - 287/T_{CLD}]} \qquad (18c)$$

Equation (18a) contains the rain and cloud liquid water content, Q, and $Q(\nu)$ which is given by (18b). The quantity $Q(\nu)$ depends on frequency, ν, and the parameter ν_0, which is given by (18c) and is a function of the cloud temperature T_{CLD}. Table 3 below lists $Q(\nu)$ at three different cloud temperatures for the 4 and 12 GHz radiometers as well as the 20 GHz radiometer described in Chapter 8. The Table also lists the center frequencies measured for the 4, 12 and 20 GHz radiometers.

Table 3: Cloud Transmittance Parameter, $Q(\nu)$, at different Temperatures.

Radiometer	Center Frequency	T_{CLD} =270 K	T_{CLD} =275 K	T_{CLD} =280 K
4 GHz	3.9 GHz	$Q(\nu)$ = 278 mm	$Q(\nu)$ = 319 mm	$Q(\nu)$ = 365 mm
12 GHz	11.7 GHz	$Q(\nu)$ = 31.3 mm	$Q(\nu)$ = 35.8 mm	$Q(\nu)$ = 40.8 mm
20 GHz	20.5 GHz	$Q(\nu)$ = 10.5 mm	$Q(\nu)$ = 11.9 mm	$Q(\nu)$ = 13.5 mm

Since $\nu < \nu_0$, equation (18b) and Table 3 shows that $Q(\nu)^{-1}$ is nearly proportional to ν^2 with $Q(4)/Q(20) \cong 27.6$ and $Q(4)/Q(12) \cong 9.0$, which is almost independent of the cloud temperature. Also, for the small amount of liquid water associated with clouds and light rain $Q << 1$ mm so that $Q/Q(\nu) << 1$. As such, (18a) can be approximated as

$$\tau_{CLD}(\nu) \approx 1 - Q/Q(\nu), \qquad (19)$$

so that from (16a) and (17),

$$\frac{\Delta T_b(12)}{\Delta T_b(4)} \approx 0.45 \frac{Q(4)}{Q(12)} = 0.45 \left[\frac{11.7}{3.9}\right]^2 = 4.0 \ . \qquad (20)$$

The above relationship between the 12 and 4 GHz radiometer measurements is now examined using actual observations.

Figure 26 shows an example of the 4 and 12 GHz skyward measurements taken over an eight hour period on June 12, 2014, during which there was light and heavy rain. The two abrupt large voltage increases seen at 12 GHz between 5 pm and 7 pm is due to the thermal emission by rain. Smaller voltage increases are seen at 4 GHz due to the same rain event. Since non-precipitating clouds have smaller drop size and less water content than rain they produce a smaller increase at 12 GHz with no observable change at 4 GHz. As discussed later, since the liquid water transmittance given by (18a) decreases with frequency, the 20 GHz radiometer is even more sensitive to clouds and rain than the 12 GHz radiometer. Such a comparison between the 20 and 12 GHz measurements for clouds and rain is discussed in Chapter 8.

Before continuing I must digress and discuss what appears to be an apparent discrepancy. Prior to the rain events, Figure 26 shows a nearly constant 0.5 volt difference between the 12 and 4 GHz measurements. However, as shown in Appendix A9, the difference increases from 0.7 volts with the door open to 3.1 volts when the door is closed due to the glass door. In other words the 4 GHz measurements should be lower by about 3 volts during the rain-free period, not the 0.5 volts shown in Figure 26. The reason for this discrepancy is that the instrument cart shown in Figure 23 was moved slightly so that the larger 4 GHz antenna beamwidth picked up more stray radiation than the 12 GHz antenna. This approach of making the measurements initially close to each other by adding stray radiation could have also been achieved by adjusting the 4 GHz DC offset control. Incidentally, the use of stray radiation to reduce the offset was also apparently

done when initializing the measurements in Figure 23 while no such offset adjustment was done for the measurements in Figure 24.

Referring back to Figure 26, the bottom two plots show the 12 GHz measurements plotted against the 4 GHz measurements for the first rain event between 5 and 6 pm. For comparison, the bottom-right (plot #2) contains the time period when there was heavy rain present while the bottom-left (plot #1) is for the shorter period when the rain was much lighter. Regression analysis using the heavy rain data in plot #2 shows the 12 GHz measurements to be greater than at 4 GHz by a factor of 12.4. This factor is reduced to 8.6 when using only the light rain data in plot #1. Interestingly, measurements described in Appendix A10 of another severe storm on February 24, 2016 resulted in nearly the same ratio of 12.4 between the two radiometer measurements for intense rain. However, in general the measurements of other rain events were found to have ratios between 10 and 15. The reason for the variation in the ratio is explained next.

The slopes shown in Figure 26 can be compared directly with that given by equation (20) since T_b is linearly related to voltage. As such, the T_b ratio of 4.0 in (20) is about 3 times smaller than the 12.4 value measured for heavy rain while it is about 2 times smaller than the 8.6 value obtained for the light rain. Much of this difference in the T_b ratio can be attributed to the larger spatial averaging of rain by the 4 GHz antenna beamwidth of 27 degrees compared with the 12 GHz beamwidth of 16 degrees. Furthermore, as shown below, this factor when combined with equation (20) results in a ratio comparable to the measurements.

For the maximum spatial averaging effect we consider a small isolated opaque rain feature within the antenna beamwidth, so that the 12 to 4 GHz brightness temperature ratio is proportional to the ratio of viewing areas, *i.e.*, $(27^0/16^0)^2$ =2.8. When this spatial averaging factor is multiplied to equation (20), the resulting ratio becomes 11.2, which is comparable to the 12.4 value obtained for the heavy rain measurements. For more widespread rain the spatial averaging effect results in a factor less than 2.8 so that the ratio would be less than 11.2, as found for the light rain measurements. In summary, the variation due to spatial averaging when combined with the glass reflectance contribution (20) can result in T_b ratios comparable to the measurements. While these calculations are encouraging, what is more significant is the fact that the 12 GHz radiometer detects rain in a manner similar to radar, but instead of measuring the scattering it measures the absorption by rain drops.

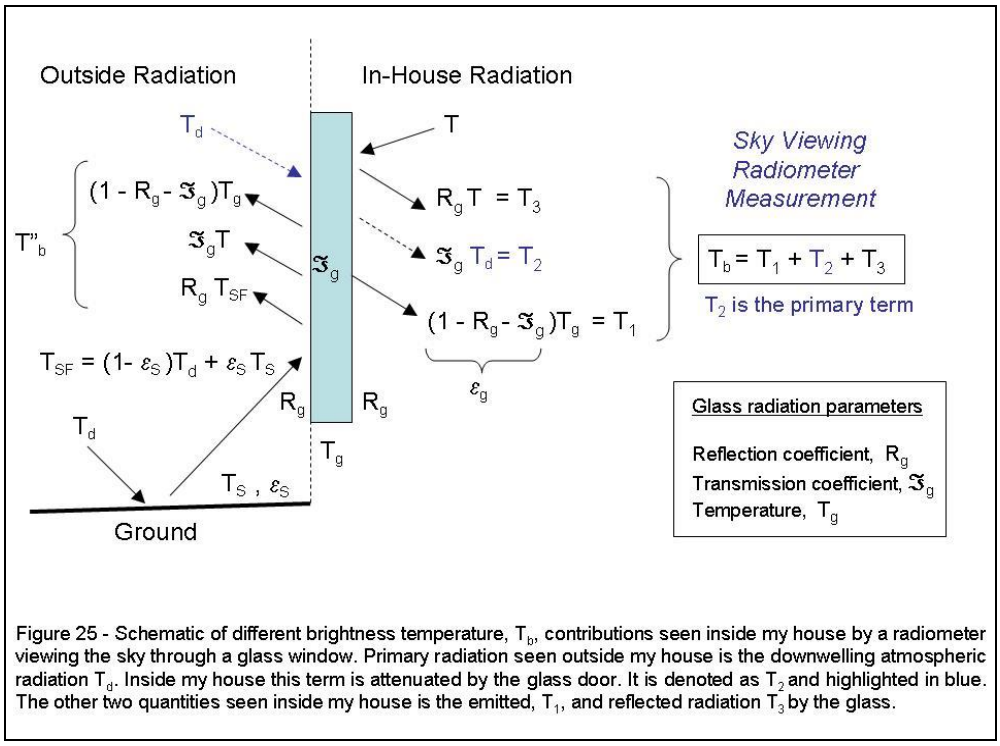

Figure 25 - Schematic of different brightness temperature, T_b, contributions seen inside my house by a radiometer viewing the sky through a glass window. Primary radiation seen outside my house is the downwelling atmospheric radiation T_d. Inside my house this term is attenuated by the glass door. It is denoted as T_2 and highlighted in blue. The other two quantities seen inside my house is the emitted, T_1, and reflected radiation T_3 by the glass.

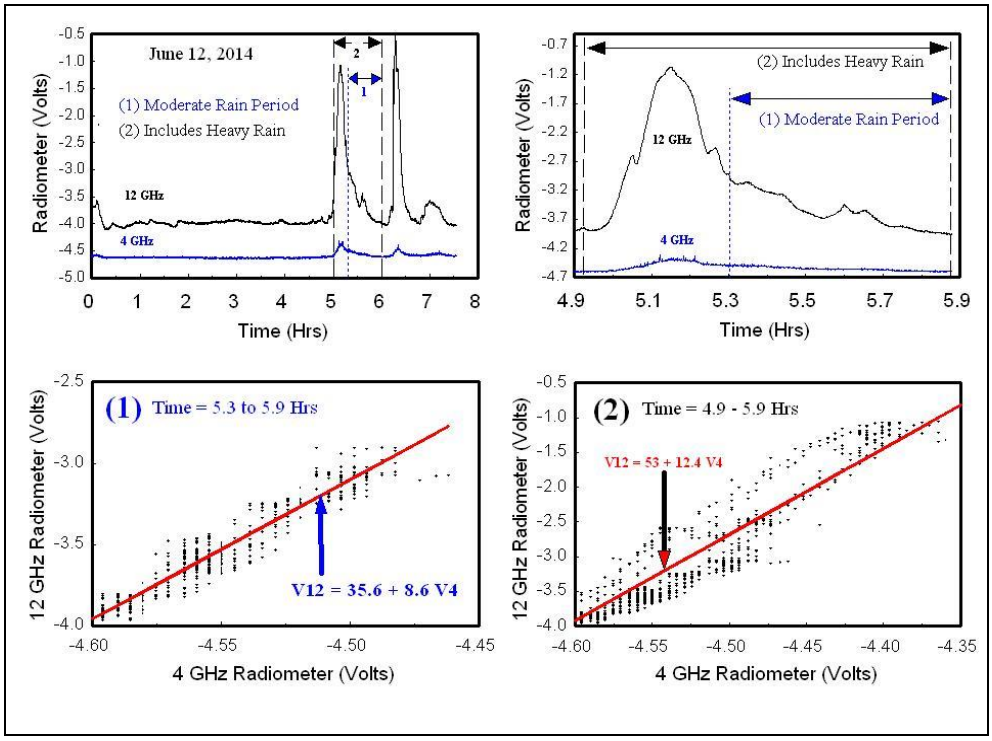

Figure 26- The top left plots the 4 and 12 GHz measurements over an 8 hour period beginning at 12pm on June 12. Two distinct rain events are seen between 5 and 7 pm, with the 12 GHz radiometer increasing from -4 volts to less than -1 volt while the 4 GHz radiometer increases by only 0.2 volts. The top right plots the first rain event between 4.9 to 5.9 hours. During this time the bottom right shows the 12 GHz voltage increasing by a factor of 12.4 compared to 4 GHz. However, the bottom left shows the 12 GHz voltage only increases by a factor of 8.6 for the period containing widespread light rain between 5.3 and 5.9 hrs.

8. 20 GHz Radiometer

This last Chapter describes my highest frequency Dicke radiometer together with some measurements, analysis and simulations. The radiometer is built using the Norsat 9000C Ka band LNB shown in Figure 5 which amplifies frequencies between 20.2 and 21.2 GHz at linear polarization. Its higher frequency makes the radiometer more sensitive to atmospheric absorption by clouds and rain than the two lower frequency radiometers. Figure 13 also shows it to be more sensitive to water vapor than the lower frequency radiometers. Furthermore, as explained next, the radiometers center frequency is at 20.5 GHz although it will be referred to as a 20 GHz radiometer.

8.1 Radiometer Construction

The Norsat LNB has an *LO* frequency of 19.25 GHz with a down converted *IF* frequency between 0.95 to 1.95 GHz. As such, the corresponding *RF* frequency is between 20.2 and 21.2 GHz. As with the lower frequency LNB's shown in Figure 6 it has waveguide input and coax output at the *IF* port. The LNB also has 55 dB of gain with a noise figure of 1.3 dB or 100 *K* noise temperature. This is 7 times greater than the 4 and 12 GHz LNB noise temperatures of 14 *K*. The radiometer noise (NEΔT) is therefore proportionally larger. Also, due to its higher frequency, it is more expensive to construct than the lower frequency radiometers; *i.e.,* primarily due to the LNB. The radiometer also requires higher precision components such as the pin diode switch, isolator and waveguide adapters which are more difficult to acquire at low cost.

While the Norsat Ka-Band LNB is more expensive than the C- and Ku- band units, which cost about $10, I was able to find one on Ebay at $50. Figure 27 shows the radiometer lid opened to display the LNB along with the other components. The block diagram is similar to the 12 GHz radiometer in Figure 3. Clear sky measurements described in Section 4.2 are used to set the radiometer parameters (G_1=1000, G_d=10 and G_2=3.2) so that the output is within the 0 to -9 volt range. Tipping curve measurements described in Section 8.3 are then used to obtain the calibration equation. As such, the total radiometer gain is 145 dB which is larger than the 12 GHz radiometer gain of 130 dB and less than the 4 GHz radiometer gain of 158 dB. Also, its smaller size antenna has 20 dB gain, which is similar to the 12 GHz antenna gain of 19 dB. Measurements using all three radiometers are obtained by mounting the 20 GHz radiometer as shown in Figure 28.

Waveguide adapters and an isolator were readily available for the 18 to 22 GHz Ka frequency band, although I was unable to find a pin diode switch on Ebay at frequencies much beyond 18 GHz. I therefore decided to use the same General Microwave (M862B) switch used for the lower frequency radiometers. This pin diode switch is specified to operate between 0.1 and 18 GHz with 2 dB insertion loss and 45dB isolation at its highest frequency. Fortunately, as shown in Figure 31, I measured little degradation of these parameters between 18 and 20.8 GHz. At these higher frequencies Figure 30 shows about a 3 dB insertion loss when the pin diodes are switched on and generally more than 45 dB isolation when the pin diodes are powered off. However, beyond 20.8 GHz the insertion loss sharply increases to 12 dB at 21.5 GHz. Interestingly, as discussed next the radiometers peak response is at 20.5 GHz due to the high detector sensitivity and low insertion loss of the pin diode switch at this frequency.

The radiometers frequency response is shown in Figure 29 next to that of the detector. These radiometer measurements were obtained using a sweep generator whose attenuated output of -87 dBm is directly connected to the pin diode switch input. The sweep generator frequency was varied between 20.15 to 21.15 GHz and the normalized radiometer output voltage is plotted in dB as a function of *IF* frequency (0.9 to 1.9 GHz). Unlike the LNB which covers a 1 GHz bandwidth from 20.2 to 21.2 GHz, the radiometer output peaks at 20.5 GHz with a 250 MHz bandwidth. As explained next, this narrow bandwidth centered at 20.5 GHz occurs primarily due to the detector.

In a separate experiment the detector was excited using another sweep generator having an attenuated output of -25 dBm over the *IF* frequency range. As with the radiometer, the normalized detector output voltage in dB is plotted in Figure 29 as a function of *IF* frequency. The circuit is shown in the Figure with its amplifier gain set to 10 and peak response at 1.26 GHz. It is found to have a square law response with a sensitivity of 18.6 mv/μw for input power less than 20 μw or output voltage less than 370 mv. Note how the radiometer follows the detector's response whose output also peaks at a 1.26 GHz (20.5 GHz *RF* frequency) with a 230 MHz bandwidth. Stated differently, the radiometer response is mainly due to the detector which inadvertently acts to narrow the bandwidth beyond that of the LNB. Also, as mentioned above, the increased insertion loss by the pin diode switch beyond 20.8 GHz also contributes to the radiometer response.

Unfortunately, this Ka band radiometer detects *RFI* at certain times of the day when viewing space. Unlike the occasional noise spikes observed for the 4 GHz radiometer, Figure 30 shows the 20 GHz interference to be stepwise jumps of varying duration beginning at 9 pm on May 12, 2017. Compared to the 12 GHz measurements, the 20 GHz radiometer displays abrupt offsets of 0.1 to 0.3 volts that persist throughout the evening until the next day at about 12 pm. Other observations show the *RFI* begins at later times. As shown in the next Section, the interference only occurs when viewing space so I originally felt it was due to TV broadcast from geostationary satellites. However, the radiometer antenna is not directed toward Directv geostationary satellites and the *RFI* only occurs at certain times of the day. Also, the interference pattern is not observed for the other radiometers whose LNB's operate within the C and Ku broadcast band. As such the interference may be due to non-stationary low orbiting satellites. It may also be localized to my particular area. I should also mention that I tried unsuccessfully to reduce the interference using low and high pass filters at the *IF* output. I also tried to identify the *RFI* frequencies using spectrum analyzer measurements of the *IF* output but only detected weak signals outside the LNB passband that did not coincide with the interference pattern.

After constructing this 20.5 GHz radiometer, I found that the FCC allocates a protective band between 21.2 to 21.4 GHz for radio astronomy and space research although it excludes fixed and mobile services. I therefore constructed a 2nd radiometer using another LNB, but who's *LO* was shifted from 19.25 GHz to a maximum of 19.93 GHz by reducing its DRO size and tuning it. This 680 MHz increase of the *LO* increased the radiometer *RF* frequency to the edge of the protective band at 21.2 GHz, as defined by the detector's peak response at 1.26 GHz. However, as shown in Figure 31 the pin diode switch has 8 dB insertion loss at 21.2 GHz. This required a doubling of the detector amplifier gain from 10 to 20. The larger insertion loss of the switch also increased the radiometer noise (NEΔT) so a 5 second integration time was needed compared to 1 second for the 20.5 GHz radiometer. However, after all of this modification I only

observed a small reduction in interference compared with the 20.5 GHz radiometer so I felt it was not worth the extra effort.

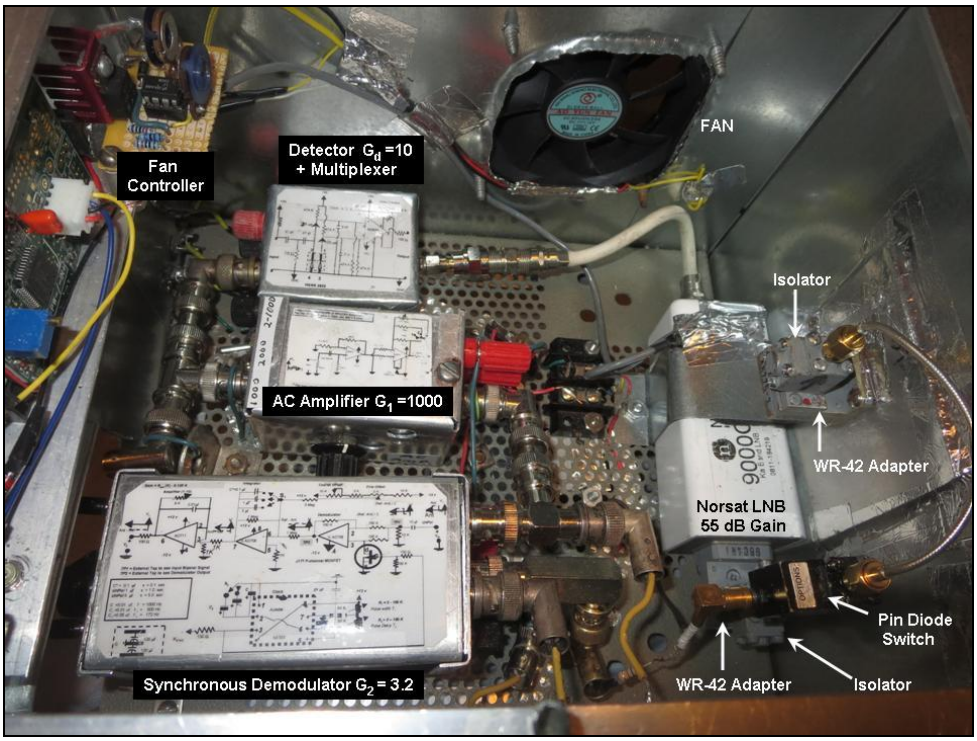

Figure 27- The top lid of the 20 GHz radiometer shown in Figure 28 is opened to show the components. Except for the Norsat LNB, the components are similar to the 12 GHz radiometer in Figure A3. The layout of components and wiring is cleaner looking than the 12 GHz radiometer.

Figure 28- The 20 GHz radiometer is mounted on top of the 4 and 12 GHz radiometers. The 20 GHz radiometer has the smallest antenna with 20 dB gain. In comparison, the 12 GHz antenna has 19 dB gain while the largest antenna at 4 GHz has the smallest gain of 15 dB.

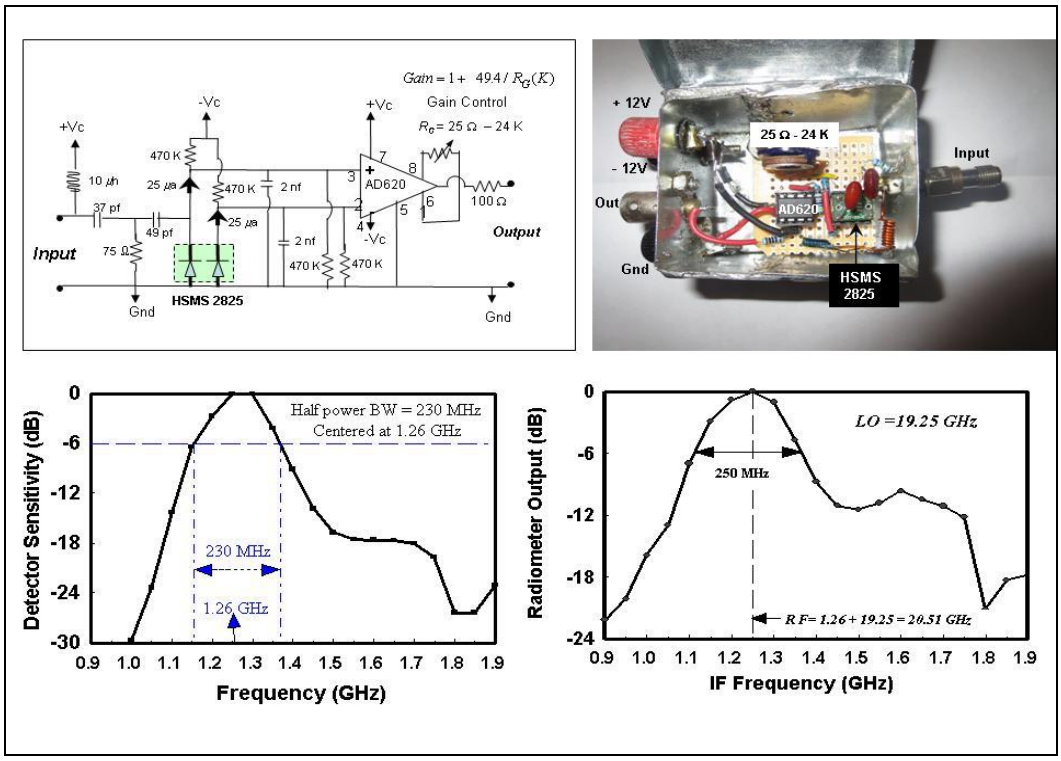

Figure 29- The 20 GHz radiometer uses a temperature compensated detector (top-right) similar to the other radiometers. Its circuit (top-left) uses an AD620 difference amplifier with its gain set to 10 by setting R_G to 5.5 *K*. Its input uses a multiplexer circuit to power the LNB while passing the *IF* signal to the detector. The normalized detector sensitivity (bottom-left) peaks at 1.26 GHz with a 230 MHz bandwidth, while the normalized radiometer response (bottom-right) peaks at 19.25 GHz (*LO*) + 1.26 GHz (*IF*) = 20.51 GHz with a 250 MHz.

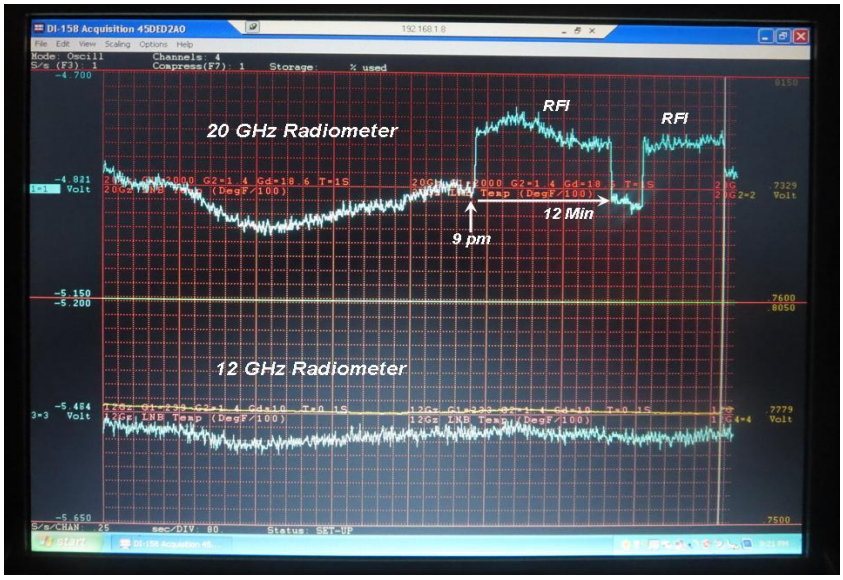

Figure 30- Radiometer measurements at 20 GHz and 12 GHz on May 12, 2017 of cloudy skies. Measurements were taken a few minutes prior to and after 9 pm when abrupt jumps lasting 12 minutes occur due to *RFI*. Integration times for the 20 and 12 GHz radiometer is 1.0 and 0.1 seconds respectively. Radiometer output voltages are shown using the same vertical range of 0.45 volts and horizontal (time) scale which cover a 53 minute period.

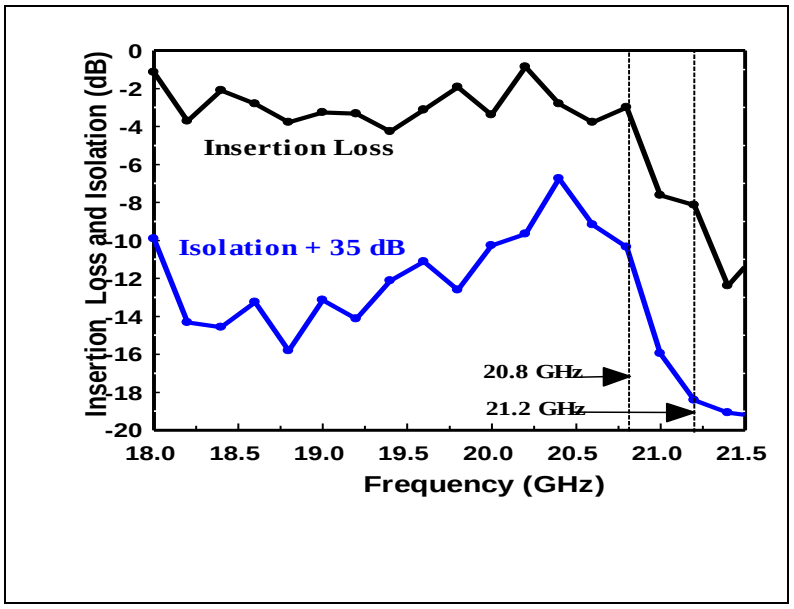

Figure 31- General Microwave pin diode switch (M862B) measurements of insertion loss and isolation at frequencies beyond 18 GHz. It is specified to operate between 0.1 and 18 GHz with -2 dB insertion loss and -45 dB isolation. Measurements show little degradation between 18 and 20.8 GHz. However, beyond 20.8 GHz its insertion loss decreases (*i.e.*, -8 dB at 21.2 GHz).

8.2 Cloud and Rain Measurements

Sky viewing cloud measurement

In the absence of interference the 20 GHz radiometer provides high quality atmospheric measurements when viewing space. As an example, Figure 32 shows the 20 GHz and 12 GHz radiometer measurements of clouds seen through the glass patio door on May 12, 2017 between 12 am and 9 pm (Top-left). During this 9 hour period no *RFI* is seen except for its onset at 9 pm. The top-right picture taken at about 4 pm shows a large cumulous cloud while the bottom-left is a plot of the 20 GHz against 12 GHz cloud measurements between the hours of 4.1 to 4.6. During this half hour period the radiometers view varying amounts of cloud liquid water within the FOV. The slope of the measurements $\Delta T_b(20)/\Delta T_b(12)$ is shown to be 2.0 in Figure 32 (Bot-Left). According to equations (16a, b) this slope depends on the cloud transmittance and glass reflectivity at the two frequencies, *i.e.*,

$$\frac{\Delta T_b(20)}{\Delta T_b(12)} = \left[\frac{1-R_g(20)}{1-R_g(12)}\right]\frac{1-\tau_{CLD}(20)}{1-\tau_{CLD}(12)} \approx \left[\frac{1-R_g(20)}{1-R_g(12)}\right]\frac{Q(12)}{Q(20)} \qquad (21)$$

Since the cloud absorption parameter, $Q(\nu)$, varies approximately as $1/\nu^2$, the term containing cloud transmittance is 2.9 for the two frequencies. Therefore, upon dividing 2.0 by 2.9, the factor in brackets containing the glass reflectivity is 0.69. This reflectivity term is larger than the 0.45 value determined from the 12 and 4 GHz insertion loss measurements described in Appendix A9.

Ground viewing (indirect) rain measurement

As shown in Figures 30 and 32, *RFI* is observed to start at 9:30 PM on May 12 when viewing space. To help identify the direction of *RFI* the radiometer cart is adjusted so the antenna views the ground rather than space. However, while no interference is seen when viewing the ground, I measured a small increase of 0.168 volts for the 20 GHz measurements at 10:20 PM along with a smaller increase of 0.084 volts at 12 GHz. Both voltage increases were found to occur during a brief light rain event. The measurements are shown in Figure 33 and analyzed below.

The increased measurements shown in Figure 33 at 20 and 12 GHz is probably due to the downwelling radiation by rain, T_d. As illustrated in Figure 21, this radiation is reflected by the ground in the direction of the radiometer antenna. The Figure also shows all other contributions seen when viewing the ground through my glass patio door. The combined components are given by equation (11). Using this equation together with (14c) the brightness temperature can be written as

$$T_b(\nu) = [(1-R_g)\,\varepsilon_S T_S + R_g T] + \Delta T_b \qquad (22a)$$

$$\text{where} \quad \Delta T_b = (1-R_g)(1-\varepsilon_S)\,(1-\tau_{CLD})\,T_{\text{CLD}} \ . \qquad (22b)$$

The dominant term in (22a) is the bracketed term which contains the surface emitted radiation $\varepsilon_S T_S$. The smaller residual term ΔT_b is the downwelling atmospheric radiation reflected by the ground as given by (22b). Both terms in (22a) also include the contributions due to the glass reflectance, R_g. The ground reflected atmospheric radiation ΔT_b is considered responsible for the small perturbations seen in Figure 33. It increases the brightness temperature due to the transmittance by rain and clouds as given by (18a). However, as shown in Figure 22 the emissivity over vegetated land is about 0.95 so that the ground reflectivity 1-ε_S in (22b) is small. Therefore, to obtain a significant brightness temperature increase the transmittance must be small. Such small transmittance occurs predominately due to the large amounts of liquid water associated with rain clouds.

To further analyze the measurements in Figure 33, equation (22b) is used to obtain the brightness temperature ratio at the two frequencies, *viz*.,

$$\frac{\Delta T_b(20)}{\Delta T_b(12)} = \left[\frac{1-R_g(20)}{1-R_g(12)}\right]\left[\frac{1-\varepsilon_S(20)}{1-\varepsilon_S(12)}\right]\left[\frac{1-\tau_{CLD}(20)}{1-\tau_{CLD}(12)}\right] \qquad (23)$$

Neglecting the small emissivity difference at the two frequencies the brightness temperature ratio is the same as equation (21). As such, the brightness temperature ratio when viewing the ground should be the same value of 2.0 as found when viewing cloudy skies. In fact, when applying the voltage increases shown in Figure 33 we obtain $\Delta T_b(20)/\Delta T_b(12) = 0.168/0.084 = 2.0$, which is indeed the same value obtained previously when viewing clouds.

To observe larger downwelling radiation, a second ground viewing experiment was taken on May 5, 2017 when heavier rain occurred. Figure 34 (Top) shows the time series over a

nine hour period starting at 12 AM. For more detail, the bottom Figure shows an expanded plot around 8 AM during the heavy rain period. As in Figure 33, the radiometers measure abrupt increases due to the rain emitted radiation reflected by the ground toward the radiometers. However the voltage increase is now much larger than before. Furthermore, the 20 GHz measurement approaches saturation while the 12 GHz increase of 0.55 volts approaches the 20 GHz increase of 0.65 volts.

This indirect observation of rain by way of ground reflection is a demonstration of the high radiometric sensitivity to detect very small signals. A much larger signal is obtained using direct (skyward) observations. Instead of (22b) the brightness temperature increase due to rain is given by (15), *i.e.*, $\Delta T_b = (1-R_g)(1-\tau_{CLD})\,T_{\mathrm{CLD}}$. The absence of the reflectivity term (1-ε_S) in (15) results in a 3.3 fold increase in ΔT_b compared to (22b) assuming a very wet soil emissivity of 0.7 due to rain (see Figure 22). However, for non flooded land the emissivity is 0.95, which results in a 20 fold reduction in ΔT_b compared with the direct viewing measurement. Compared to the indirect result, the much larger direct measurement of rain is due to the large contrast between cold space and the rain emitted radiation. In an analogous situation, satellite radiometers operating below 20 GHz rarely detect rain over land due to the very small difference between the land and rain emitted radiation. However, these same lower frequency radiometers readily detect both rain and clouds over oceans since the sea surface emissivity is about 0.45 so a large contrast exists between the ocean and atmospheric emission. Furthermore, as denoted in Figure 43, high frequency satellite radiometers (*e.g.*, 85 GHz) detect rain over land and ocean by measuring the decrease in upwelling radiation due to scattering by millimeter size ice particles formed in rain clouds as part of the precipitation process.

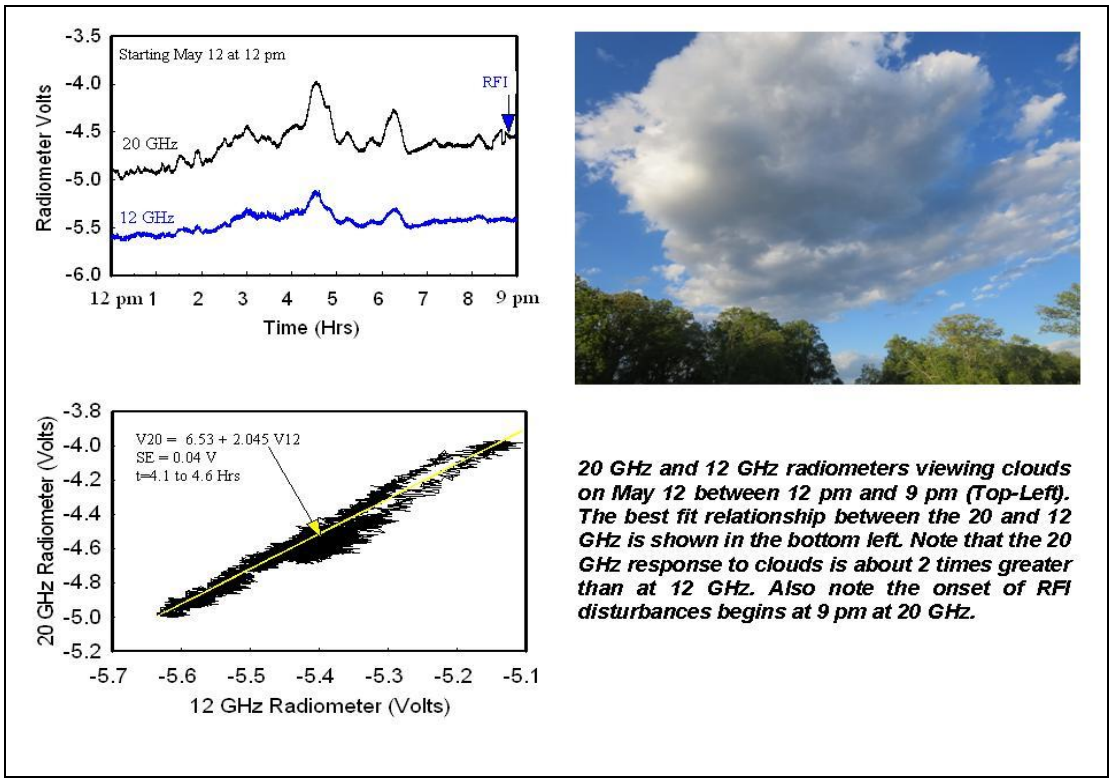

Figure 32- Clouds measured using the 20 and 12 GHz radiometer on May 12, 2017 between 12 and 9 pm (Top-left). The cloud picture on the top-right is at 4 pm, while the bottom-left plots the 20 GHz against 12 GHz measurements between 4.1 to 4.6 hours. The measurement ratio of 2.0 is the product of the cloud transmittance and glass reflectivity factors as given by equation (16b).

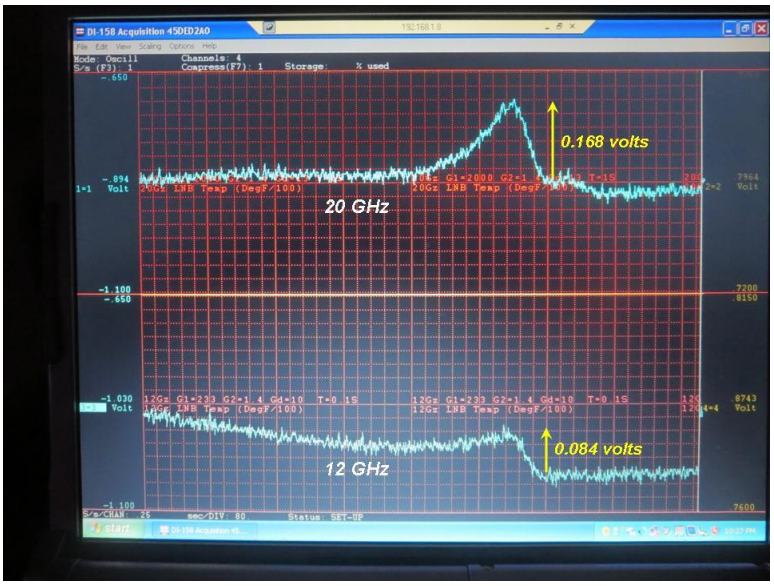

Figure 33- Surface viewing rain measurements on May 2, 2017 at 10:20 PM using the 20 and 12 GHz radiometers. Radiometer output is plotted on a vertical scale having a 0.45 voltage range. The horizontal time scale covers a 53 minute period. Integration time is 1 second for the 20 GHz radiometer and 0.1 seconds for the 12 GHz radiometer. The measurement increase of 0.168 volts at 20 GHz and 0.084 volts at 12 GHz results from rain emitted radiation reflected by the ground and received by the radiometers. This measurement ratio of 2.0 is the product of the cloud transmittance and glass reflectivity factors at the two frequencies given by equation (23).

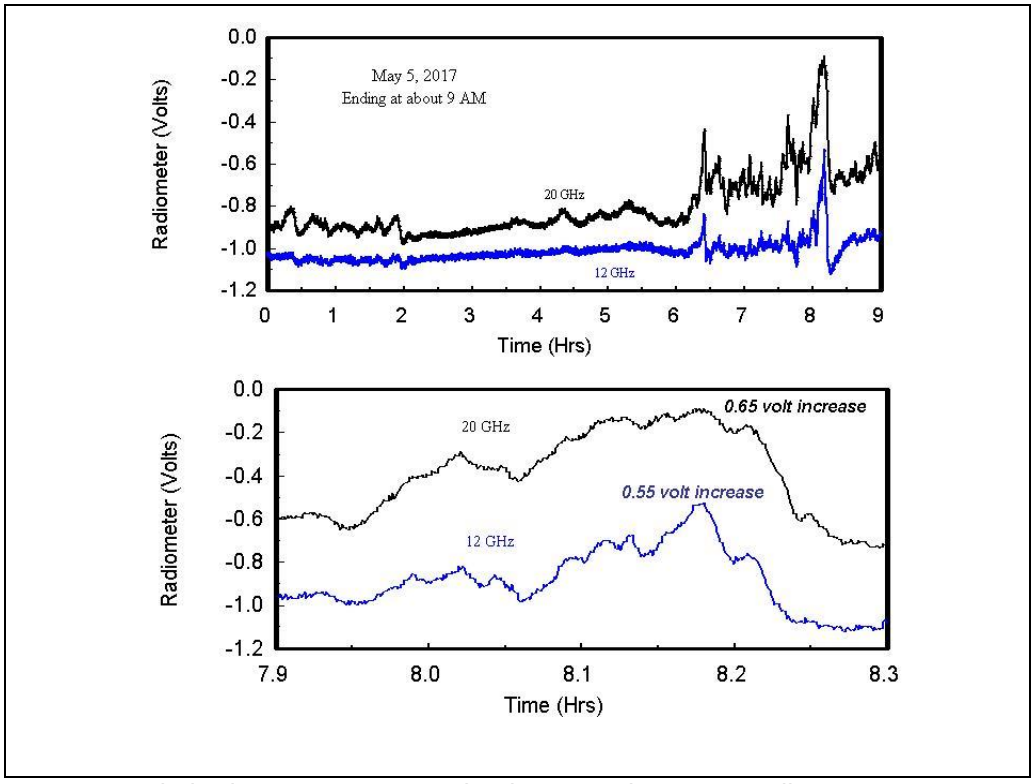

Figure 34- Ground viewing measurements by the 20 and 12 GHz radiometers on May 5, 2017 over a 9 hour period starting at 12 AM. The top plot displays the total time period while the bottom is an expanded plot during the most intense rain period around 8 AM. As in Figure 33, the integration time is 1 sec for the 20 GHz radiometer and 0.1 sec for the 12 GHz radiometer. The ratio of the 20 to 12 GHz measurements during this intense rain period is 1.3. This ratio is less than the 2.0 value found for light rain in Figure 33 due to saturation of the 20 GHz measurements.

8.3 Tipping Curve Calibration

Clear sky radiometer measurements were made from the upper patio deck on July 9, 2018 at about 2 PM when the surface temperature was 92 ^{0}F and relative humidity was 37 %. Unlike the zenith viewing sky measurements at 4 and 12 GHz described in Chapter 4, the 20 GHz radiometer views the sky at zenith angles, θ, from 0^0 to +/- 90^0 using the flat copper reflector shown in Figure 35. Also, as illustrated in Figure A11, the polarization direction is kept constant as the reflector is rotated. Unfortunately, as shown later, a nonlinear increase in radiometer voltage as a function of Secθ is found due to blockage of sky radiation and the resulting thermal emission by trees and houses. The blockage on one side of zenith (0^0 to 90^0) is due to my house, while the blockage on the other side (0^0 to -90^0) is less and primarily due to trees seen in the distance at low elevation or large zenith angles. Therefore, to obtain the best views of space the reflector was scanned at zenith angles between 0^0 and -70^0 in 10^0 steps so that Secθ varies between 1.0 and 2.9. Figure 36 plots the radiometer voltage as a function of Secθ, where for consistency the eight angle measurements were repeated four times. The following is the data analysis.

Considering a linear response, the calibrated brightness temperature is given by (3), *i.e.*,

$$T_b = \mathrm{I} + \mathrm{S}\,\mathrm{V}, \qquad (24)$$

where I is the offset, S is the radiometric gain and V is the output voltage. As shown in Figure 36, the best straight line fit of the measurements is

$$\mathrm{V} = -8.38 + 1.26\ \mathrm{Sec}\theta \qquad (25)$$

so that upon substituting (25) into (24) the brightness temperature is

$$T_b = (\mathrm{I} - 8.38\mathrm{S}) + 1.26\ \mathrm{S}\cdot\mathrm{Sec}\theta. \qquad (26)$$

As discussed in Section 4.1, the sky brightness temperature is

$$T_b = \tau^{Sec\theta}\, T_{CB} + (1 - \tau^{Sec\theta})\, T_M \qquad (27)$$

so that for $Sec\theta = 0$ equation (27) results in $T_b = T_{CB} = 2.7\,K$. Therefore, setting $Sec\theta = 0$ in (26) we can write[2],

$$T_{CB} = \mathrm{I} - 8.38\mathrm{S}. \qquad (28)$$

Also, when viewing the high emissivity warm target at temperature T_W = 307 *K* (92 ^{0}F), the radiometer voltage is 94 mv so that from (24),

[2] If the calibration parameters *I* and *S* are known *a-priori* then (27) can be used to derive T_{CB}. This approach was in fact used by Dicke, and later by Penzias and Wilson, to accurately measure T_{CB}. Conversely, as done here, (27) can be used to calibrate the radiometer since T_{CB} is now known with very high accuracy.

$$T_W = \mathrm{I} + 0.094\mathrm{S}. \qquad (29)$$

Subtracting equation (29) from (28) the radiometric gain is,

$$\mathrm{S} = \frac{T_{\mathrm{W}} - T_{\mathrm{CB}}}{8.38 + 0.094} = 35.91 \ \ K/\mathrm{Volt}, \qquad (30)$$

and from equation (29) the offset is

$$\mathrm{I} = T_{\mathrm{W}} - 0.094\mathrm{S} = 303.62 \ \ K. \qquad (31)$$

Substituting (30) and (31) into (24), the calibration equation becomes

$$\boxed{T_b = 303.62 + 35.91 \ \mathrm{V}} \qquad (32)$$

and the calibrated tipping curve (26) becomes

$$\boxed{T_b = 2.7 + 45.175 \cdot \mathrm{Sec}\theta} \ . \qquad (33)$$

It should be noted that the radiometric gain of 35.91 in (32) depends on the extrapolated cosmic background measurement of -8.38 volts which is obtained by setting $Sec\theta = 0$ in (25). Also, as discussed next the atmospheric opacity depends on the tipping curve slope of 1.26 in (25).

As explained in Appendix A-11, the atmospheric opacity can be obtained using A11-9,

$$\alpha = -\frac{\mathrm{d}\ln\left[T_{\mathrm{M}} - T_{\mathrm{b}}(\theta)\right]}{\mathrm{d}\,\mathrm{Sec}\theta} \quad \text{with} \quad T_{\mathrm{M}} = 285 \ K, \qquad (34)$$

with $T_b(\theta)$ obtained by applying the calibration equation (32) to the voltage measurements of Figure 36. The natural logarithm term is then plotted against $Sec\theta$ in Figure 37 to obtain the best fit straight line,

$$\ln\left[T_M - T_b(\theta)\right] = 5.71 - 0.229\,Sec\theta \ . \qquad (35)$$

Applying (35) to (34) the opacity becomes 0.229 nepers and the transmittance is

$$\tau = e^{-0.229} = 0.80. \qquad (36)$$

Alternatively, the opacity can be obtained using equation A11-4 in Appendix A11,

$$\alpha = \ln\left[\frac{T_M - T_b(0^0)}{T_M - T_b(60^0)}\right], \qquad (37)$$

where from (33), $T_b(0^0) = 45.87\ K$ and $T_b(60^0) = 93.75\ K$ so that $\alpha = 0.223$. This simpler method results in nearly the same opacity as the 0.229 value obtained using (34) and (35).

The cloud-free atmospheric transmittance is the product of the oxygen and water vapor components,

$$\tau = \tau_{O2}\tau_{H2O} = e^{-\alpha_{O2}(\nu)}e^{-TPW/W(\nu)} \quad , \qquad (38)$$

where the water vapor opacity is proportional to *TPW* so that its transmittance can be parameterized using the frequency dependent quantity $W(\nu)$. At ν = 20.5 GHz the calculated values of α_{O2} and W are listed in Table 4 as 0.014 and 270 mm, respectively. Therefore, from (38), $TPW = -W\,[\ln\tau + \alpha_{O2}]$ = 58 mm for τ = 0.80. However this *TPW* value appears two large. A more realistic transmittance at 20.5 GHz would be greater than 0.85 so that *TPW* is less than 38 mm.

The large opacity of 0.229 results from the slope of 1.26 seen in Figure 36. This large slope is likely due to blockage of the sky radiation by objects such as trees. Furthermore, the thermally emitted radiation by trees can be leaked into the feed horn as the reflector rotates to large zenith angles. Such leakage or spillover at large viewing angles produce large sidelobes in the antenna pattern. As discussed next, one way to reduce the angular variation of the antenna pattern is to use a conical scanning reflector. Better yet, any antenna pattern variation due to the reflector can be eliminated by mounting the radiometer on a tripod as described below.

To minimize the antenna pattern variation with scan angle, radiometers use a circularly polarized feed horn with the reflector rotated in azimuth about the feed horn axis[3]. As such, the antenna pattern remains almost unchanged as the reflector is rotated in azimuth. However, since my feed horn is linearly polarized, the measured brightness temperature varies with azimuth angle, ϕ, according to $T_b = T_V \cos^2\phi + T_H \sin^2\phi$, where T_V and T_H are the vertical and horizontal polarized components, respectively. Fortunately, the sky radiation (27) is un-polarized so $T_b = T_V = T_H = \tau^{Sec\phi}T_{CB} + (1-\tau^{Sec\phi})T_M$ where the zenith angle in replaced by the azimuth angle. Alternatively, rather than use a reflector to view the sky, the radiometer can be scanned in elevation and azimuth by mounting it on a tripod. As shown in the Preface of this document as well as in Figure 38, this approach was used by Dicke in 1946 to measure atmospheric absorption and will be used here.

Figure 39 shows the 20 GHz radiometer mounted on a tripod whose elevation can be varied from 0^0 to 60^0 so that the zenith angle varies from 90^0 to 30^0, respectively. However, while no problem occurs when viewing the sky at high elevation, various objects can obscure the sky at low elevation. The area outside my patio is surrounded by trees. Also, for privacy, a plastic lattice panel exists between my house and my neighbors. Since this panel produces blockage, the tripod is raised on a patio table to elevate it as shown in Figure 38. The best orientation to view space is determined by moving the tripod and scanning it in elevation and azimuth to find the location with the lowest voltage. Using this procedure, Figure 39 shows the best sky view at low elevation while Figure 40 shows the cloud free measurements obtained at this location on August 26 when the surface temperature was 89^0 F.

[3]A Steerable Dual-Channel Microwave Radiometer for Measurements of Water Vapor and Liquid in the Troposphere, Journal of Climate and Applied Meteorology, Vol. 22, May 1983, pp 789-806.

The left plot in Figure 40 displays the full range of radiometer measurements as a function of Secθ for zenith angles between 35^0 and 80^0. Note that the voltage increases linearly for $\theta < 70^0$, after which the response becomes nonlinear for larger angles. This nonlinear behavior is due to blockage of the sky radiation by trees in addition to its thermal emission. Such effects for $\theta > 70^0$ is also displayed by comparing the best fit quadratic equation with the linear equation obtained for $\theta < 70^0$ or Sec $\theta < 3$, i.e.,

$$V = -8.10 + 1.105 \, \mathrm{Sec}\theta \, . \qquad (39)$$

For further analysis, Figure 40 on the right shows an expanded plot for zenith angles less than 70^0. It also plots the tipping curve (39), and for comparison shows the previous tipping curve equation (25) with its larger slope of 1.26. This earlier tipping curve was obtained using the setup in Figure 35 which results in greater blockage due to the privacy panel and radiation leakage from surrounding objects. Unlike the nonlinear characteristic seen at large zenith angles, the slope difference seen for smaller zenith angles appears as a smaller effect in Figure 40.

Furthermore, upon repeating the previous analysis using the new tipping curve (39), the calibration equation becomes

$$\boxed{T_b = 310.6 + 38.0 \, V \, .} \qquad (40)$$

Also, after substituting (39) into (40) the calibrated tipping curve equation now becomes

$$\boxed{T_b = 2.7 + 42.0 \, \mathrm{Sec}\theta \, .} \qquad (41)$$

Finally, upon applying (41) to (37) with T_M = 285 *K* the opacity is 0.192. Also, the transmittance becomes 0.825 with $TPW = -W\,[\ln\tau + \alpha_{O2}]$ = 48 mm. This is a 10 mm decrease in *TPW* than that obtained previously using the setup in Figure 35, which contains more error sources. This smaller amount of water vapor is more reasonable so that the corresponding calibration equation (40) should be more accurate than that of equation (32).

For comparison with above results, an additional set of tipping curve measurements was taken on April 3, 2019. During this early spring period the trees were bare and the water vapor amount is much less than during the summer period. Figure 41 (Left) shows a plot of the radiometer measurements for this day in addition to the natural logarithm plot (Right). Both quantities are plotted as a function of air mass (Sec θ). Due to the small obstruction by trees a smaller elevation angle can be obtained so that the maximum zenith angle is 80 degrees (Sec θ = 5.76). The resulting calibration equation now becomes Tb = 293 +38.89 V which is very similar to that obtained previously and given by equation (40). Furthermore, the opacity given by the slope in the logarithmic plot is 0.0955 so that the resulting *TPW* is now only 22 mm.

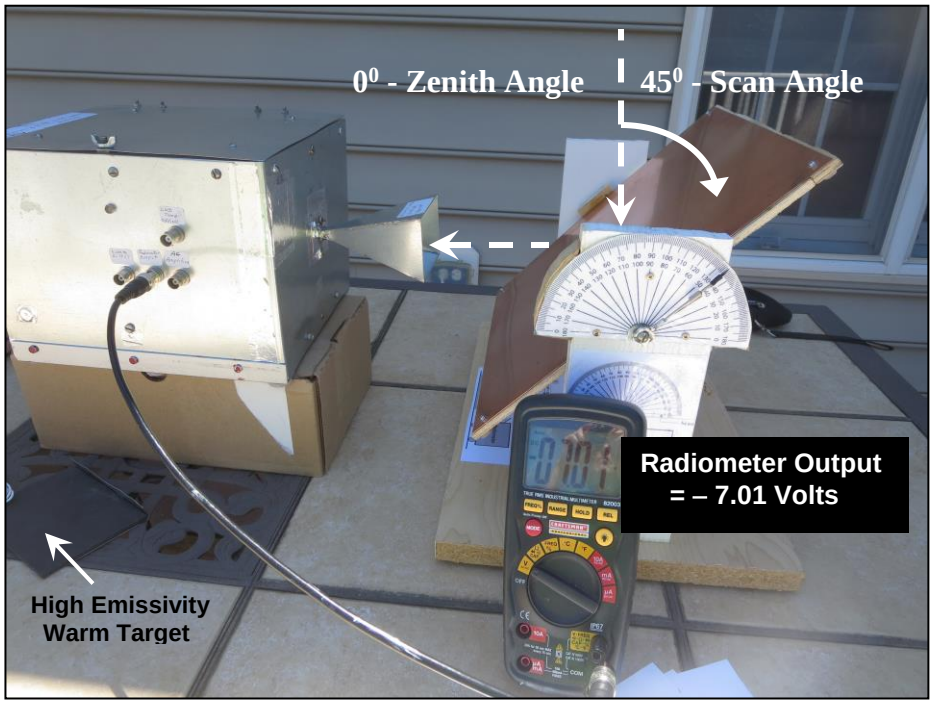

Figure 35- Tipping curve measurements of the 20 GHz radiometer on July 9, 2018. The radiometer antenna views space using a flat copper reflector. The zenith angle is varied between 0^0 to the largest unobstructed slant angle of 70^0. The picture shows the upward viewing scan angle of 45^0, corresponding to a zenith angle of 0^0 and radiometer voltage of -7.01 volts.

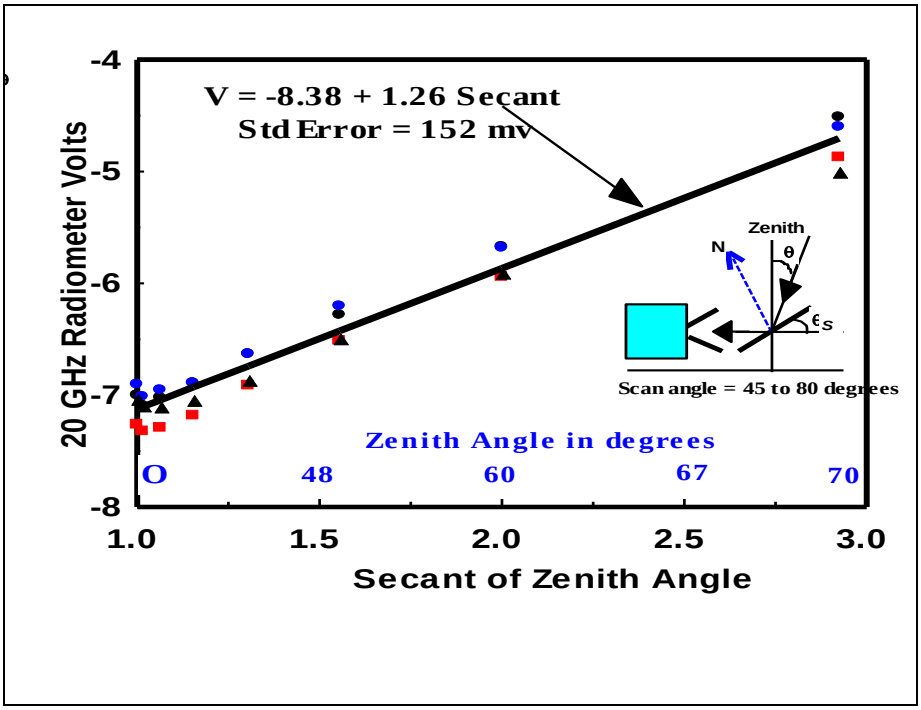

Figure 36- Tipping curve measurements on July 9, 2018 for the 20 GHz radiometer use the setup shown in Figure 35. For a consistency check, the series of eight angle measurements was repeated four times. The plot shows the data and straight line fit between the radiometer voltage and secant of zenith angle, θ. The resulting calibration equation based on the plotted data is given by equation (32), *i.e.,* $T_b = 303.62 + 35.91$ V.

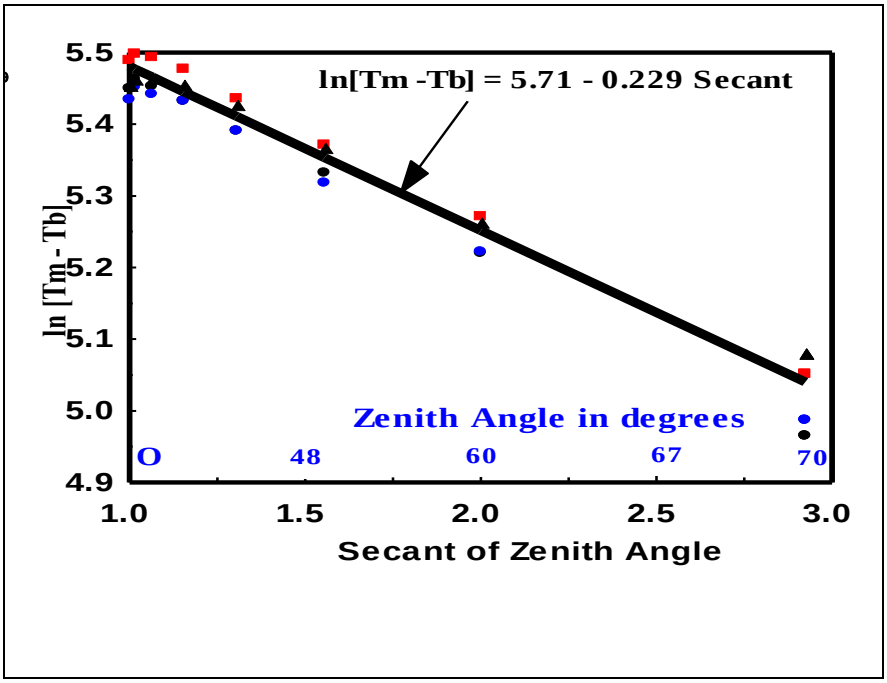

Figure 37- Tipping curve measurements in Figure 36 is used to calibrate the 20 GHz radiometer. The resulting calibrated brightness temperature given by equation (32) is used to obtain the atmospheric opacity by plotting ln (T_M -T_b) as a function of *Sec* θ. The straight line fit shown above is then applied to equation (34) to obtain the opacity, which is the negative slope of 0.229.

Figure 38- Tipping curve absorption measurements made in 1946 by Dr. Robert Dicke along with his associates. Starting on the Left is E. Beringer, R. Kyhl, A. Vane and R. Dicke. This picture is contained in the MIT Rad Lab Book “Five Years”. It shows Dicke holding up an absorber in front of one of his radiometers while a chart recorder on the ground plots the measurements.

Figure 39- Clear sky tipping curve measurements of the 20 GHz radiometer made August 26, 2018. Unfortunately, blockage of the sky radiation at low elevation (large zenith angle) occurs by the surrounding trees, house and privacy panel. To minimize blockage the radiometer is mounted on a tripod that is elevated on a table. The right picture shows the view seen by the radiometer when the antenna views at low elevation. Observations for zenith angles greater than 70^0 are obstructed by the trees and house shown in the picture.

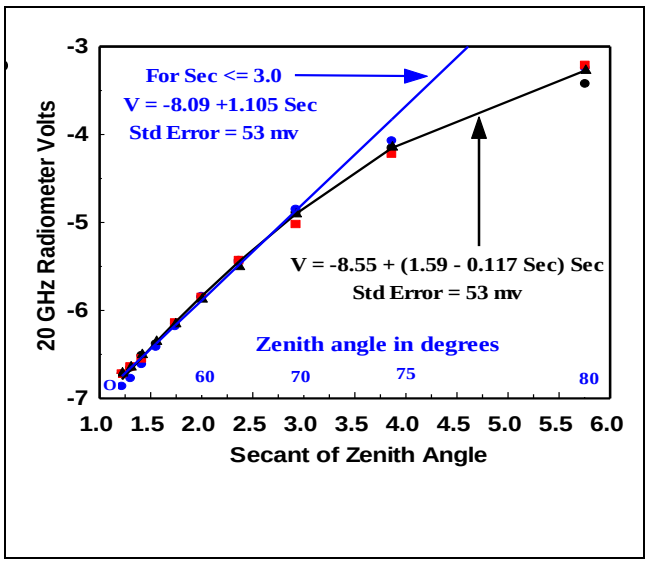

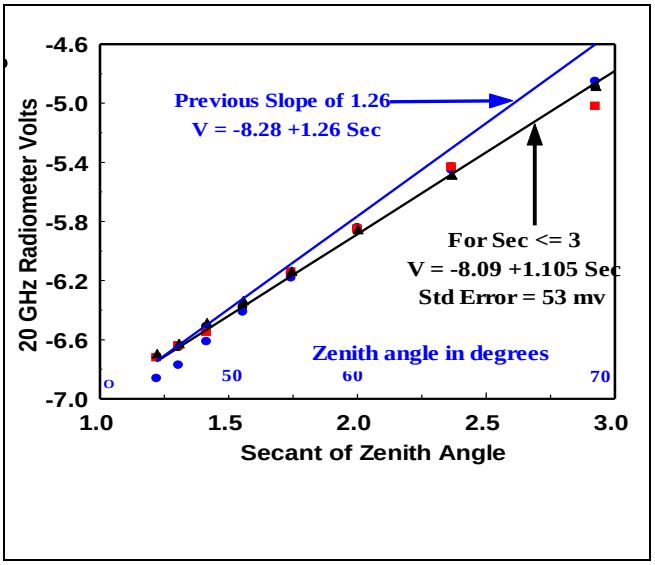

Figure 40- Clear sky tipping curve measurements of the 20 GHz radiometer made August 26, 2018 using the improved setup in Figure 39. The left plot shows the data for all zenith angles ($\theta = 35^0$ to 80^0) while the right most plot is only for angles between 35^0 and 70^0. Radiometer voltage is plotted as a function of Sec θ in both plots where the measurements were repeated four times. The full range of angles in the left plot displays a nonlinear increase in voltage for Sec $\theta > 3$ due to obscurations described in the text. The Figure also shows a best fit quadratic equation in addition to the linear tipping curve equation V = - 8.09+ 1.105 Sec θ derived for Sec $\theta < 3$. The right Figure only shows data for Sec $\theta < 3$ along with the linear tipping curve equation. For comparison, the right most Figure also shows the previous tipping curve equation of Figure 36 having a slope 1.26 with the intercept slightly changed. This larger slope of 1.26 was obtained from the measurements obtained using the setup in Figure 35.

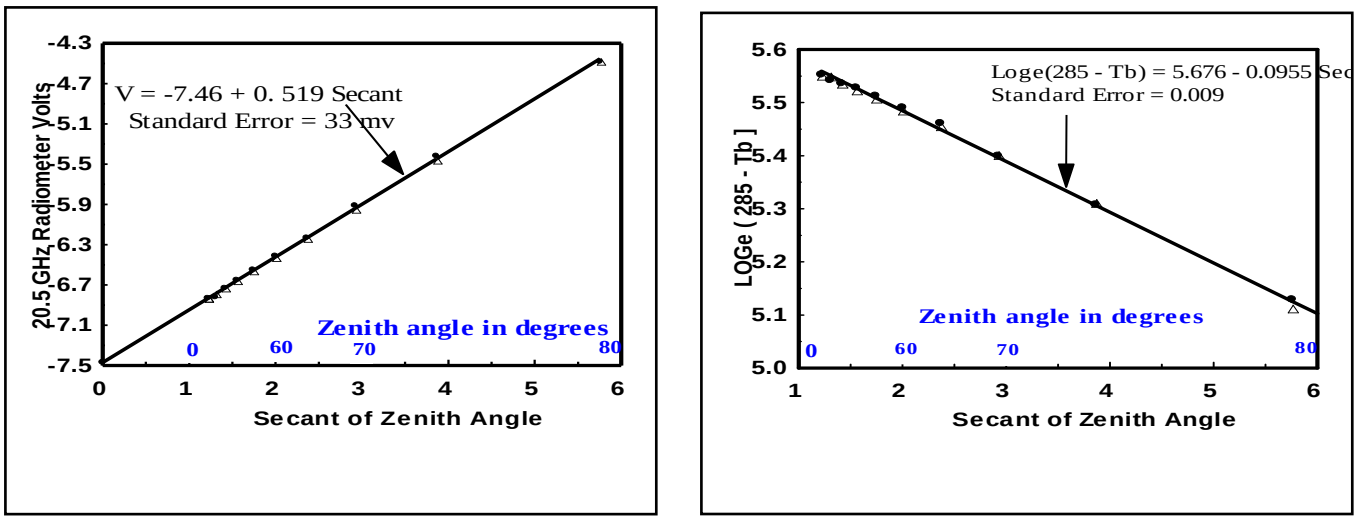

Figure 41- Clear sky tipping curve measurements of the 20 GHz radiometer obtained on April 3, 2019. At this time the trees were bare and the water vapor is less than that for the summer period exhibited in the measurements of Figure 40. As such, compared to Figure 40, the left-most plot now shows data for zenith angles between 35^0 to a maximum of 80^0 with Sec θ = 5.76. Radiometer voltage is again plotted against Sec θ where the measurements repeated two times. The tipping curve equation now becomes V = - 7.46+ 0.519 Sec θ so that the slope of 0.519 is much smaller than the slope of 1.105 found in Figure 40. Also shown on the right is a plot of the natural logarithm term contained in equation (34), plotted against Sec θ. The negative slope of 0.0955 is the atmospheric opacity for this day which is much smaller than the 0.229 value displayed in Figure 37.

8.4 Water Vapor and Cloud Water

Having calibrated the radiometer using the tipping curve measurements the radiometer can be used to determine the water vapor by combining (27), (38) and (40). The algorithm is obtained by considering $TPW << W(\nu) = 270$ mm in (35) and neglecting the small cosmic radiation term in (27), *viz.*,

$$T_b \cong (1-\tau^{Sec\theta})T_M \cong \left[\alpha_{O2}(\nu) + TPW/W(\nu)\right]T_M \; Sec\theta \qquad (42a)$$

so that

$$TPW \cong -W(\nu)\,\alpha_{O2}(\nu) + \left[W(\nu)/T_M\right]T_b \; Cos\theta \qquad (42b)$$

where T_b is given by the calibration equation (40).

Substituting the α and W parameters from Table 4 into (42b) with $T_M \equiv 285\ K$,

$$TPW \cong -3.78 + 0.947\, T_b \; Cos\theta\,. \qquad (43)$$

However, as discussed next, equation (43) only provides accurate *TPW* measurements under clear sky conditions. For cloudy skies, dual frequency radiometer measurements are needed to account for cloud liquid water absorption. The second radiometer frequency is generally chosen to be greater than 22 GHz so that it is more responsive to clouds and less sensitive to water vapor than at 20.5 GHz. Fortunately, however, the 12

GHz radiometer is shown next to have sufficient sensitivity to clouds to correct the 20 GHz measurements. As such, water vapor measurements can be obtained for clear as well as cloudy skies by combining the 12 and 20 GHz radiometer measurements.

Algorithms for determining *TPW* and *Q* are obtained using (27) with the transmittance given as the product of the clear transmittance (38) and cloud transmittance (18), *i.e.*,

$$\tau(\nu) = \tau_{O2}\tau_{H2O}\tau_{CLD} = e^{-\alpha_{O2}(\nu)}\ e^{-TPW/W(\nu)}\ e^{-Q/Q(\nu)}\ . \qquad (44)$$

with all of the transmittance parameters listed in Table 4 for the 12 and 20 GHz radiometer center frequencies of 11.7 and 20.5 GHz.

Table 4: Atmospheric Transmittance Parameters, $\alpha_{O2}(\nu)$, $W(\nu)$ and $Q(\nu)$

Radiometer	**Center Frequency**	**Oxygen**	**Water Vapor**	**Cloud (T_{CLD} = 275 *K*)**
20 GHz	ν_1= 20.5 GHz	$\alpha_{O2}(\nu_1)$ = 0.014	$W(\nu_1)$ = 270 mm	$Q(\nu_1)$ = 11.9 mm
12 GHz	ν_2= 11.7 GHz	$\alpha_{O2}(\nu_2)$ = 0.010	$W(\nu_2)$ = 3989 mm	$Q(\nu_2)$ = 35.8 mm

Substituting (44) into (27) and neglecting the small cosmic radiation term,

$$\frac{TPW}{W(\nu)} + \frac{Q}{Q(\nu)} + \alpha_{O2}(\nu) = -\psi(\nu)\ , \qquad (45a)$$

where $$\psi(\nu) = Cos\theta\ \ln\left[1 - T_b(\nu\ )/T_M\right]\ . \qquad (45b)$$

Solving (45a) for *TPW* and *Q* using dual frequency (ν_1, ν_2) brightness temperatures,

$$TPW = \frac{W(\nu_2)}{\eta - \beta}\left[\psi(\nu_1) - \eta\,\psi(\nu_2) + (\rho - \eta)\,\alpha_{O2}(\nu_2)\right] \qquad (46a)$$

and $$Q = -\frac{Q(\nu_2)}{\eta - \beta}\left[\psi(\nu_1) - \beta\psi(\nu_2)\ + (\rho - \beta)\,\alpha_{O2}(\nu_2)\right] \qquad (46b)$$

where $$\beta = \frac{W(\nu_2)}{W(\nu_1)},\ \eta = \frac{Q(\nu_2)}{Q(\nu_1)},\ \rho = \frac{\alpha_{O2}(\nu_1)}{\alpha_{O2}(\nu_2)}\ . \qquad (46c)$$

Except for very large amounts of water vapor and cloud liquid water, $T_b(\nu) << T_M$ so that $\psi_1 \cong -T_b(\nu_1)\,Cos\theta/T_M$ and $\psi_2 \cong -T_b(\nu_2)\,Cos\theta/T_M$. Equations (46a) and (46b) then become linearized as

$$TPW \cong \frac{\eta-\rho}{\beta-\eta} W(\nu_2)\, \alpha_{O2}(\nu_2) + \frac{W(\nu_2)\, Cos\theta}{(\beta-\eta)\, T_M} \left[T_b(\nu_1) - \eta\, T_b(\nu_2) \right], \qquad (47a)$$

$$Q \cong -\frac{\beta-\rho}{\beta-\eta} Q(\nu_2)\, \alpha_{O2}(\nu_2) - \frac{Q(\nu_2)\, Cos\theta}{(\beta-\eta) T_M} \left[T_b(\nu_1) - \beta\, T_b(\nu_2) \right]. \qquad (47b)$$

Substituting the transmittance parameters from Table 4 into (47a, b) we obtain

$$TPW \cong 7.59 + Cos\theta \left\lfloor 1.19\, T_b(\nu_1) - 3.57\, T_b(\nu_2) \right\rfloor, \qquad (48a)$$

$$Q \cong -0.40 - Cos\theta \left\lfloor 0.010\, T_b(\nu_1) - 0.157\, T_b(\nu_2) \right\rfloor. \qquad (48b)$$

Equations (48a, b) use weighted brightness temperature differences to obtain *TPW* and *Q*. Note that *TPW* is positively correlated to the 20 GHz measurements with the 12 GHz measurements providing cloud liquid water corrections. Conversely, *Q* is positively correlated to the 12 GHz measurements with the 20 GHz measurements providing small water vapor corrections.

More accurate coefficients than those in (48a, b) are obtained using statistical regression analysis of simulated brightness temperature measurements (predictors) against the water vapor and cloud liquid water (predictands) in the data. The simulated results also provide the standard error of the retrieved parameters. Brightness temperatures are obtained using the radiation transfer equation (5) with the mean atmospheric temperature in (6) calculated using a global sample of temperature, water vapor and cloud liquid water profiles. The vertical distribution of temperature and water vapor was obtained using an historical sample of radiosonde data with the total precipitable water increasing from 2 mm to 60 mm as the surface temperature increases from 245 *K* to 303 *K*. Since cloud liquid water is not available from radiosonde data, clouds are artificially introduced at different heights into each atmospheric profile. The liquid water amount is varied between 0 mm to a maximum of 1 mm, with the smallest liquid water applied to clouds having temperatures below freezing. For reference it should be noted that actual satellite and ground-based radiometer measurements have shown that liquid water greater than about 0.3 mm is generally associated with rain clouds. In fact, it has been customary to identify rain from satellites using such a liquid water threshold.

Upon applying a least squares regression analysis to the simulated data, the resulting dual frequency algorithms for water vapor and cloud liquid water are similar in form to (48a, b), but with slightly different coefficients, *i.e.*,

$$TPW = 10.39 + 1.33\, T_b(20) - 3.68\, T_b(12) \quad \text{with} \quad SE = 0.86\ mm, \qquad (49a)$$

$$Q = -0.80 - 0.010\, T_b(20) + 0.159\, T_b(12) \quad \text{with} \quad SE = 0.07\ mm. \qquad (49b)$$

For comparison, the optimal single frequency algorithms for water vapor and cloud liquid water are

$$TPW = -6.54 + 0.86\, T_b(20) \quad \text{with} \quad SE = 4.49\ mm, \qquad (50a)$$

$$Q = -0.59 + 0.098 T_b(12) \quad \text{with} \quad SE = 0.11\ mm. \qquad (50b)$$

The above equations give the dual frequency and optimal single frequency algorithms for zenith viewing ($\theta = 0^0$) along with their standard errors. For visualization, Figure 42 plots the corresponding retrieved water vapor obtained from the algorithms against the actual data set values. Similarly, Figure 43 shows the results for cloud liquid water. Each Figure plots the results obtained using dual frequency brightness temperatures (Left) as well as that obtained using single frequencies (Right).

Comparing (50a) with (49a) we see that the 12 GHz radiometer measurements provides cloud corrections of *TPW*, reducing the standard error (SE) from 4.49 mm to 0.86 mm. On the other hand, comparing (50b) with (49b) we see that the 20 GHz radiometer provides small water vapor corrections of *Q*, reducing the error from 0.11 mm to 0.07 mm. Although this appears to be a small improvement it is important for measuring non-precipitating clouds whose liquid water is generally less than 0.3 mm. However, to better measure clouds with small liquid water content a higher frequency than 12 GHz is needed. For example, simulations obtained using 20.5 GHz and 31 GHz measurements result in a liquid water error of 0.06 mm compared to 0.07 mm when using the 20.5 GHz and 12 GHz measurements. Also, the error of *TPW* was found to be reduced from 0.86 mm to 0.61 mm when substituting the 31 GHz for the 12 GHz measurements.

I should also mention that such a dual frequency Dicke radiometer at 20.6 and 31.6 GHz was constructed using a single corrugated horn antenna around 1979 by the late Dr. David Hogg of NOAA in Boulder, Colorado[4]. This highly reliable instrument was used in an unattended continuous mode of operation at airports in Denver, Colorado and Washington, D.C. to provide real time data of water vapor and cloud liquid water under all weather conditions to the National Weather Service Forecast Office. A more detailed description of the instrument along with its calibration and measurements is given in an earlier footnote[3]. As a result of its high performance, similar dual frequency radiometers were developed by other organizations for research and operational use.

Lastly, while the coefficients in (48a, b) are similar to those in (49a, b) these final coefficients are considered more accurate since they are based on a larger data base that is more representative. Also, the single frequency water vapor coefficients in (49a) are also considered more accurate than those in (43) due to the larger more representative data base used in their derivation. I should also mention that the use of the logarithmic predictors as in (45b) were also analyzed and found to decrease the *TPW* error from 0.86 mm to 0.48 mm. This reduction in error is mainly due to the saturation effect seen in Figure 42 for *TPW* > 50 mm when using linear predictors. However, the error in *Q* was not reduced using the logarithmic predictors. This is due to the variations seen in the plotted data do to parameters such as cloud temperature, which can not be accounted for using either linear or logarithmic predictors.

[4] A Dual-Channel Microwave Radiometer for Precipitable Water Vapor and Liquid Water, IEEE Transactions on Geoscience Electronics, Vol. GE-17, No.4, Oct 1979, pp 129-136.

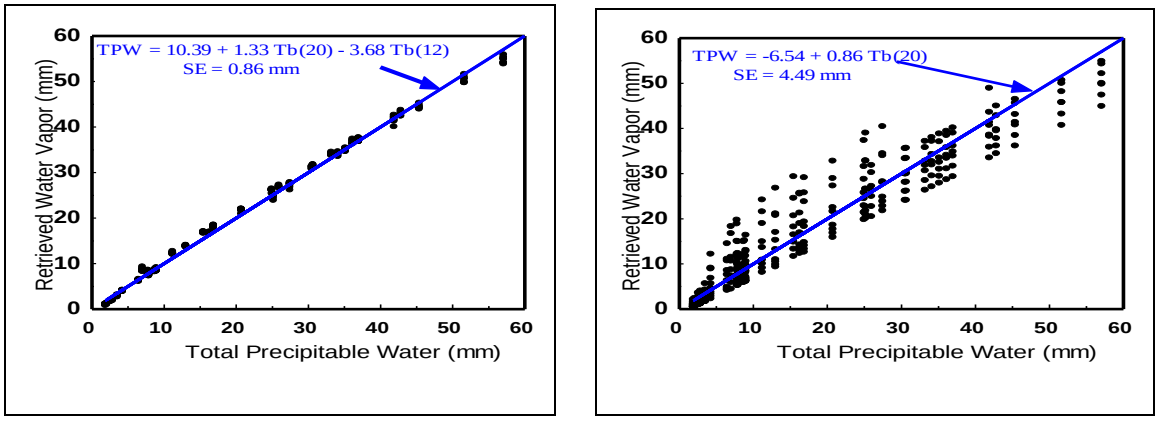

Figure 42- Retrieval of TPW based on simulations. The Left and Right-most Figures show the application of the dual and single frequency algorithms to the simulated data, respectively. Also shown are their standard errors (SE) and the one to one lines in Blue.

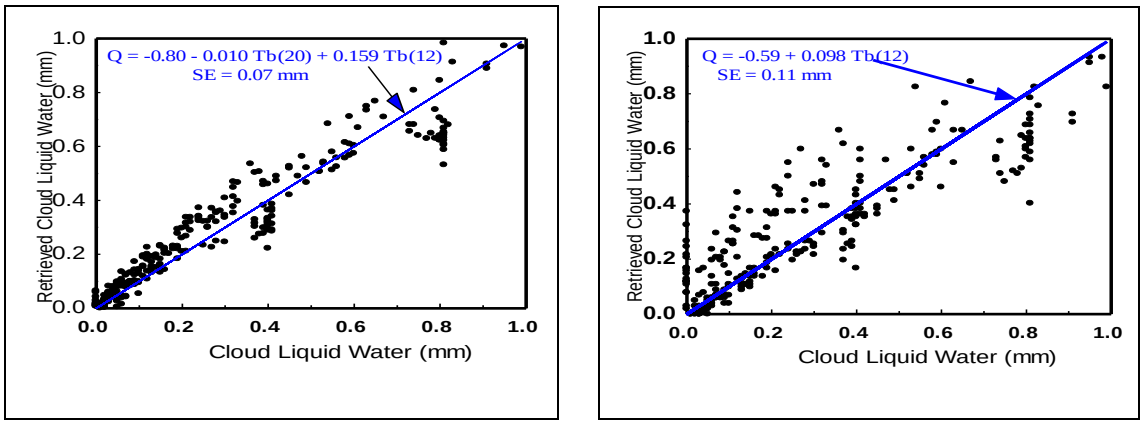

Figure 43- Retrieval of Q based on simulations. The Left and Right-most Figures show the application of the dual and single frequency algorithms to the simulated data, respectively. Also shown are their standard errors (SE) and the one to one lines in Blue.

9. Concluding Remarks

Microwave radiometry has its origin in radio astronomy. However, since the beginning of the satellite era in the 1960's its application has been expanded to also include earth remote sensing. My own experience with radiometers began in 1971 when I worked at NASA and then at NOAA to derive atmospheric and surface parameters from radiometer measurements to help monitor, analyze and forecast the weather and climate. Upon retiring from the government in 2005 I considered building microwave radiometers using components readily available from the Internet. As the project evolved I documented my progress using photos and PowerPoint presentations. This material was used in this report to summarize my construction of a 3.7, 11.7 and 20.5 GHz radiometer. The report also describes the calibration, observations and analysis of the radiometer measurements.

The first half of this report describes the radiometer construction while the second half demonstrates some of its applications. For completeness, it includes many issues I came across while developing the instruments and taking measurements. It also describes experiments demonstrating the radiometer use for detecting surface wetness, water vapor, clouds and rain water content. Most of these measurements were observed through a glass patio door. As such, model simulations and analysis is used to help understand the effect glass has on the measurements. The surface and atmospheric measurements also demonstrate the high quality and precision of these very stable Dicke radiometers.

The rain, clouds, water vapor and surface wetness measurements demonstrated here are only a few of many others that are derived operationally under nearly all weather conditions using ground based and earth viewing satellite microwave radiometers. A good reference to these applications in addition to other topics is given in the 1993 book "Atmospheric remote sensing by microwave radiometry", Edited by M. A. Janssen, and published by John Wiley & Sons. Figure 44 shown below is a composite picture from the book's cover of sea ice, snow cover, rain rate and cloud liquid water measured using an instrument called the Special Sensor Microwave Imager (SSM/I), which was first launched aboard a polar orbiting satellite in 1987. The SSM/I is a dual polarized multi-frequency (19, 22, 37 and 85 GHz) radiometer developed by the Navy to measure these parameters in addition to water vapor, sea surface temperature and wind speed. Of particular importance for climate monitoring is the 40 year global record of atmospheric temperature obtained from a different series of satellite radiometers operating in the 50 to 60 GHz oxygen band which was developed by NOAA, NASA and the Air Force. None of this could be obtained without the high reliability and precision of Dicke radiometers. As shown in Figure 26, even my instruments operate over long periods without any drift or changes in calibration. This is due to the Dicke radiometer design which reduces spurious noise and minimizes temperature drift and gain variation effects. An excellent review of the subject is given by M. E. Tiuri in the 1966 book "Radio Astronomy" by John. D. Kraus, published by McGraw - Hill, Inc.

Historically, beginning in the 1970's, earth viewing satellite radiometers have employed the Dicke design to avoid the need for frequent calibration. However, since the late 1990's, some satellite instruments have opted to use the simpler total power radiometer design. This was based on data analysis, showing high stability as long as the radiometer can step quickly (*e.g.*, every 30 seconds) through a calibration cycle whereby its antenna views the cosmic background and a high emissivity temperature monitored target. Ground based radiometers on the other hand still generally use the Dicke approach since it's difficult to ensure cloud-free calibration measurements in a timely manner. An alternative approach has been to use a precision noise diode input to supplement the cold space calibration measurements for both ground based and satellite instruments.

It should also be noted that although microwave technology has advanced considerably since 1944 when Dr. Robert Dicke first developed his instrument at the MIT Radiation Laboratory, the basic design hasn't changed much over time. However, as mentioned above, the application of microwave radiometers has well surpassed his original use, which was to primarily measure the gaseous atmospheric absorption from water vapor and oxygen. These observations together with radiation measurements of the moon, the sun, and the first estimate (~20 *K*) of the cosmic background microwave radiation were briefly mentioned in his 1946 landmark paper (*Phys. Rev.* 70, 340–348). It was some 16 years later while studying cosmology in the early 1960's that Dicke decided to revisit his

early radiometer experiment and improve on his cosmic radiation measurement. This work was however surpassed in 1964 by Drs. Arno Penzias and Robert Wilson at Bell Laboratories, who accidentally found the radiation while studying the noise in a satellite receiver. They both received Nobel Prizes for their very accurate 2.7 *K* cosmic radiation measurement at a frequency of 4 GHz.

In conclusion, I myself am grateful to have had the opportunity to work with many colleagues who shared my interest in applying this unique technology to measure the earth's atmosphere and its underlying surface from space. More importantly, upon finally building a radiometer, after many years of developing algorithms and analyzing data, I can fully appreciate Dicke's remarkable achievement. In fact, Wikipedia states that some believe Robert Dicke deserved a Nobel Prize just for the invention of this powerful measuring device. Hopefully, this article will encourage others to construct such an instrument for sensing the earth as well as astronomical sources, as it was first envisioned back in the 1930's by Karl Jansky.

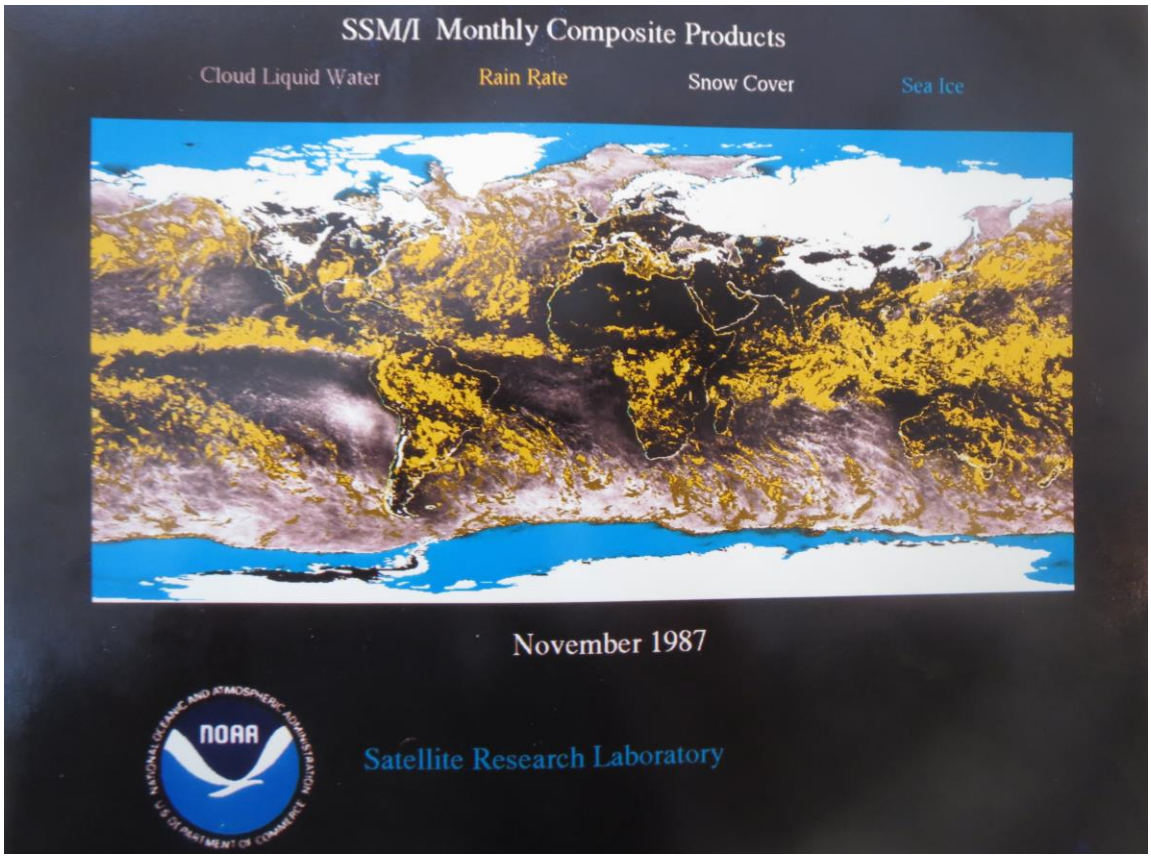

Figure 44 - Products such as those shown above are determined daily using the Special Sensor Microwave Imager (SSM/I). The daily products are monthly averaged to obtain this composite image. The SSM/I frequency and polarization measurements are combined using a decision tree to generate each product globally (*e.g.*, Grody, N.C., Classification of snow cover and precipitation using the SSM/I, *J. Geophys. Res*., 96, 7423-7435, 1991). Of particular importance is the highest frequency SSM/I channel at 85 GHz, which detects volume scattering by the millimeter size ice particles in rain clouds and snow cover.

10. References (*in order of citation*)

Swenson and Yang, "An Amateur Radio Telescope - V", *Sky and Telescope*, Vol. 56, No. 3, September 1978, pp 201-205.

Neils Skou, "Microwave Radiometer Systems: Design & Analysis", *Artech House, Inc*, 162 pgs., 1989.

C. Newton, T.E. Peterson and N. J. Perkins (Eds), "Five Years at the Radiation Laboratory, MIT", *The Andover Press, Ltd*., 205 pgs., 1946.

Robert H. Dicke, Robert Beringer, Robert L. Kyle and A. B. Vane, "Atmospheric Absorption Measurements with a Microwave Radiometer", *Physical Review*, Vol 20, No. 5, September 1, 1946, pp 340-349.

D.C. Hogg, F.O. Guiraud, J.B. Snider, M.T. Decker and E.R. Westwater, "A Steerable Dual-Channel Microwave Radiometer for Measurements of Water Vapor and Liquid in the Troposphere", *Journal of Climate and Applied Meteorology*, Vol. 22, May 1983, pp 789-806.

F.O. Guiraud, Joe Howard and D. C. Hogg, "A Dual-Channel Microwave Radiometer for Measurement of Precipitable Water Vapor and Liquid", *IEEE Transaction on Geoscience Electronics*, Vol. GE-12, No. 4, October 1979, pp 129-136.

John D. Kraus, "Radio Astronomy", *McGraw Hill*, 485 pgs., 1966.

Michael A. Janssen (Ed.), "Microwave Remote Sensing by Microwave Radiometry", John Wiley & Sons, 592 pgs., 1993

N. C. Grody, "Classification of snow cover and precipitation using the SSM/I", *Journal. Geophysical Research*, 96, 1991, pp 7423-7435.

Appendices.

A1. Pyramidal Horn Antenna

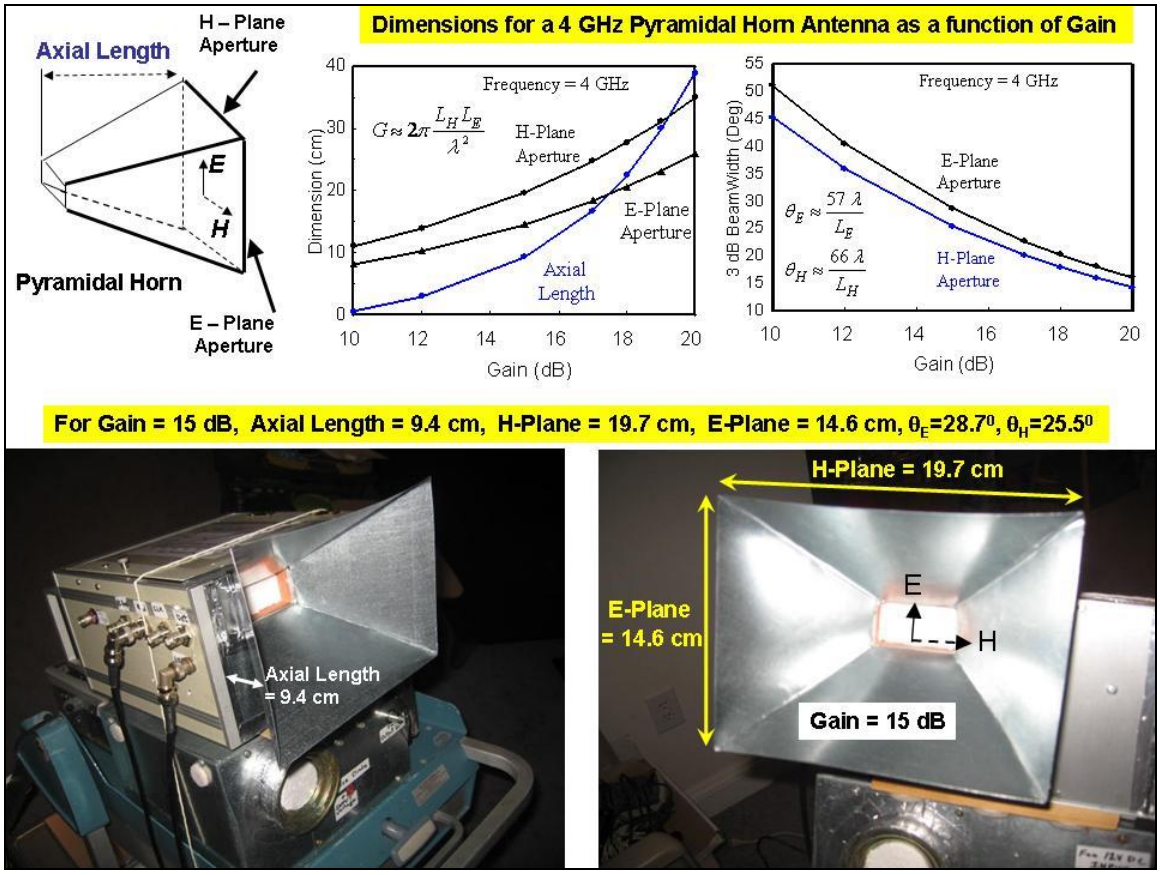

Figure A1. The top-middle figure shows the height, width and axial length of a pyramidal horn antenna. All parameters are plotted as function of gain for a frequency of 4 GHz. The top-right figure shows the 3 dB beamwidths in the E- and H-planes. The 4 GHz radiometer antenna shown in the bottom figures was designed to have a gain of 15 dB with about a 27^0 beanwidth. The approximate equations given in the top figures can be used to calculate the antenna dimensions at any wavelength. Note that the effective aperture is about 50% of its area, A, so that the gain is ½($4\pi A/\lambda^2$). The equations as well as a program to calculate exact dimensions were obtained from Paul Wade's online microwave web site at http://www.w1ghz.org/. It was used to obtain the dimensions for the 4 GHz as well as the 12 GHz radiometer antenna whose gain is 19 dB with a 16^0 beamwidth and 20 GHz radiometer whose gain is 20 dB. I should also mention that the polarization used by both radiometers is vertical as shown in the above figure. This polarization is preferred in order to minimize the reflections by glass when taking measurements through my patio door as shown in Figures 24 and 29.

A2. Temperature Controlled Fan

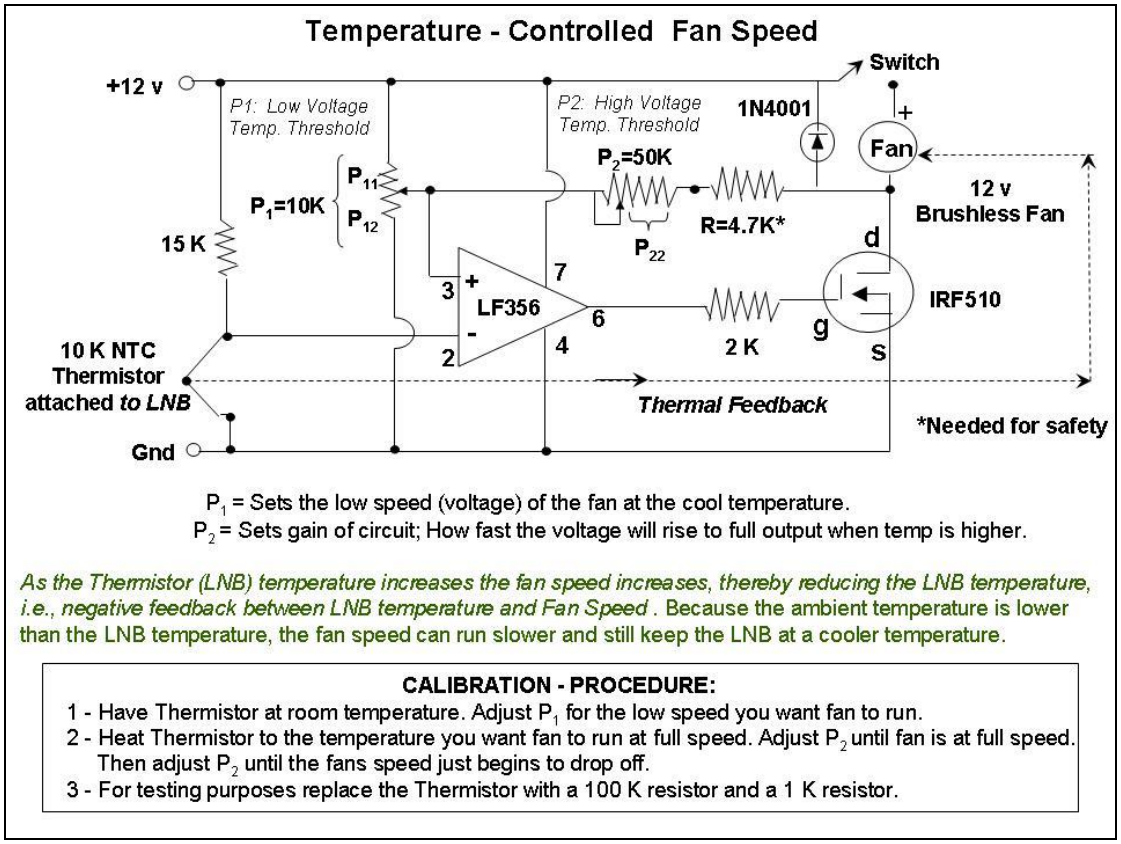

Figure A2. A temperature controlled fan speed circuit is used to cool the LNB by increasing the ambient temperature flow. The circuit uses a difference amplifier (LF356) whose negative voltage depends on the thermistor (10 K NTC) resistance, while the positive (reference) voltage is set using a 10 K resistive trimmer (P_1). Its differential output goes to the MOS-FET (IRF510) which injects more or less current into the brushless fan depending on the thermistor resistance. The thermistor is attached to the LNB so that thermal feedback between the fan speed and LNB temperature is used to keep the differential input voltage constant. The difference amplifier gain set by resistor P_2 determines how fast the circuit responds to temperature change.

A3. 12 GHz Radiometer

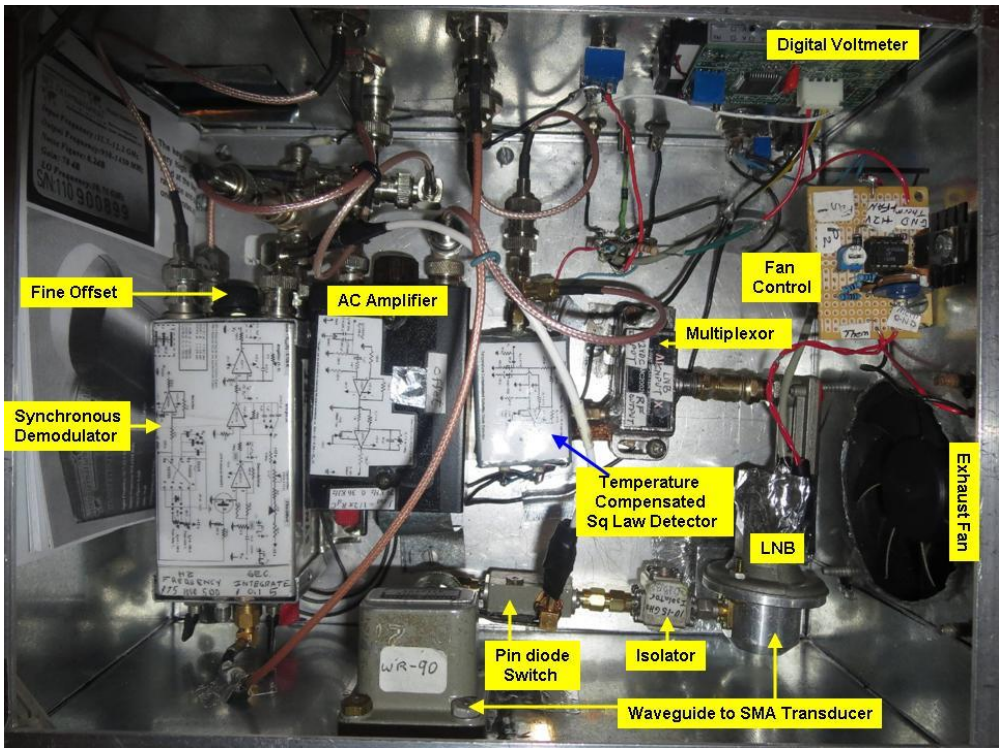

Figure A3. The top lid of the 12 GHz radiometer is opened (see Figure 2) to show the components. These are the same components referred to in the block diagram of Figure 3.

A4. Synchronous Demodulator

Figure A4-1 is the schematic diagram of the synchronous demodulator used in the 12 GHz radiometer. It also shows the waveforms at the different input and output stages of the circuit. A picture of the demodulator with its top opened and components labeled is shown in Figure A4-2. It is similar to the ones used in the 4 GHz and 20 GHz radiometers. Beginning from the right side of Figure A4-1, the input signal, V_{IN}, is the output from the AC amplifier. Note that V_{IN} is a square wave of voltage Ref when the pin diode switch in Figure 3 connects to its internal resistive load, followed in time with voltage Ant when the switch connects to the antenna input. The 10 µf input capacitor in Figure A4-1 removes any DC level from the AC amplifier output so that the unbiased waveform varies from (Ref-Ant)/2 to –(Ref-Ant)/2. This signal located at tap TP_1 goes to the demodulator, which is a unit gain difference amplifier constructed using half of a dual operational amplifier (OP2111).

The positive input of the operational amplifier at Pin 3 is switched from open to ground using the J-177 MOSFET transistor whose gate is driven by the NE555 clock generator. This is the same clock that energizes the pin diode switch. Note that the clock frequency can be set at 172 Hz, 500 Hz or 1000 Hz. Due to synchronization, the difference amplifier reverses the polarity of the Ant signal so that its output at TP_2 has amplitude (Ref – Ant)/2. As an example, Figure 5 shows the waveform at TP_2 when the 4 GHz radiometer views cold space. The demodulator output, TP_2, is next connected to an

integrator (OP2111) that smoothes the signal according to equation (7b). Note that T_b fluctuations are reduced by increasing the integration time from 0.1, 1.0 or 5.0 seconds. The integrator also reverses the input polarity at its output, and provides an adjustable offset to the last stage which is a DC amplifier of adjustable gain (1 to 6). As such, the DC amplifier output becomes G_2(Ant - Ref)/2 where G_2 is the amplifier gain. The DC amplifier uses an AD711 operational amplifier to assure very low noise and very small temperature drift.

Figure A4-2 shows a picture of the synchronous demodulator, which fits inside a small metal box. Small coax connectors are used to access the TP1 and TP2 diagnostic outputs while four BNC connectors are used for the input and output signals as well as the two clock signals, one having positive and the other negative voltage. The negative clock is obtained using the inverter circuit shown in Figure A4-1. It is needed to drive the Hewlett Packard pin diode switch (33102A). However, the 4 GHz and 20 GHz radiometers uses a General Microwave pin diode switch (M862B) which only requires a positive switching voltage. As such, the inverter stage is omitted in the 4 GHz synchronous demodulator. The positive clock signal can also be used to synchronize the sweep of an oscilloscope to observe the signals from the demodulator, AC amplifier and detector as seen in Figure 5. I also found that a 500 Ω external resistor can be added to reduce the current that turns the M862B switch off from its specification of 37 ma to 16 ma at 12 volts without affecting its performance.

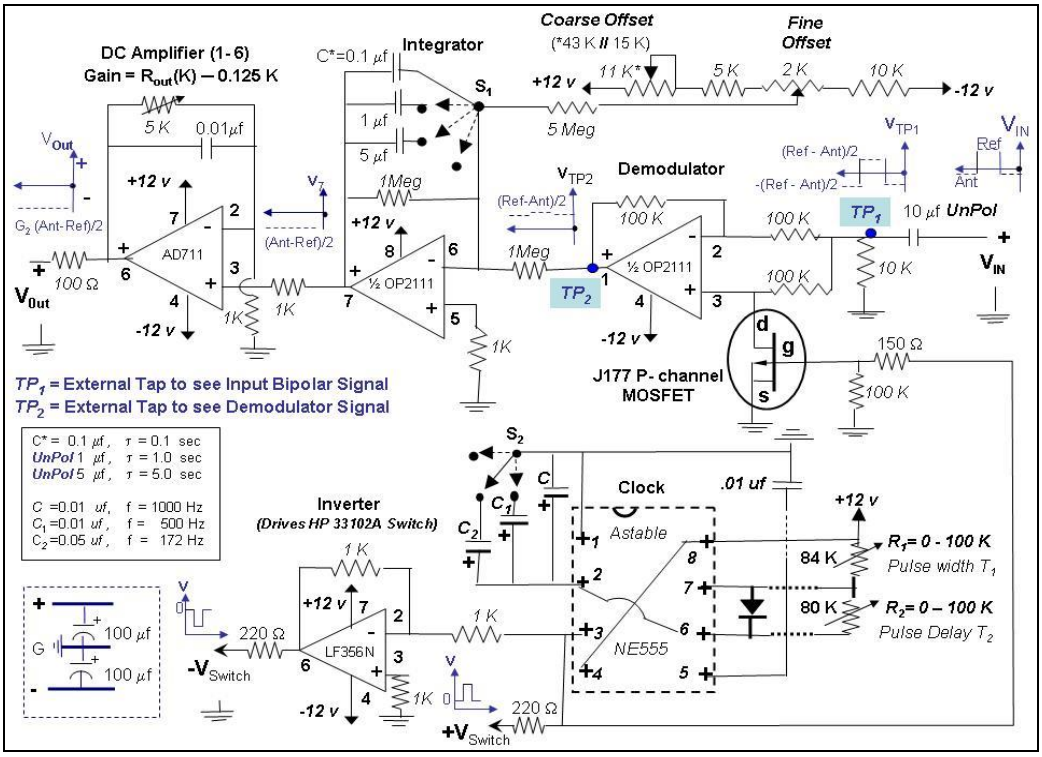

Figure A4-1. Synchronous demodulator used in the 12 GHz radiometer. Starting from the input on the left, it uses operational amplifiers (op amps) connected as a difference amplifier, integrator and DC amplifier. The circuit also contains a NE555 clock generator and MOSFET transistor whose gate is driven by the clock to switch the difference amplifier gain to +/- 1. Finally, the last stage op amp is connected as an inverter to provide a negative clock signal to drive the HP 33102A pin diode switch shown in Figure 3. The 4 GHz and 20 GHz radiometer circuits do not have the inverter since it uses a General Microwave M862B pin diode switch that only requires a positive clock signal.

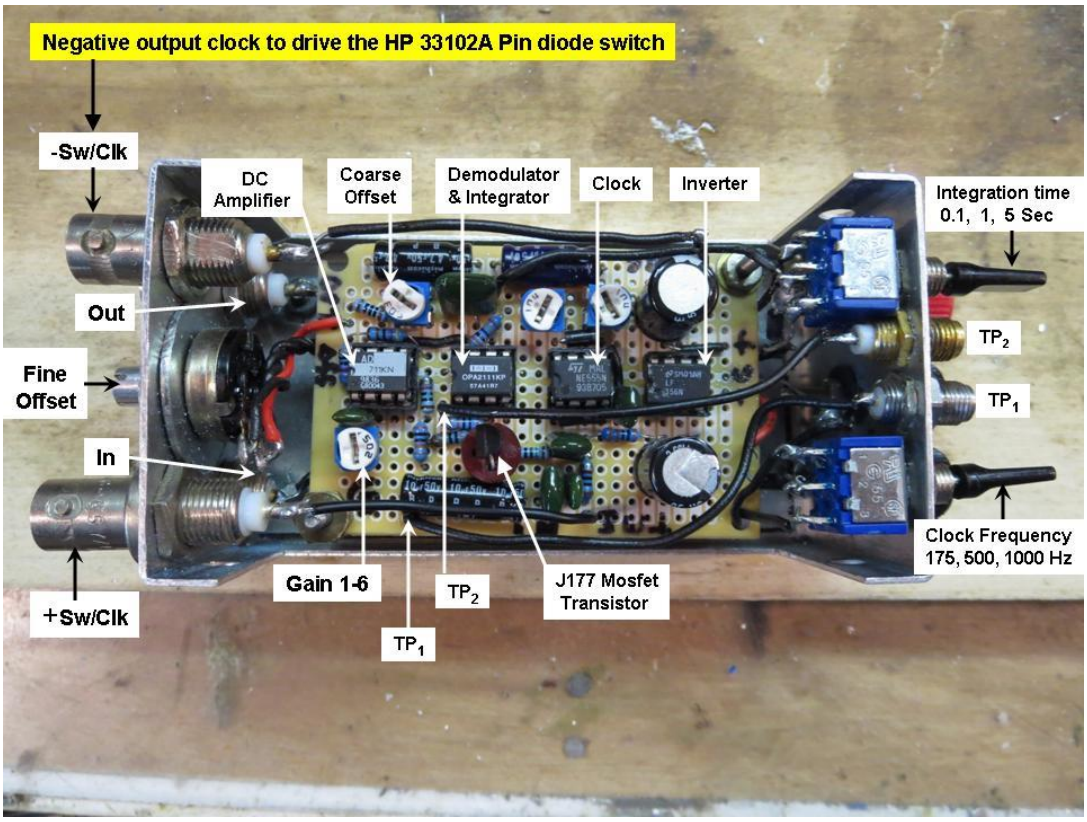

Figure A4-2. Synchronous demodulator used in 12 GHz radiometer. The case is opened to view the components, along with input and output connectors. The circuit board contains the variable resistors used to set DC amplifier gain and coarse offset, while the fine offset adjustment is outside the case. The outside switches on the right set the integration time and clock frequency.

A5. Temperature Compensated Detector

Figure A5 shows the temperature compensated detector used in the 4 GHz radiometer. The circuit uses a matched pair of Schottky diodes (HSMS - 282P) connected to a well balanced difference amplifier in the form of an instrumentation amplifier (AD620) as shown in Figure A5. One of the diode sections is used as reference while the other is connected to the input, which is the LNB *IF* output signal. The difference output then approximately cancels the temperature effect since both diodes operate at nearly the same temperature. To assure that the detector's output current varies approximately as the input voltage squared, or power, a very small current bias of 25 μa is applied. This stems from the fact that the diode response is greater than square law at low signal levels and is closer to a linear voltage detector and rectifies at high levels. Only between the noise level and around -20 dBm does a Schottky diode respond linearly to power, as shown in Figure 14. This is the square law region where the detector and radiometer responds linear to power or brightness temperature.

The gain of the AD620 difference amplifier can be set between 2 and 100 using the 50 K ohm variable resistor. The equation for the gain is $G_d = 1 + 49.4/(R_G + 0.47)$ where R_G is the resistance in kilohms. A gain of 10 is however found to be sufficient so that the resistor is set to 5 K. This gain is adequate even when the detector input is at its smallest voltage,

i.e., when the radiometer views the warm reference load, T_R. Furthermore, you will note that from the schematic diagram, a 47 ohm input resistor is used to reduce the maximum input signal when the radiometer views space, so that the Schottky diode is not saturated but operates linearly with power. This is shown by the detector measurements in Figure 19. Note that the detector operates approximately linearly with input power, or voltage squared, with errors less than +/- 0.2 dBm for power input between -30 dBm to -12 dBm. The 12 GHz detector is similar to that shown in Figure A5 except that it uses an AD711 operational amplifier with a fixed gain of 10 rather than the instrumentation amplifier. It also uses an HSMS 2825 matched pair Schottky diode rather than the HSMS 282P. The connections between the Schottky diode and difference amplifier inputs should be kept as short as possible (< 1 cm) to minimize radiation loss and coupling effects. However, even when minimizing the connections, Figure 29 shows a narrower frequency response of the 20 GHz radiometer detector beyond that of the individual element when the diode is connected using bulk circuit components.

As an alternative, many chip manufacturers offer RF detectors that operate over a wide dynamic range of input power and temperature. One such example is the LTC5509 chip by Linear Technology. It is available in a SC70 package and is specified to operate between 0.3 to 3 GHz as a square law detector between -30 dBm to 6 dBm input power. It uses a dual Schottky diode that is temperature compensated using a circuit similar to that of Figure A5 but having a buffer amplifier with a gain of two. I found the measured sensitivity to be 0.56 mv/μw at 1.4 GHz. This is nearly a factor of 10 less than the detector sensitivity given by equation (9b) which uses the circuit described above. Therefore, an additional amplifier with a gain of 10 is needed after the detector to increase my 4 GHz radiometer output from about -1 volt to -10 volts when viewing space. As such, the LTC5509 detector plus amplifier performs similar to that shown in Figure A5, which also uses an amplifier having a voltage gain of 10.

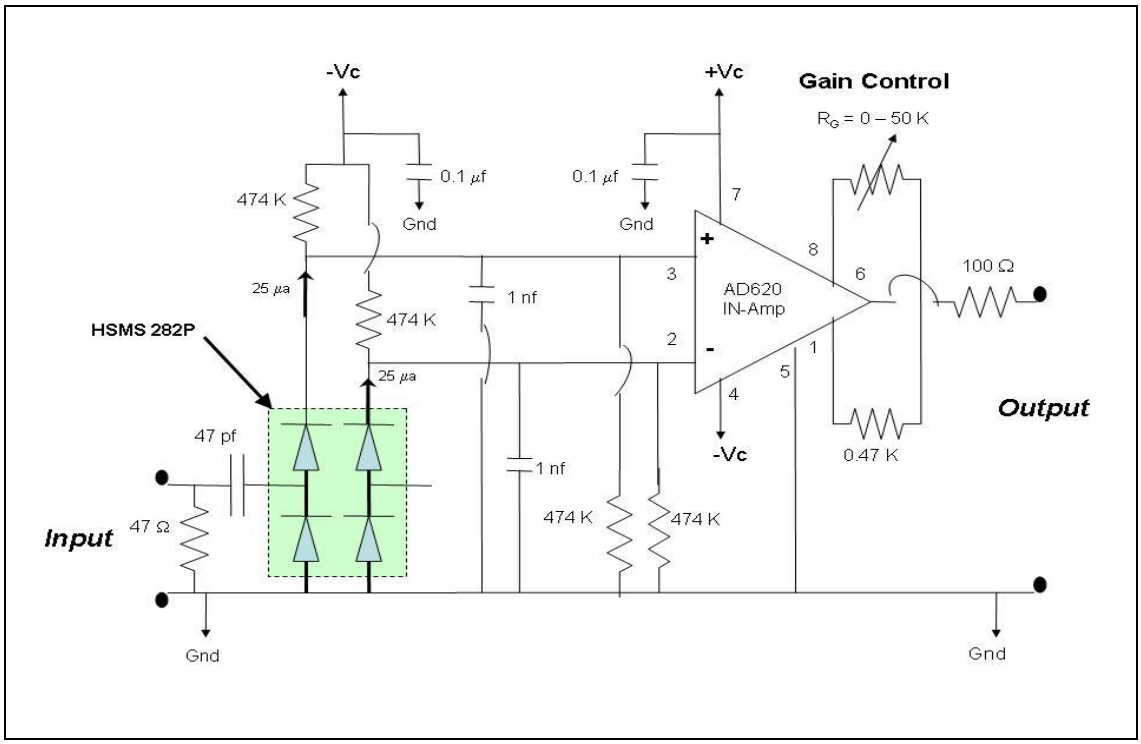

Figure A5. Temperature compensated square law detector for the 4 GHz radiometer uses an HSMS 282P balanced Schottky diode and an AD620 instrumentation amplifier that is powered using a supply voltage, V_C, of +/-12 volts. The amplifier gain can be varied from 2 to 100 by setting the resistor R_G according to the equation G_d =1+ 49.4/(R_G+ 0.47). To optimize the dynamic range, the diodes are slightly forward biased (25 μa).

A6. AC Amplifier

The AC amplifier in Figures 3 and 4 was designed using two single AD711 operational amplifiers as shown in the Figure A6. These particular operational amplifiers were chosen because of their very small temperature drift, low noise and large gain bandwidth product of 3 MHz. The AD711 also has an internal circuit to remove any internal DC offset using an external resistor. The 10 K trim resistor shown in Figure A8 provides the fixed offset adjustment. The first amplifier acts as a buffer stage with a gain of 2 while the second stage has an adjustable gain from 1 to 1000 using a 1 megohm variable resistor. Therefore, the total gain can be set from 2 to 2000. This gain can be determined by measuring the DC output resistance of the amplifier, *i.e.*, Gain = 2 R_{OUT} where R_{OUT} is in kilohms. The only change I would make is to replace the 1 megohm variable resistor with a precision stepped attenuator, since I found that the variable resistor can change it's value slightly over long time periods.

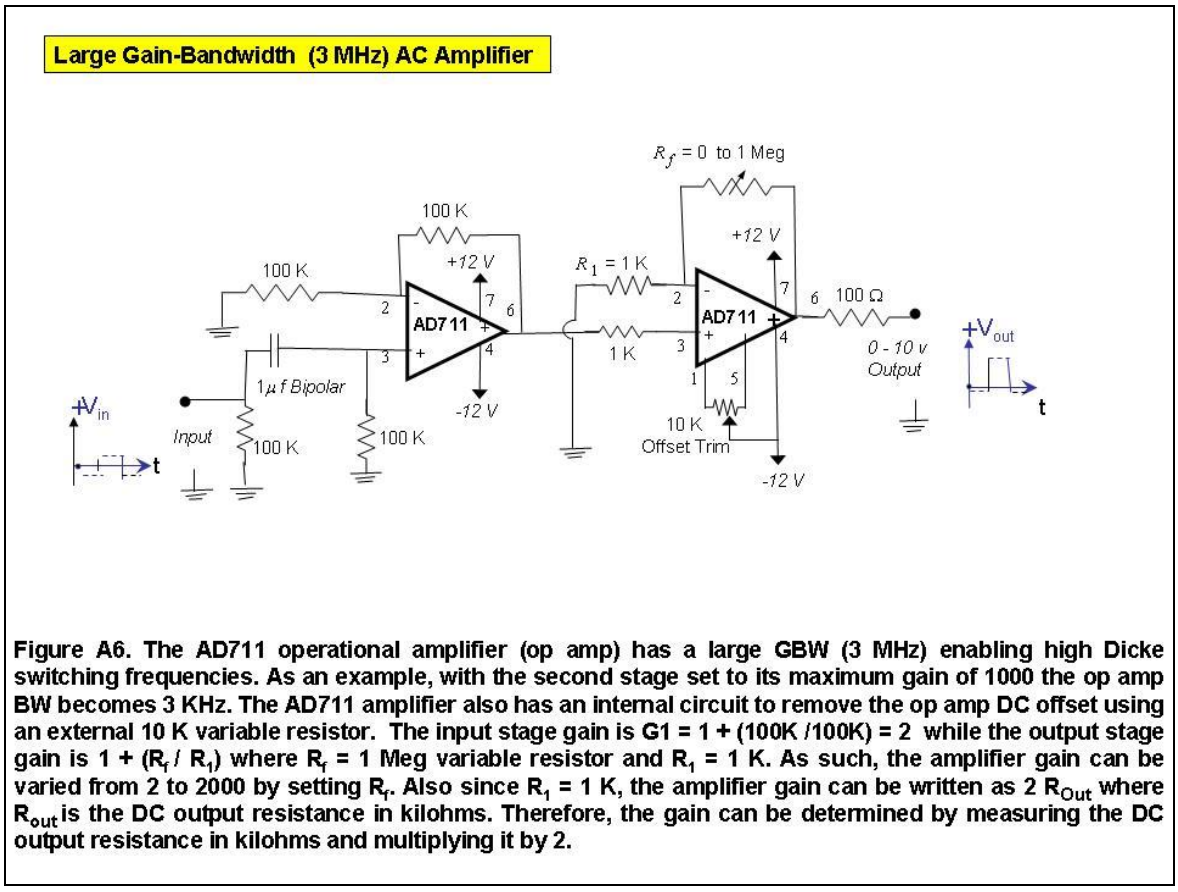

Figure A6. The AD711 operational amplifier (op amp) has a large GBW (3 MHz) enabling high Dicke switching frequencies. As an example, with the second stage set to its maximum gain of 1000 the op amp BW becomes 3 KHz. The AD711 amplifier also has an internal circuit to remove the op amp DC offset using an external 10 K variable resistor. The input stage gain is G1 = 1 + (100K /100K) = 2 while the output stage gain is 1 + (R_f / R_1) where R_f = 1 Meg variable resistor and R_1 = 1 K. As such, the amplifier gain can be varied from 2 to 2000 by setting R_f. Also since R_1 = 1 K, the amplifier gain can be written as 2 R_{Out} where R_{out} is the DC output resistance in kilohms. Therefore, the gain can be determined by measuring the DC output resistance in kilohms and multiplying it by 2.

A7. 4 GHz Radiometer Isolator

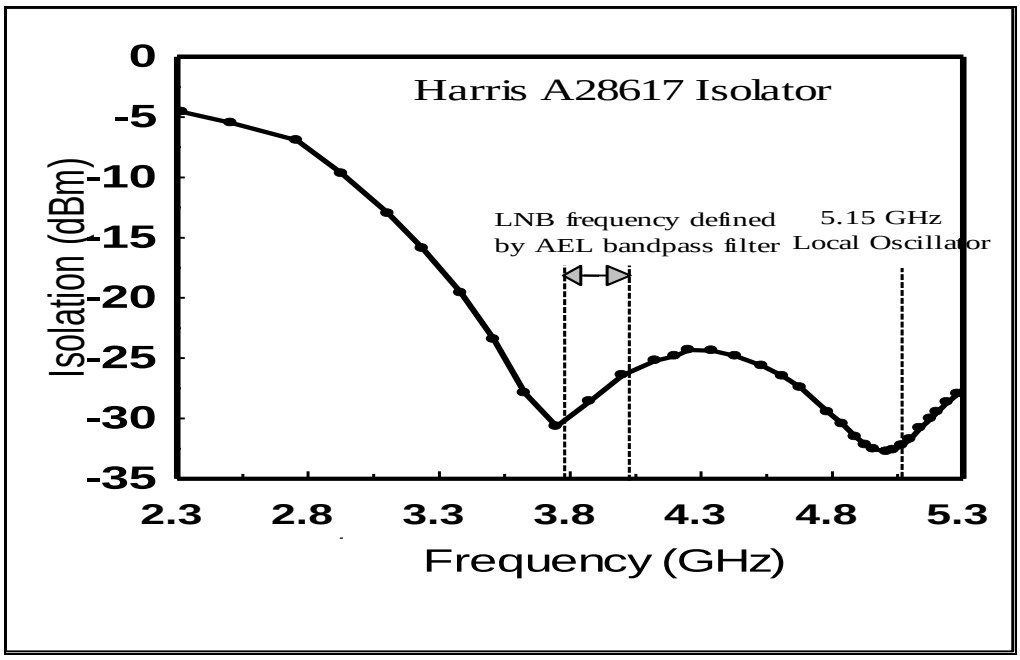

Figure A7. The isolator produces 30 dB of isolation at the C-Band LNB 5.15 GHz *LO*. It also provides similar isolation at the LNB frequencies of 3.76 to 4.01 GHz (defined by AEL filter).

A8. 4 GHz Radiometer *RFI* Filter

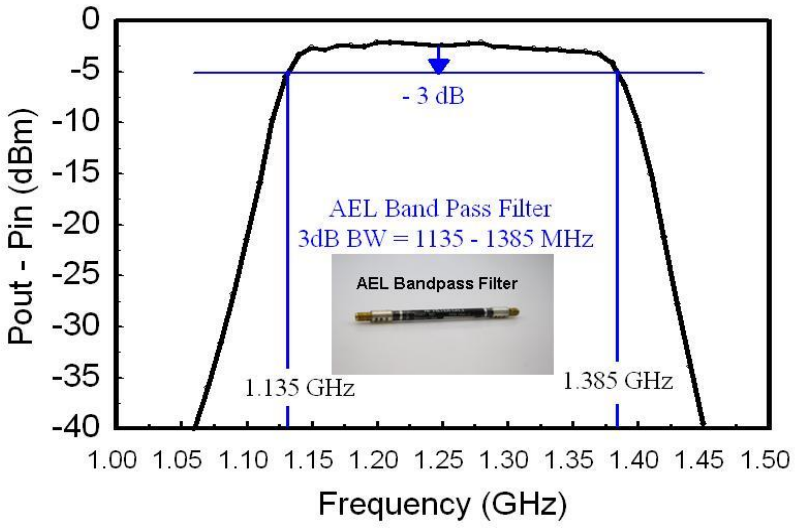

Figure A8. The bandpass filter is used in the 4 GHz radiometer to eliminate interference from WiFi, radar and aircraft altimeters. The filter has a 3 dB bandpass between 1.135 to 1.385 GHz (*i.e.* B = 250 MHz) with a center frequency of 1.260 GHz and a 2 dB insertion loss in the passband. The filter bandpass corresponds to LNB input frequencies from 3.76 to 4.01 GHz.

A9. Insertion Loss Measurements

Insertion loss measurements of the glass door are made using the 4 and 12 GHz radiometers. The instruments view the same outside scene, T_0, with and without the glass patio door opened. The calibrated brightness temperatures are then used to determine the reflectance by assuming that the glass attenuates the scene radiation due to reflection, without any absorption. Figure A9 derives the general equation describing the measurements as well as the result when the absorption is zero. In the zero absorption case the brightness temperature reduces to $T_b = (1 - R_g)\, T_0 + R_g T_g$ so the reflection coefficient is

$$R_g = \frac{T_b - T_0}{T - T_0} \ .$$

Using the above equation, Figure A9 shows the calculated reflection coefficients to be 0.20 at 4 GHz and 0.64 at 12 GHz. Section 7.1 contains a further discussion of these results.

As a point of interest, it is noted that the open door measurement, T_0, is much larger than the 2.7 *K* cosmic background due to the terrestrial objects seen by the antenna in addition to the sky radiation contribution. The measurements are also different at the two frequencies. It is a result of the nearly horizontal viewing angle required to make the insertion loss measurements of the glass door. This is different then when performing outdoor calibration measurements, where the radiometers are placed on the upper patio deck with the antenna directed upward to avoid viewing any of the surrounding earth radiation. However, it should be understood that this same scene radiation, T_0, is observed when opening and closing the door so that the stray radiation does not affect the transmission coefficient determination.

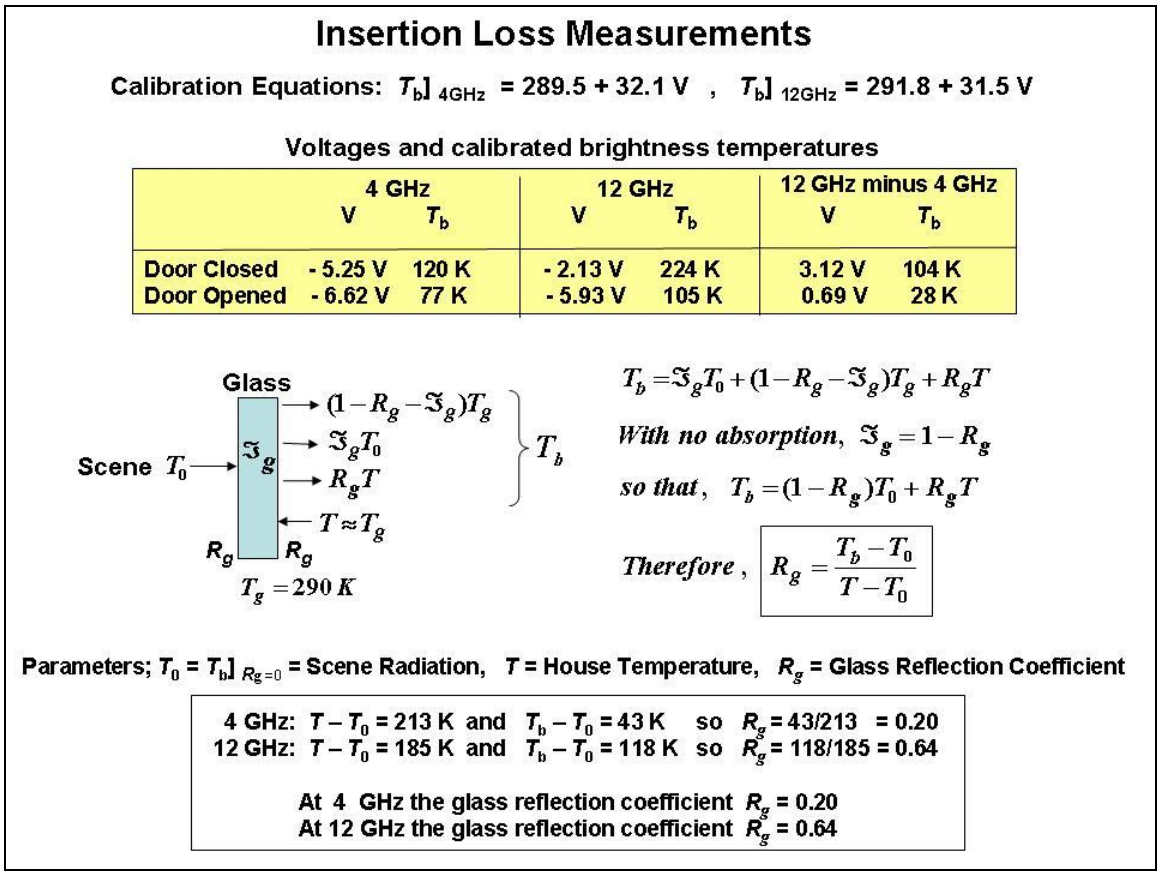

Figure A9. Insertion loss of a glass door is obtained from radiometer measurements with the door opened and closed. Neglecting absorption, the glass reflection coefficient is calculated to be 0.20 at 4 GHz and 0.64 at 12 GHz.

A10. Severe Storm Radiometer Measurements

As with the rain event on June 12, 2014, discussed in Section 7.2, measurements were taken on February 24, 2016 for another storm using the smallest integration time of 0.1 seconds. These measurements were also obtained with the radiometer viewing the event through my basement glass patio door. For reference, the local radar and enhanced satellite images were observed on my laptop computer and pictures were taken. The radiometer data was also displayed on my computer in real time using software provided with the analog to digital converter mentioned in Chapter 4. A composite picture of the radiometer measurement together with the radar and satellite images is shown in Figure A10. Of particular significance is the large increase in the 12 GHz radiometer voltage during the most intense rain period. This is accompanied by a relatively large increase in the 4 GHz radiometer voltage as well. Note that the scale used to display the 4 GHz radiometer measurements is at its minimum dynamic range of 0.45 volts while the scale of the 12 GHz measurements is expanded to a 4.8 volt range to display the full extent of its observations.

Figure A10 shows the largest radiometer increase at 12 GHz is 4.8 volts, while the corresponding voltage increase at 4 GHz is 0.375 volts. This voltage ratio of 12.8 for the

two frequency measurements is nearly the same value found for the rain event discussed in Chapter 7. Other rain events showed the voltage ratio to vary between 10 and 15. Also, when the 12 GHz output increased by 4.8 volts, its output reached 0.3 volts. For even heavier rain events the 12 GHz measurement has been observed to saturate at nearly zero volts while the 4 GHz showed no sign of saturation. Also note the abrupt voltage increases in the 4 GHz measurements. The spikes are seen sporadically throughout the measurement period although they are most pronounced during the most intense rain period when I heard and observed lightning. However, the 12 GHz radiometer measurements show no change associated with lightning discharge.

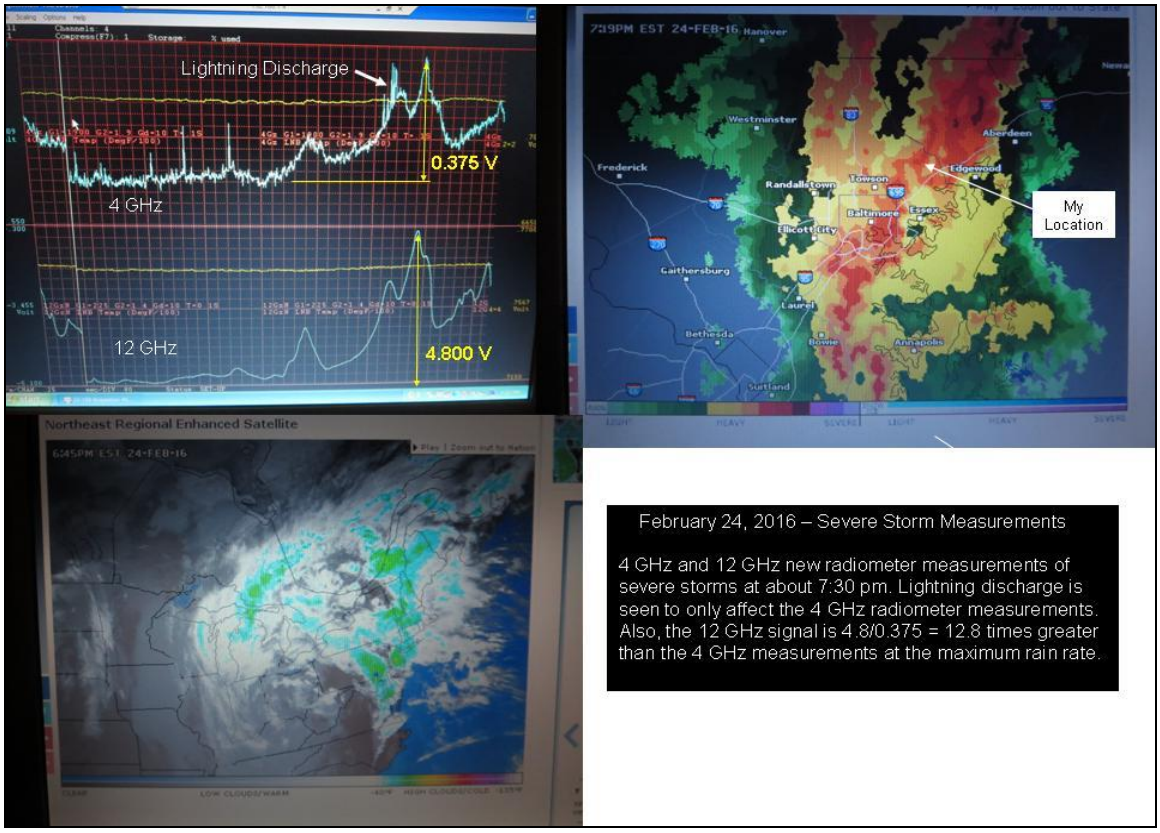

Figure A10. Radiometer measurements of a severe storm on Feb. 24, 2016. Shown are the 12 and 4 GHz measurements taken through a glass door as the storm passed through my area. Also shown is the online radar and satellite images at nearly the same time of my measurements, which was at 7:30 pm. For the maximum rain event, the ratio of the 12 to 4 GHz measurements is 12.8, which is nearly the same found in Figure 26 for a different rain system.

A11. Tipping Curve Analysis

This Appendix analyzes the tipping curve procedure used in Section 8.3 to measure the atmospheric transmittance for the 20 GHz radiometer by measuring the downwelling sky radiation, T_{SKY}, as a function of zenith angle. This novel procedure is also used to calibrate the radiometer.

The radiation transfer equation for the downwelling radiation is given by (5), *i.e.*,

$$T_{SKY}(\theta) = \tau^{Sec\theta}\, T_{CB} + \left(1 - \tau^{Sec\theta}\right) T_M \ , \qquad \text{(A11-1)}$$

where the radiometer antenna is assumed to have an unobstructed view of space. It also assumes a horizontally stratified atmosphere where T_M is the mean radiating temperature of about 285 *K* for the frequencies under consideration, and T_{CB} is the cosmic background 1radiation of 2.7 *K*. The equation contains the atmospheric transmittance, τ, along a vertical path between the radiometer and the upper atmosphere. For a horizontally stratified atmosphere, the $Sec\theta$ exponent of τ accounts for the longer path length due to viewing at off-zenith angles θ. All of these quantities (T_M, T_{CB}, τ, θ) are shown symbolically in Figure A11. The Figure also shows the geometry of a radiometer whose reflector redirects the downwelling radiation to its antenna. Figure 34 is a picture of the actual reflector used in the measurements.

We begin by considering the radiometer initially calibrated, for example, using the variable target temperature procedure described in Chapter 4. Using equation A11-1, the atmospheric transmittance due to oxygen and water vapor can then be obtained from the sky brightness temperature at any zenith angle, viz.,.

$$\tau = \left[\frac{T_{SKY}(\theta) - T_M}{T_{CB} - T_M}\right]^{Cos\theta} \qquad \text{(A11-2a)}$$

so that
$$\alpha = -\ln\tau = -Cos\theta \ln\left[\frac{T_{SKY}(\theta) - T_M}{T_{CB} - T_M}\right] \qquad \text{(A11-2b)}$$

Equation A11-2b can be used to obtain the opacity, α, and transmittance from a single sky measurement given the radiation temperatures T_M and T_{CB}. Furthermore, if we measure the brightness temperature at two viewing angles θ_1 and θ_2 we can eliminate the quantity T_{CB}-T_M so that the opacity becomes,

$$\alpha = \frac{1}{Sec\theta_2 - Sec\theta_1} \ln\left[\frac{T_M - T_{SKY}(\theta_1)}{T_M - T_{SKY}(\theta_2)}\right] \quad \text{where} \quad \tau = e^{-\alpha} \qquad \text{(A11-3)}$$

Although any two zenith angles can be used, for simplicity we use $\theta_1 = 0^0$ and $\theta_2 = 60^0$ so that the opacity becomes

$$\alpha = \ln\left[\frac{T_M - T_{SKY}(0^0)}{T_M - T_{SKY}(60^0)}\right]. \qquad \text{(A11-4)}$$

Lastly, if we measure the sky brightness temperature at a third angle θ_3 we obtain an expression for T_M, viz.,

$$\left[\frac{T_M - T_{SKY}(\theta_1)}{T_M - T_{SKY}(\theta_2)}\right]^{\eta} = \frac{T_M - T_{SKY}(\theta_1)}{T_M - T_{SKY}(\theta_3)} \quad \text{where} \quad \eta = \frac{Sec\theta_3 - Sec\theta_1}{Sec\theta_2 - Sec\theta_1} \qquad \text{(A11-5)}$$

While A11-5 is a nonlinear equation for T_M, it can be linearized for specific angles. For example, if $\eta \equiv 2$, $Sec\theta_2 - Sec\theta_1 = Sec\theta_3 - Sec\theta_2$ so that the solution for T_M reduces to,

$$T_M = \frac{T_{SKY}(\theta_1)T_{SKY}(\theta_3) - T_{SKY}(\theta_2)^2}{T_{SKY}(\theta_1) + T_{SKY}(\theta_3) - 2T_{SKY}(\theta_2)} \qquad \text{(A11-6)}$$

whose three angles can be $\theta_{1,2,3} = 0^0, 30.0^0, 40.2^0$ or $\theta_{1,2,3} = 0^0, 45.0^0, 56.9^0$, etc.,

Furthermore, upon substituting A11-6 into A11-3 we obtain the simplified equation,

$$\alpha = \frac{1}{Sec\theta_2 - Sec\theta_1} \ln\left[\frac{T_{SKY}(\theta_1) - T_{SKY}(\theta_2)}{T_{SKY}(\theta_2) - T_{SKY}(\theta_3)}\right] \qquad \text{(A11-7)}$$

whose opacity is independent of T_M and T_{CB}**.** It only depends on the sky measurements at the three viewing angles defined by $Sec\theta_2 - Sec\theta_1 = Sec\theta_3 - Sec\theta_2$, *i.e., equal spacing between* $Sec\theta$.

Having determined the opacity or transmittance, the cosmic background radiation temperature is obtained from upward viewing measurements using A11-3, *i.e.*,

$$T_{CB} = \tau^{-1}[T_{SKY}(0^0) - (1-\tau)T_M]. \qquad \text{(A11-8)}$$

Since T_{CB} = 2.7 *K*, then A11-8 can serve as a consistency check. Any increase in the calculated value of T_{CB} beyond 2.7 *K* is likely due to obstructions or unaccounted radiation affecting the sky viewing measurements at the different viewing angles. An example of such unaccounted radiation was described in Chapter 4 as due to the surrounding natural thermal emitted radiation scattered within the antennas FOV.

In summary, the above relationships utilize anywhere between one to three angular measurements to determine the atmospheric opacity. It is inherently assumed in deriving equations A11-3 to A11-7 that the opacity is independent of the viewing angle. This assumption is only possible for cloud free atmospheres where the opacity results from the nearly uniform absorption by oxygen and water vapor. However, once the radiometers are calibrated using cloud-free multi-angle measurements, the opacity of clouds and rain can be obtained from single angle measurement using equation A11-2.

Equations A11-2 through A11-7 provides analytic relationships to derive the opacity from angular measurements. An alternate graphical means of determining the opacity is obtained by differentiating A11-2b, so that

$$\alpha = \frac{1}{T_M - T_{SKY}(\theta)} \frac{d\,T_{SKY}(\theta)}{dSec\theta} = -\frac{d\ln\left[T_M - T_{SKY}(\theta)\right]}{dSec\theta} \qquad \text{(A11-9)}$$

Equation (A11-9) can be used to obtain the opacity by plotting ln [T_M -T_{SKY}] against $Sec\theta$ (referred to as *air mass*) and determine the best fit straight line having slope α. This graphical procedure has been the more traditional way of measuring opacity from radiometer measurements than the analytical solution given by A11-7. An argument for using A11-9 rather than A11-7 is explained below. Furthermore, in addition to measuring the opacity, the cosmic background T_{CB} is determined by extrapolating the brightness temperature plot to zero air mass, *i.e.*, $Sec\theta = 0$ in A11-1. This approach was originally developed and applied by Dicke in 1946 (*Phys. Rev.* 70, 340–348) to measure the opacity of oxygen and water vapor and is currently used as the primary technique for measuring opacity and calibrating ground-based radiometers. The procedure is applied in Section 8.3 to measure the clear atmospheric transmittance seen by the 20 GHz radiometer. It is also compared with the opacity obtained using A11-4. Furthermore, and most importantly, the procedure shall also be used to calibrate the radiometer.

While A11-9 uses the slope or first derivative of ln [T_M -T_{SKY}] to determine the opacity, A11-7 requires the curvature or second derivative. This is seen by differentiating A11-9 with respect to $Sec\theta$ so that

$$\alpha = -\frac{\dfrac{d^2\,T_{SKY}(\theta)}{d\,Sec^2\theta}}{\dfrac{dT_{SKY}(\theta)}{d\,Sec\theta}} \quad . \qquad \text{(A11-10)}$$

Using A11-7 or A11-10 to determine the opacity requires accurate measurements of the slope and curvature of the sky brightness temperature. Unfortunately, the curvature or second derivative is more susceptible to error than the first derivative, so in the case of noisy data it is better to use A11-9 to determine the opacity. However, upon using A11-9 the mean atmospheric temperature must be estimated using models or auxiliary data such as surface temperature and humidity. Incidentally, while the tipping curve procedure uses calibrated T_{SKY} measurements to determine opacity, the procedure can also be used for calibration, given T_{CB}. This latter approach is used in Section 8.3 to calibrate the 20 GHz radiometer. Its use is also referenced in the 2nd footnote on page 48.

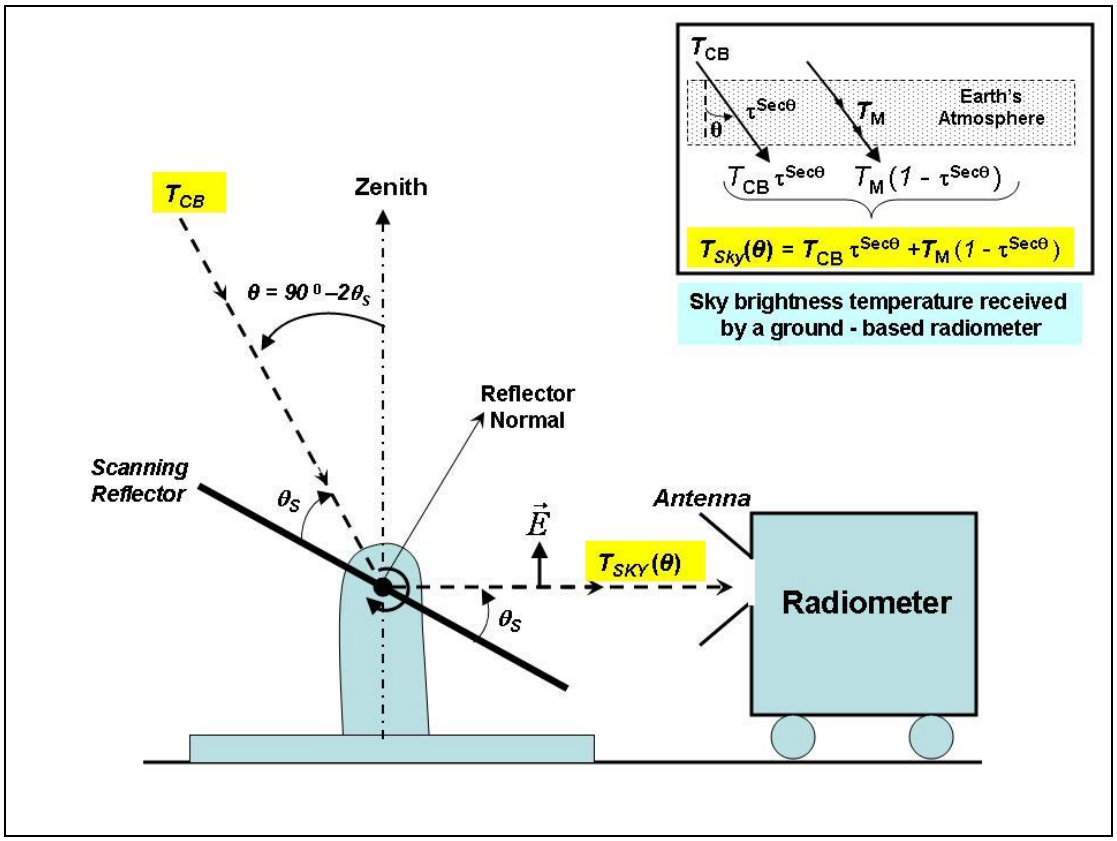

Figure A11. Schematic showing the tipping curve setup of a ground based radiometer having a linearly polarized antenna, where **E** is the electric field direction. The radiometer antenna views the sky through a reflecting surface that can be rotated to view the sky at different scan angles θ_S. Note that the zenith angle θ is related to the scan angle by $\theta = 90^0 - 2\theta_S$. Also shown in the insert figure are the two radiation components viewed by the radiometer, which when combined become $T_{SKY}(\theta) = \tau^{Sec\theta}\, T_{CB} + (1-\tau^{Sec\theta})\, T_M$. The actual tipping curve setup is shown in Figure 35. Section 8.3 demonstrates its use in calibrating the 20 GHz radiometer and measuring the atmospheric transmittance due to water vapor and oxygen. The Section also identifies some deficiencies of the setup.

A12. Parts list of Radiometer Components

Fan Controller shown in A2

Metallic Resistors	Variable Resistors	Thermistor	Diode	Op-Amp, FET
1 – 2 K Ω	1 –10 K Ω Trim	1 – 10K NTC	1N4001	IRF 510 Mosfet
1 – 4.7 K Ω	1– 50 K Ω Trim			LF 356
1 – 15 K Ω				

Synchronous Demodulator shown in A4

Metallic Resistors	Variable Resistors	Capacitors	Op-Amp, FET, Etc.,
1 - 100 Ω	1 - 2 K Ω	4 - 0.01 µf	1 - OP2111
1 - 150 Ω	1 - 5 K Ω Trim	1 - 0.05 µf	1 - AD711
2 - 220 Ω	2 - 100 K Ω Trim	1 - 0.1 µf	1 - LF356N
6 - 1 K Ω		1 - 1 µf (BiPol)	1 - NE555
1 - 5 K Ω		1 - 5 µf (BiPol)	1 - J177 Mosfet
2 - 10 K Ω		1 - 10 µf (BiPol)	
4 - 100 K Ω		2 - 100 µf (Pol)	
2 - 1 Meg Ω			
1 - 5 Meg Ω			

Detector shown in A5

Metallic Resistors	Variable Resistors	Capacitors	Schottky Detector
1 – 47 Ω	1 –50 K Ω Trim	1 – 47 pf	1 – HSMS 292 P
1 – 100 Ω		2 – 1.0 nf	
1 – 0.47 K Ω		2 – 0.1 µf	
4 – 474 K Ω			

AC Amplifier shown in A6

Metallic Resistors	Variable Resistors	Capacitors	Op-Amp
1 – 100 Ω	1 –10 K Ω Trim	1 – 1.0 µf (BiPol)	2 – AD711
1 – 1 K Ω	1 – 1 Meg Ω		
4 – 100 K Ω			